Nanoscale Observation and Analysis of Damage Formation and Annealing Processes in Ion Beam Interactions with Surfaces

Toshio Seki

January 2000

Abstract

For controlling ion beam processes at an atomic level, it is necessary to study the interaction between energetic ions and solid surfaces. This thesis aims to reveal the ion bombardment effects on surfaces and the process of annealing the damage caused by ion impacts.

The formation, structure and extinction of surface defects created at high temperature were observed with a Variable Temperature Scanning Tunneling Microscope (VT-STM). A Si(111) 7×7 surface was irradiated with Xe ions and single ion impact traces of about 20 Å diameter were clearly observed with atomic resolution. In the range from 1 to 5 keV, the average size of the trace did not depend on the impact energy. When the sample was annealed at 400°C, the vacancies created in the subsurface by the impact started to diffuse toward the surface and appear on the surface, but the interstitial atoms generated together with the vacancies remained in the bulk. At 600°C, vacancy clusters were formed, whose size corresponded to the number of vacancies created near the surfaces. At 650°C, the interstitial atoms diffused and recombined with surface vacancies and the size of the vacancy cluster decreased with annealing time.

When a Si(111) surface was irradiated with Ar cluster ions at 8 keV, the traces of a cluster ion impact showed a crater shape, with a diameter of about 80 Å. This indicates that cluster impact processes are quite different from a summation of separate monomer impacts. When the surface was annealed at 600°C after irradiation, the outer rim of the crater has disappeared and the hemispherical damage in the target was removed, but the hole at the center of crater remained.

On Highly Oriented Pyrolitic Graphite (HOPG) surfaces irradiated with carbon cluster of up to 70 atoms, large hills were observed. The impact site diameters were found to be proportional to cluster size for clusters of up to 10 atoms and increase discontinuously for cluster sizes above 10 atoms. This can be explained by considering that small affected areas overlap. This indicates that non-linear multiple collision effects occur only when a local area is instantaneously bombarded by more than 10 atoms.

In order to reveal the role of ion bombardment during film formation, ion bombardment effects at each stage of film formation were investigated. After annealing of a Si(111) sample at 400°C, with Ge atoms deposited to a few Å, the formation of many islands of Ge on that surface was observed. In order to physically change the shape of Ge islands by ion impacts, it is necessary to irradiate the surface so that the ratio of ions to deposited atoms is above 1/10. At this ion dose, the total number of defects is higher than that of deposited Ge atoms. When Ge islands on the Si(111) surface after Xe ion irradiation were annealed at 400°C, many small islands, vacancy clusters, and complicated steps were created. After annealing at 600°C, the islands either combined with the steps or became larger. The complex surface structure observed after Xe ion irradiation and thermal annealing can be caused by the appearance and surface migration of vacancies that were formed by Xe ion impacts. The Xe ion impacts can have a large effect on the film formation if samples are annealed.

When the Si(111) surface was irradiated with Ar cluster ion after Ge islands formation, the large craters were found. This result indicates that Ar cluster ion impacts can physically change the shape of Ge islands with low ion dose. The cluster ion impacts can also have a large effect on the film formation even if samples are not annealed.

Thus, the damage formation and annealing processes in ion beam interactions with surfaces can be analyzed with a VT-STM. The ion bombardment effects on surfaces and annealing process of surface defects are revealed at an atomic level.

Acknowledgments

I am extremely grateful to Professor Isao Yamada of Kyoto University for his guidance and encouragement throughout this study. His perceptive comments and suggestions have helped me to achieve this study.

I also would like to thank Professor Kenji Kimura of Kyoto University for his observations, comments and discussions of this study. I am also very grateful to Associate Professor Gikan Takaoka for many helpful comments.

I would like to express my deep gratitude to Research Associate Jiro Matsuo for his significant comments and helpful discussions. I am also grateful to Visiting Professors Rafael Manory, Zinetulla Insepov, and Kazunori Fukushima for many comments and advice in this study.

This research was made possible by the cooperation and assistance of many students at Kyoto University. I would like to thank Dr. Daisuke Takeuchi, Dr. Makoto Akizuki, and Dr. Noriaki Toyoda for discussion and encouragement. The computer simulation was done with great assistance from Mr. Takaaki Aoki. Many of the experiments related to this study were carried out by the assistance of Messrs. Masahiro Tanomura, Norihisa Hagiwara, Tadayuki Fukuhara, Takuya Kusaba, Masahiro Saito and Kazumichi Tsumura. I would like to thank them for their contributions. I am also thankful to all the members of Ion Beam Engineering Experimental Laboratory at Kyoto University during my doctoral course studies.

The Rutherford backscattering experiments were carried out with great help of the department of nuclear engineering at Kyoto University. I would like to thank Research Associate Kouji Yoshida for the operation of the accelerator.

Finally, I especially thank my parents for their support and encouragement.

Contents

Chapter 1

Introduction

1.1 Surface Observation with STM

In Ancient Greece around 500 B.C. Leuchippos and Democritos suggested that the universe consists of empty space and numberless minute particles. They named the minute particles that cannot be divided anymore 'atoms'. This is the atomic hypothesis. In the nineteenth century the basic concept of atoms was established by Dalton and this atomic concept is generally accepted in the modern physics of today. From that time, many scientists had desired to see the minute particles called 'atoms'. In 1953, E.W.Müller invented the Field Ion Microscope (FIM) [1] and he could see atoms on the surface of W tip for the first time. In 1982, Binnig and Rohrer invented the Scanning Tunneling Microscope (STM) [2]. The electronic state of conductive surfaces can be observed by using STM on an atomic level. The electronic state can be known from the tunneling current between a tip and a solid surface. If a tip scanned a surface, the image of the surface electronic state can be constructed. The positions of the surface atoms can be decided by the contrast in the image.

The surfaces of solids have reconstructed structures peculiar to each solid and have characteristics that are different from that in bulk. For example, the surface structure of Si(111) is of the 7×7 symmetry in which twelve Si atoms are reconstructed on a rhombus. The Si(111) 7×7 reconstructed surface was observed by Binnig and Rohrer with STM [3]. The model of Dimer Ad-atom Stacking fault (DAS model) as shown in Fig. 1.1 is agreed as the model of the 7×7 structure. DAS model was suggested by Takayanagi [4]. After success in the observation of such static surface structures, dynamics of surface atoms can be observed [5–10]. Dynamics of surface atoms at etching, film formation, and ion bombardment, has been studied actively.

1.2 Ion Beam Technique for Nanoscale Fabrication

Ion beams have been widely used for sputtering, implantation and epitaxial film formation. For sputtering, high selectivity and high rate sputtering are required. To produce next generation ultra-large-scale integrated circuit (ULSI), shallow implantation with low energy ion beams is necessary. Low damage and high activity ion beams are used for high quality film formation. For controlling these ion beam processes at an atomic level, it is necessary to study the interaction between energetic ions and solid surfaces. These processes are schematically summarized in Fig. 1.2.

When the target is bombarded with an energetic ion, surface atoms are sputtered, displaced, or moved to stable positions. The behavior of surface atoms at room temperature can be followed using the technique of STM. When a surface is irradiated with a low dose of low energy ions, individual defects are formed on the surface. If the surface can be observed at the annealing temperature, the annealing process of the defects can be understood. When a surface is irradiated with a high dose of low energy ions, the surface atoms become completely disordered. Here again, if the surface can be observed at the annealing temperature, the reconstruction process of the disordered surface can be understood. Thus, the annealing process of the damage caused by ion impact can be studied by using STM.

Ion assisted deposition is used for ultra high quality films [11–13]. However, the role of ion bombardment during film formation has still been unclear. Fig. 1.3 shows schematically the film formation process. The film formation process has several stages such as adsorption of in-

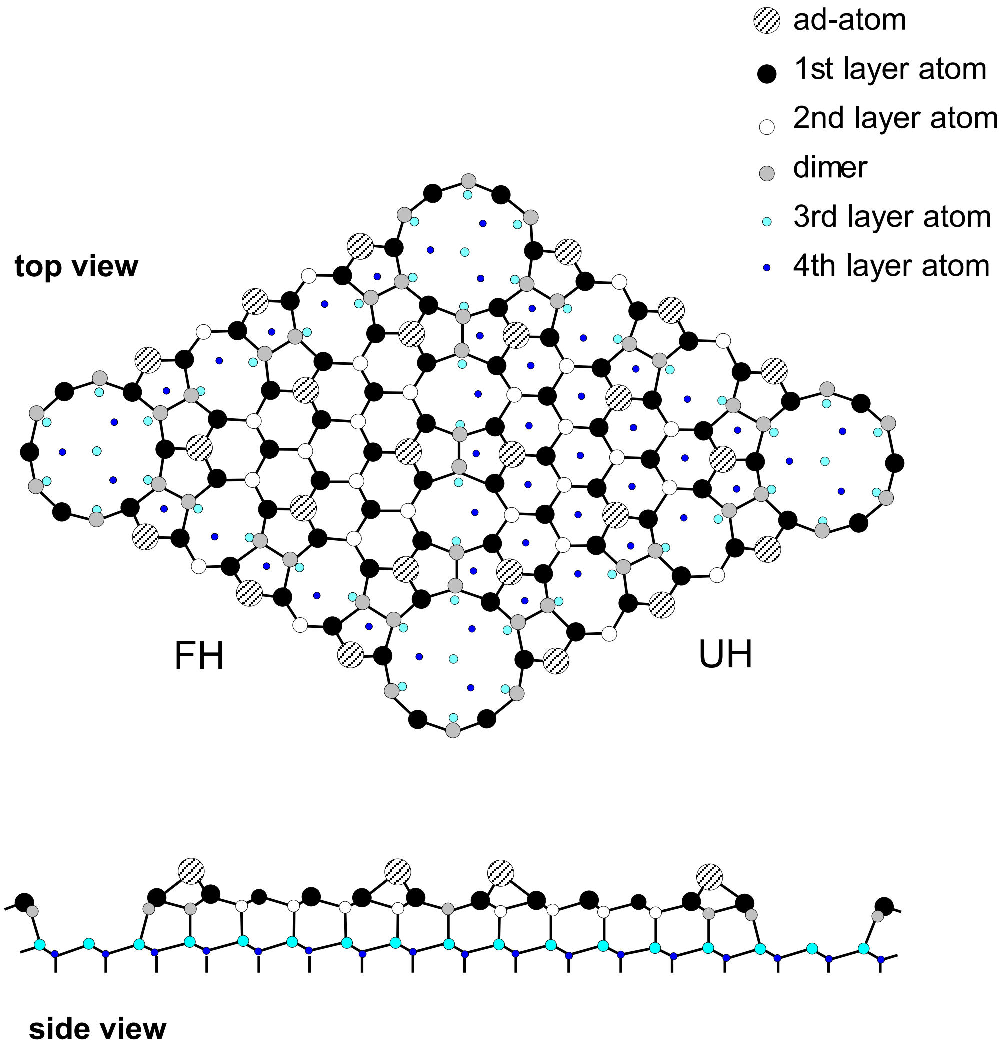

Figure 1.1: Dimer ad-atom stacking fault.

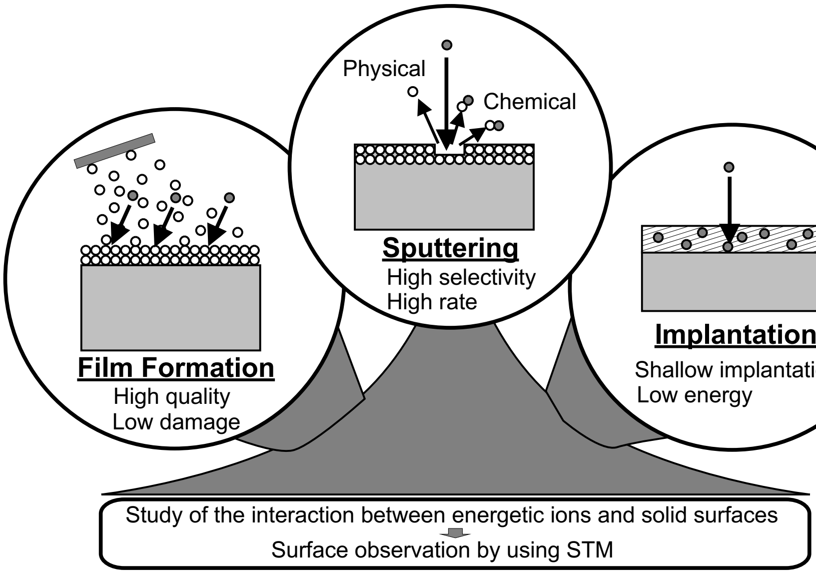

Figure 1.2: Ion beam technique.

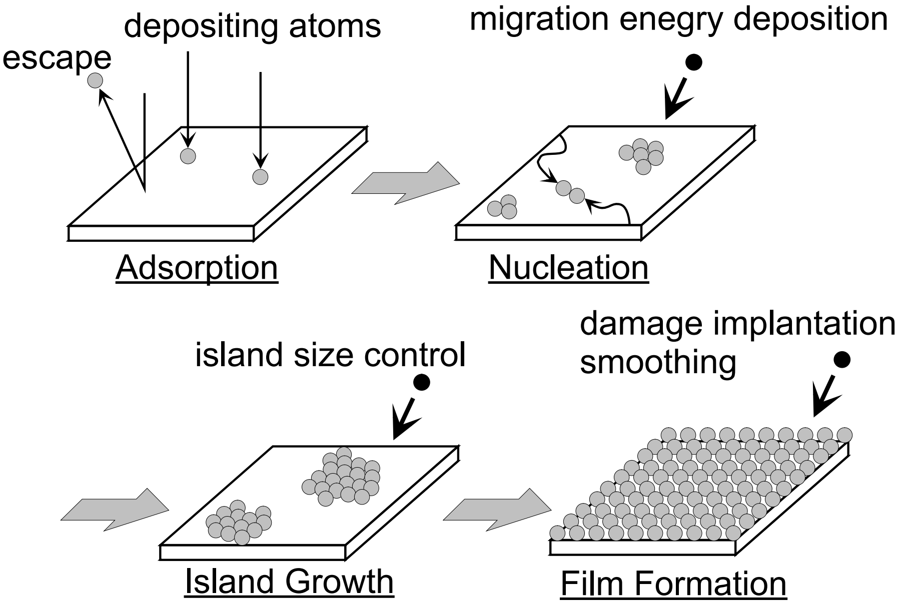

Figure 1.3: Film formation process.

coming depositing atoms on a surface, their surface diffusion, nucleation and island growth. On the stage of nucleation, the deposited atoms may be given migration energy from incident ions. Increase of migration energy causes formation of stable nuclei. At the stage of island growth, the size of the islands may probably be controlled with ion irradiation. When a large island is bombarded by an ion, the island may be divided into two or several islands. Small islands, inversely, may be combined into a large island by ion irradiation. After film formation, either surface smoothing or damage implantation may be performed with ion irradiation.

In order to reveal the role of ion bombardment during film formation, it is important to investigate ion bombardment effects at each stage of film formation. STM allows us to observe the surface on each stage before and after ion irradiation. The role of ion bombardment during film formation may be understood with the STM images.

1.3 Cluster Ion Beam Technique

A cluster is an aggregate of a few to several thousands atoms. At the Ion Beam Engineering Experimental Laboratory, we have been accelerating cluster ions to various targets. Because many atoms constituting a cluster ion bombard a local area, high-density energy deposition and multiple-collision are realized. Because of the interactions, cluster ion beam processes can produce unusual new surface modification effects, such as surface smoothing, high rate sputtering and very shallow implantation [14–17]. Various outstanding applications of the cluster ion beam have included so far: High quality tin doped indium oxide (ITO) films obtained by O_2 cluster ion assisted deposition at room temperature [18], smoothing of diamond films by Ar cluster beam [19, 20], formation of ultra shallow junction by using $B_{10}H_{14}$ ion implantation [21]. These applications are schematically shown in Fig. 1.4. Moreover, the irradiation of cluster ions enhance the chemical reactions on the substrate surface. SiO_2 films are formed on Si substrate surfaces at room temperature by irradiation with either CO_2 cluster ions [22] or O_2 cluster ions [23]. The

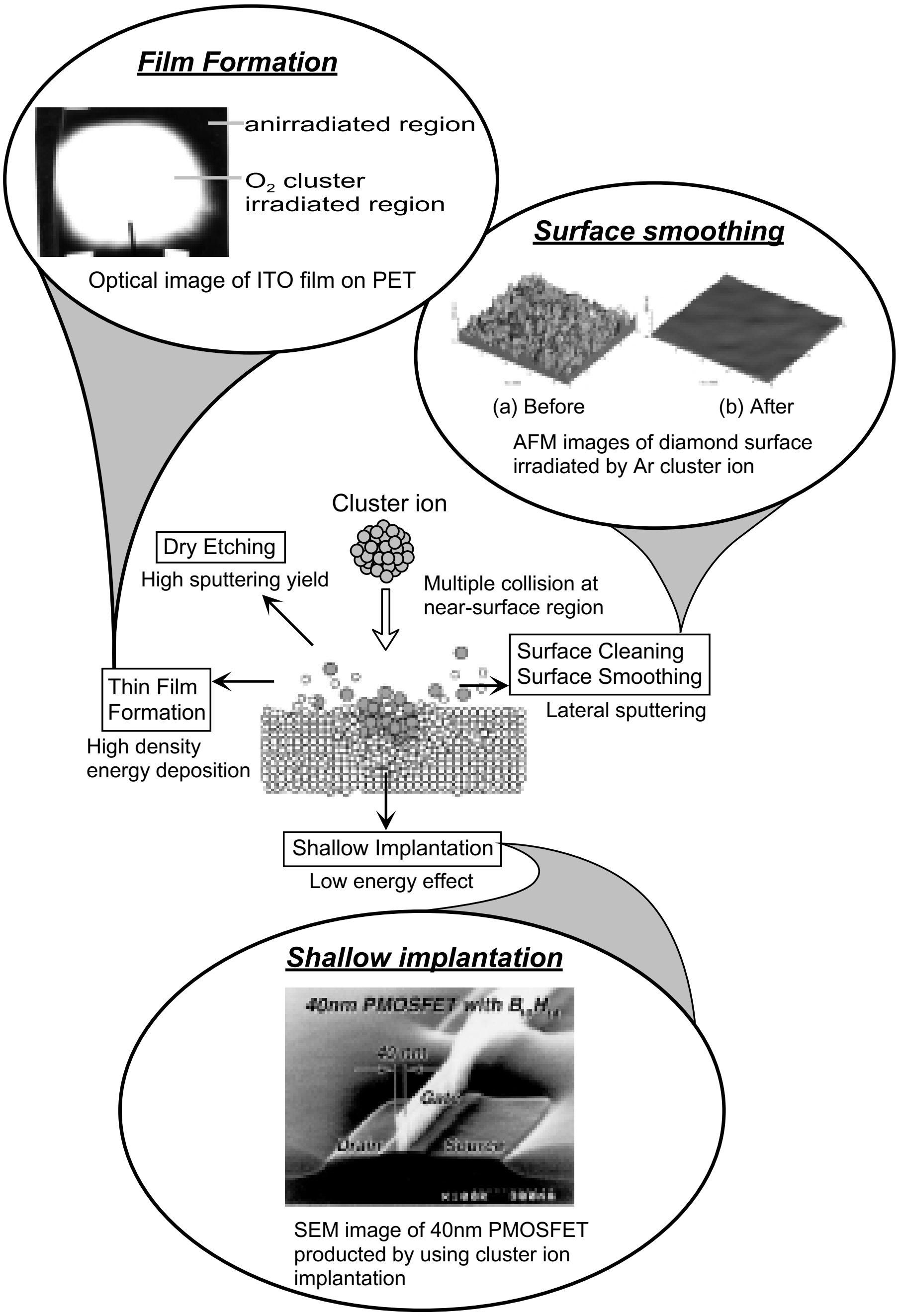

Figure 1.4: Applications of cluster ion beam.

reactive sputtering occurs on Si surfaces at room temperature by irradiation with SF_6 cluster ion [24].

In order to reveal the unusual surface modification effects of cluster ion beam, it is necessary to investigate the interactions between cluster ions and solid surfaces. There have been several reports about the interactions that were investigated with Rutherford Back Scattering (RBS) [25, 26]. However, RBS is not the analyzing method at the atomic level. In order to analyze the interactions at the atomic level, we have observed the traces of cluster ion impact by using STM. Large impact ridges and craters have been observed on solid surfaces [27–29] when Ar cluster ion beams with a size of more than 100 atoms were radiated on solid surfaces. Such a large crater, which has not been observed in monomer ion bombardments, is caused by high-density energy deposition to the surface and multiple-collision between cluster and surface atoms. But, the annealing process of the large craters has still been unclear. We have observed the traces created by Ar cluster ion impact and investigated the annealing process of the traces.

Recently, a new method for isolating and purifying fullerene (C_{60}, C_{70}) has been established and fullerene has been intensively studied [30–32]. Smaller sizes of Ar clusters, less than 100, can't be generated, but smaller sizes of carbon clusters, up to 70, can be generated as a consequence of cracking of the fullerene. These small clusters are ionized and subsequently accelerated to high energy. In order to observe cluster-surface interactions, it is important to investigate a single trace formed by a cluster impact on a solid surface. In particular, the size dependence of the trace diameter is very important, because the effect of cluster size, which is a unique parameter of the cluster ion beam, causes unique interactions that occur between cluster atoms and surface atoms. We have obtained clear images of a single trace formed by a carbon cluster ion impact and investigated the mechanism of the cluster-surface interaction.

1.4 Purpose of the Study

For controlling ion beam processes at an atomic level, it is necessary to study the interaction between energetic ions and solid surfaces. This thesis aims to reveal the ion bombardment effects on surfaces and annealing process of the damage caused by ion impacts.

In chapter 2, an ion beam system combined with a Variable Temperature Scanning Tunneling Microscope (VT-STM) in Ultra High Vacuum (UHV) is introduced and the properties of carbon cluster ion beam system are described.

Chapter 3 deals with the observation of a trace of single Xe ion impact by VT-STM. The annealing process of the damage caused by Xe ion impacts is investigated.

Chapter 4 presents observations of Si(111) surfaces irradiated with Ar cluster in UHV and the formation of crater type traces. The annealing process of the traces is investigated with VT-STM. Highly Oriented Pyrolitic Graphite (HOPG) surfaces are bombarded by carbon cluster ions. Clear images of a single trace formed by a carbon cluster ion impact were obtained and the mechanism of the cluster-surface interaction was investigated.

In chapter 5, investigation with STM of Ge islands formed on Si(111) surface is presented. The ion bombardment effect on the kinetic of nucleus growth was also studied.

Finally, chapter 6 presents a summary of the results of this study.

Chapter 2

Experimental Equipment

2.1 Introduction

In order to reveal the annealing process and understand the influence of ion impacts on film formation, we have developed an ion beam system combined with a Variable Temperature Scanning Tunneling Microscope (VT-STM) in Ultra High Vacuum (UHV). After irradiation with ions, the surfaces can be observed with VT-STM from room temperature to 800°C in situ.

Fig. 2.1 shows a schematic diagram of the ion beam system combined with VT-STM. The target chamber, exchange chamber and STM chamber are kept in UHV ($< 2\times10^{-9}$ Torr). A cluster ion beam and a monomer ion beam can be generated by the ion source. The ion beam enters the target chamber through a differential pumping chamber. After irradiation the sample can be moved into the STM chamber without being exposed to air. STM observations can be carried out while heating the sample ($<$ 800°C) by direct current.

In the STM chamber, the sample can be irradiated with Xe ions by using an ion gun. The surface can be observed by STM with Xe ion irradiation. In addition many kinds of metals can be deposited using the electron gun evaporator with ion irradiation in the target chamber, and the influence of ion impacts on film formation can be studied using

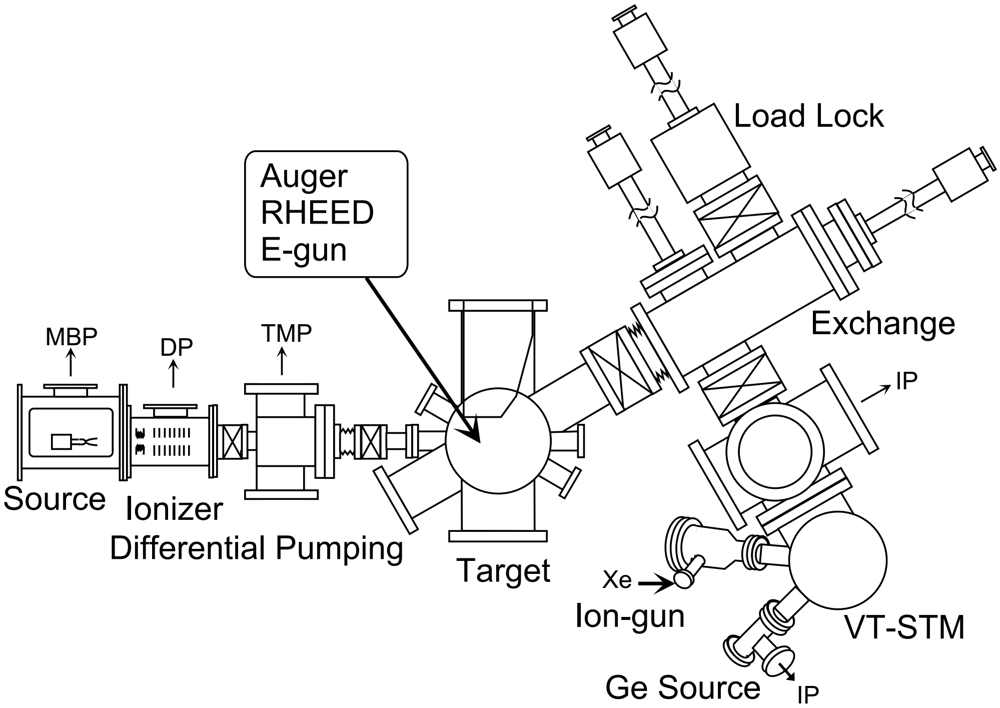

Figure 2.1: Ion beam system combined with VT-STM.

Reflection High Energy Electron Diffraction (RHEED), Auger Electron Spectroscopy (AES) or STM.

2.2 STM System

2.2.1 STM Combined with Ion Gun and Ge Source

Fig. 2.2 shows the picture and the schematic diagram of the STM chamber combined with the ion gun and the Ge source. The STM chamber is evacuated with an ion pump (IP) and a titanium sublimation pump (TSP). The pumping speed of the IP is 270 ℓ/s. The base pressure in the chamber is less than 1×10^{-10} Torr. The pressure is low enough to investigate surfaces of samples without any contamination.

The STM chamber is combined with an ion gun and a Ge source. Samples can be irradiated with Xe ions using the ion gun. The incident angle of Xe ions (θ_{Xe}) is 31° and the acceleration energy is from 0.5 keV to 5 keV. The chamber of Ge source is evacuated with IP which has a pumping speed of 8 ℓ/s. The base pressure in the chamber is less than 2 $\times10^{-8}$ Torr. Ge is evaporated from a Ge mass heated up by a W wire, which is wound up around the Ge mass. The incident angle of Ge (θ_{Ge}) is 29°.

2.2.2 High Temperature STM Observation

Fig. 2.3 shows a picture of the VT-STM. The VT-STM stage is suspended by springs in four support tubes and can swing freely in all directions. Because copper plates around the stage are alternated with magnets, eddy currents occur and vibrations can be suppressed. An STM scanner is centered in the stage and STM tips are set upward on the scanner. Samples are set over the tips with the bottom up.

Fig. 2.4 shows a schematic diagram of the sample holder of the VT-STM. In this study, samples are boron doped p-type Si bars whose width is 1 mm and resistivity is from 0.4 to 0.6 Ω·cm. The bar is connected with its positive at the sample's right side and its negative at the samples left side.

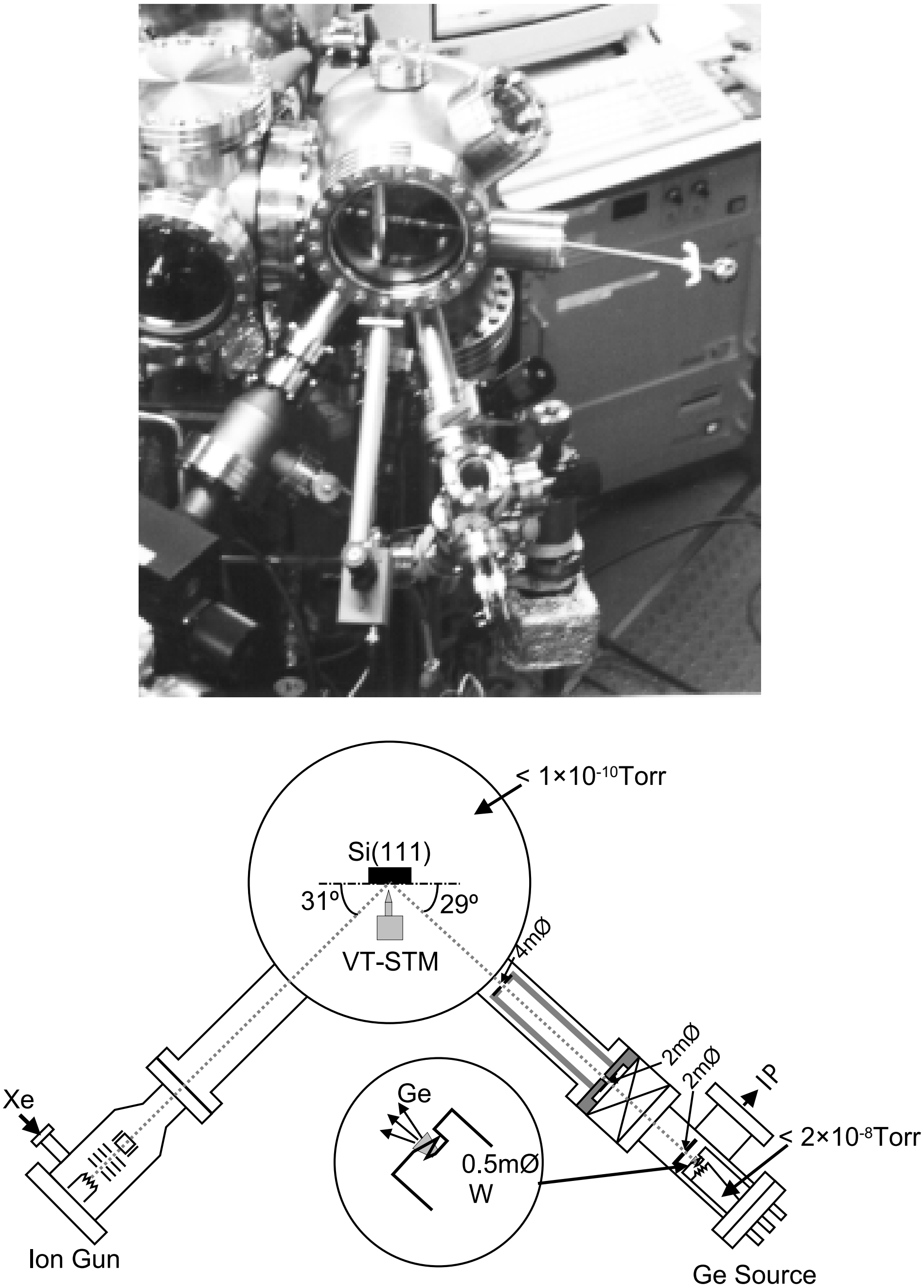

Figure 2.2: STM chamber combined with ion gun and Ge source.

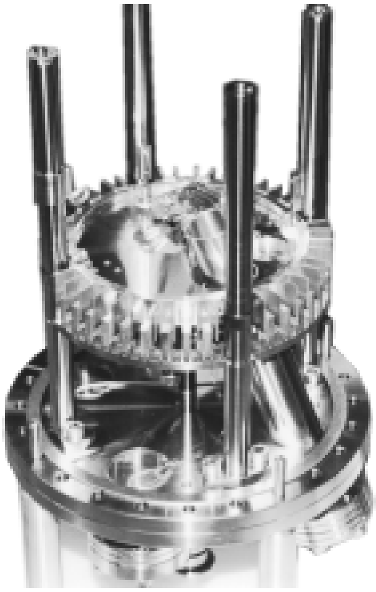

Figure 2.3: VT-STM system.

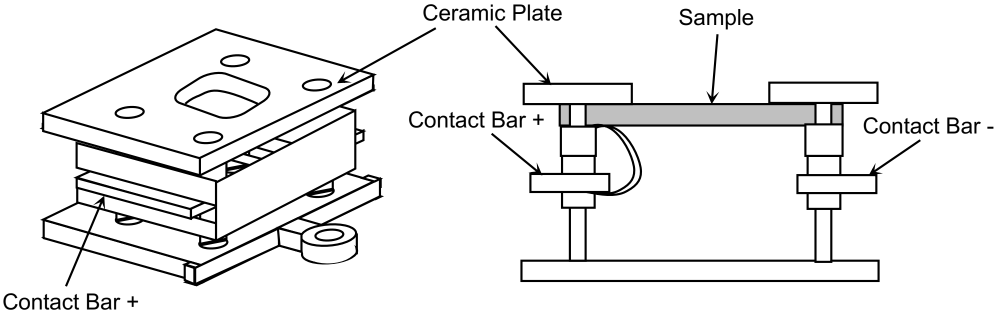

Figure 2.4: Schematic diagram of a sample holder of the VT-STM.

The sample can be heated ($< 800°\mathrm{C}$) with direct current passing between the ends of the contact bar, and STM observations can be carried out while heating. The bias voltage of the tips during heating is compensated as follows: When the slope of potential in the samples is constant, the potential at scan point is

$$V_{comp} = V_H \times \frac{l_x}{l_s}, \tag{2.1}$$

where V_H is the heating voltage, l_s is sample length and l_x is length between grand electrode and tip. Therefore, the bias voltage is

$$V_t = V_{gap} + V_{comp}, \tag{2.2}$$

where V_{gap} is the expected gap voltage. Thus, VT-STM allows us to obtain a series of images of the atoms moving on the surface at the annealing temperature. In addition, ion irradiation effects on film formation can be investigated using the ion gun and the Ge source.

2.3 Gas Cluster Ion Beam System

The ion source can generate gas cluster ion beams. A cluster is an aggregate of a few to several thousands atoms. In this section, the principle of cluster generation, the 10 kV gas cluster ion beam system, and the characteristics of the gas cluster beam are described.

2.3.1 Gas Cluster Generation

Adiabatic expansion of a high-pressure gas through a nozzle is utilized for the formation of gas cluster beams. When the high-pressure gas is ejected into the vacuum through a nozzle, the momenta of the atoms align with the beam direction. The temperature equivalent to the relative velocity among them goes down and the gas becomes supersaturated. A phase transition occurs in the supersaturated gas due to the fluctuation effect [33, 34]. When the nucleus radius becomes larger than the critical radius, the cluster is stable and grows. In this thesis, the laval nozzle, shown in

Fig. 2.5, was used. This is a glass nozzle. The diameter of the throat of the nozzle is 0.1 mmϕ and the caliber is 3 mmϕ.

When a supersonic flow ejects from the nozzle, shockwaves are generated [35]. The supersonic flow changes to a subsonic one at the boundary where the temperature, velocity and pressure are discontinuous. One of the shockwaves appears in front of the supersonic flow. These shockwaves are well understood for free jets issuing from axisymmetric sonic nozzles. Their axial position, X_m, is

$$\frac{X_m}{d_0} = 0.67 \times \left(\frac{P_0}{P_{src}}\right)^{1/2}, \tag{2.3}$$

where d_0 is the nozzle diameter, P_0 is the pressure of the source gas, and P_{src} is the pressure in the source chamber [36]. When P_0 is 2 atm, P_{src} is 0.01 Torr, and d_0 is 0.1 mmϕ, a shockwave forms at the distance 26.1 mm from the nozzle edge.

These shockwaves disturb the generation of neutral cluster beams. To avoid formation of such shockwaves, the skimmer was developed. The skimmer extracts the core of the supersonic flow and the cluster beam is introduced into high vacuum. Fig. 2.6 shows the picture and the schematic diagram of a typical skimmer. The outer and inner angle of the skimmer with the flow centerline are 55° and 40°, respectively, and the skimmer lips are made as sharp as possible [37]. The diameter of the skimmer's orifice is 0.3 mmϕ.

The cluster beams is generated by highly pure source gas flow through a nozzle. In order to avoid these shockwaves disturbance, the source pressure is suppressed though the source gas flow. A mechanical-booster pump is used to keep a good vacuum level in the source chamber, because of its large pumping speed, around 10^{-3} Torr. The pumping speed of the pump is 222 ℓ/s. When the source Ar gas pressure was 5 atm, the vacuum in the source chamber was kept at 0.01 Torr. The skimmer is placed at the center of the beam axis and 23 mm behind the nozzle exit. Because the distance (23 mm) is shorter than 26.1 mm, which was calculated using equation 2.3, the neutral cluster beams can avoid the shockwaves and go into ionizer.

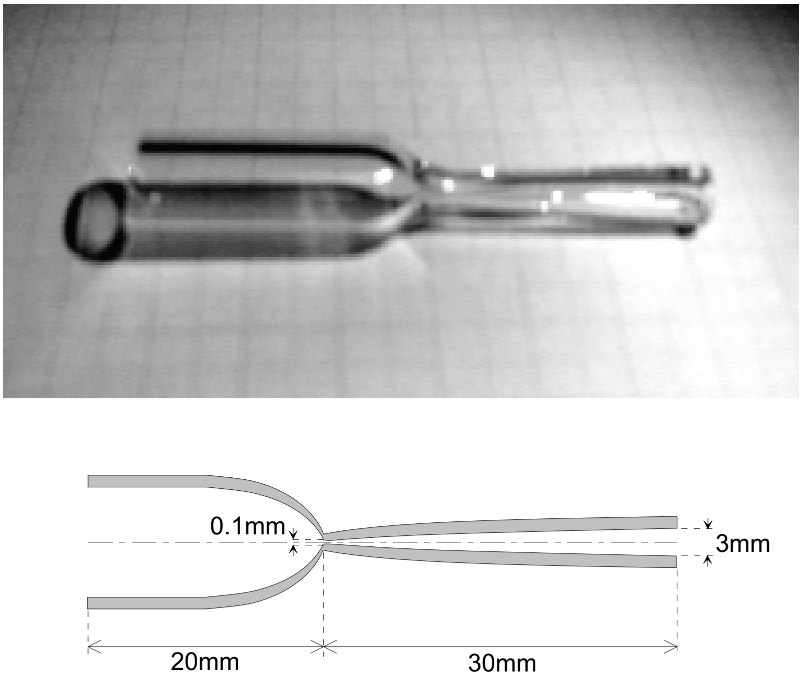

Figure 2.5: Picture and schematic diagram of a nozzle.

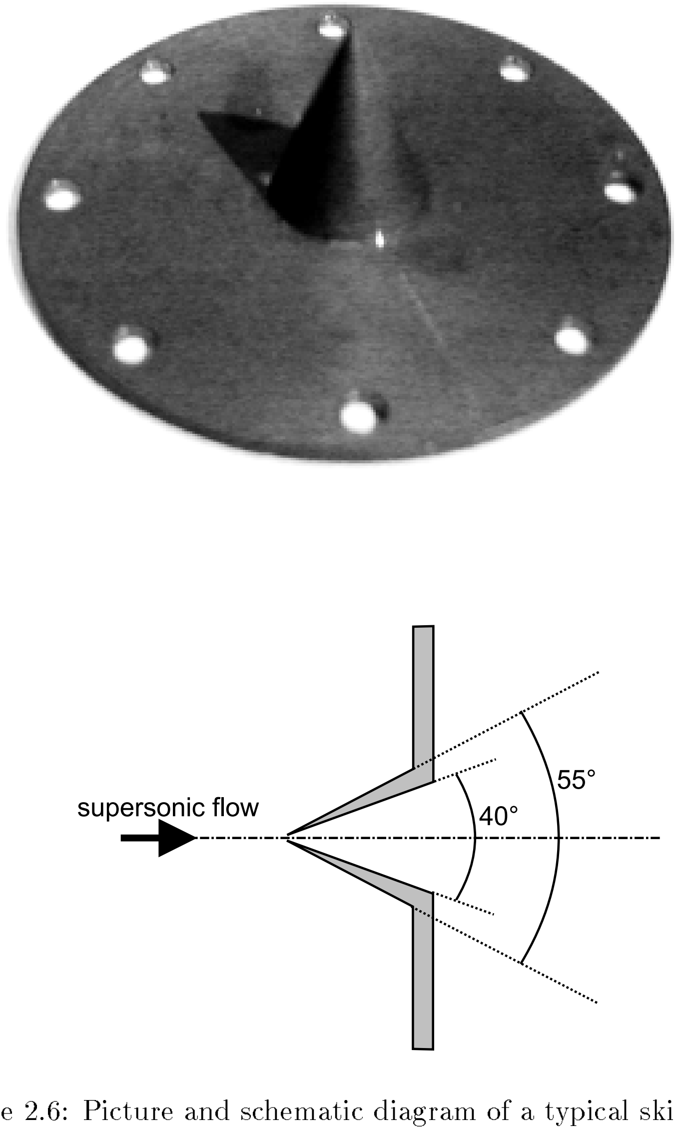

Figure 2.6: Picture and schematic diagram of a typical skimmer.

2.3.2 Ionizer Chamber

Neutral gas clusters are ionized by the electron bombardment method in the ionizer chamber. The ionizer chamber is evacuated by a diffusion pump (DP) and is kept at 1×10^{-6} Torr when not supplied with gas. When Ar gas was supplied at 5 atm, the ionizer chamber pressure became 2 $\times10^{-5}$ Torr.

Fig. 2.7 shows the picture and the schematic diagram of an ionizer. The ionizer consists of filaments, anode, extraction electrode, and einzel lens. This ionizer has three filaments, which occupy positions 120° apart and are parallel to the anode electrode. The anode is a tube whose diameter is 30 mmϕ. The exit side of the anode is covered with a grid with high transmittance (90%), which avoids the distortion of the electrostatic potential inside the anode. Electrons ejected from hot filaments are accelerated toward the neutral cluster beam and ionize clusters.

The ionized clusters can be accelerated by an extraction electrode. In this thesis, however, the extraction voltage (V_{ext}) was set 0V, because of reduction of monomer ions. As the velocity of all neutral Ar atoms is the same, the initial kinetic energy of a monomer is much lower than that of a cluster. The fraction of monomer ions can be reduced by means of space charge effects between the exit of anode and the extraction electrode. As the result, only cluster ions with large initial kinetic energy are extracted and focused by an einzel lens.

2.3.3 Target Chamber

In order to keep a good vacuum level in the target chamber during irradiation, the cluster beams go into the target chamber through a differential pumping chamber. The differential pumping chamber is evacuated with a turbo molecular pump (TMP). The pumping speed of the pump is 70 ℓ/s. The beam entrance and exit of this chamber is covered with apertures whose diameters are 10 mmϕ. These apertures suppress the flow of the background gas into the target chamber during Ar irradiation.

The target chamber is evacuated with TMP whose pumping speed is

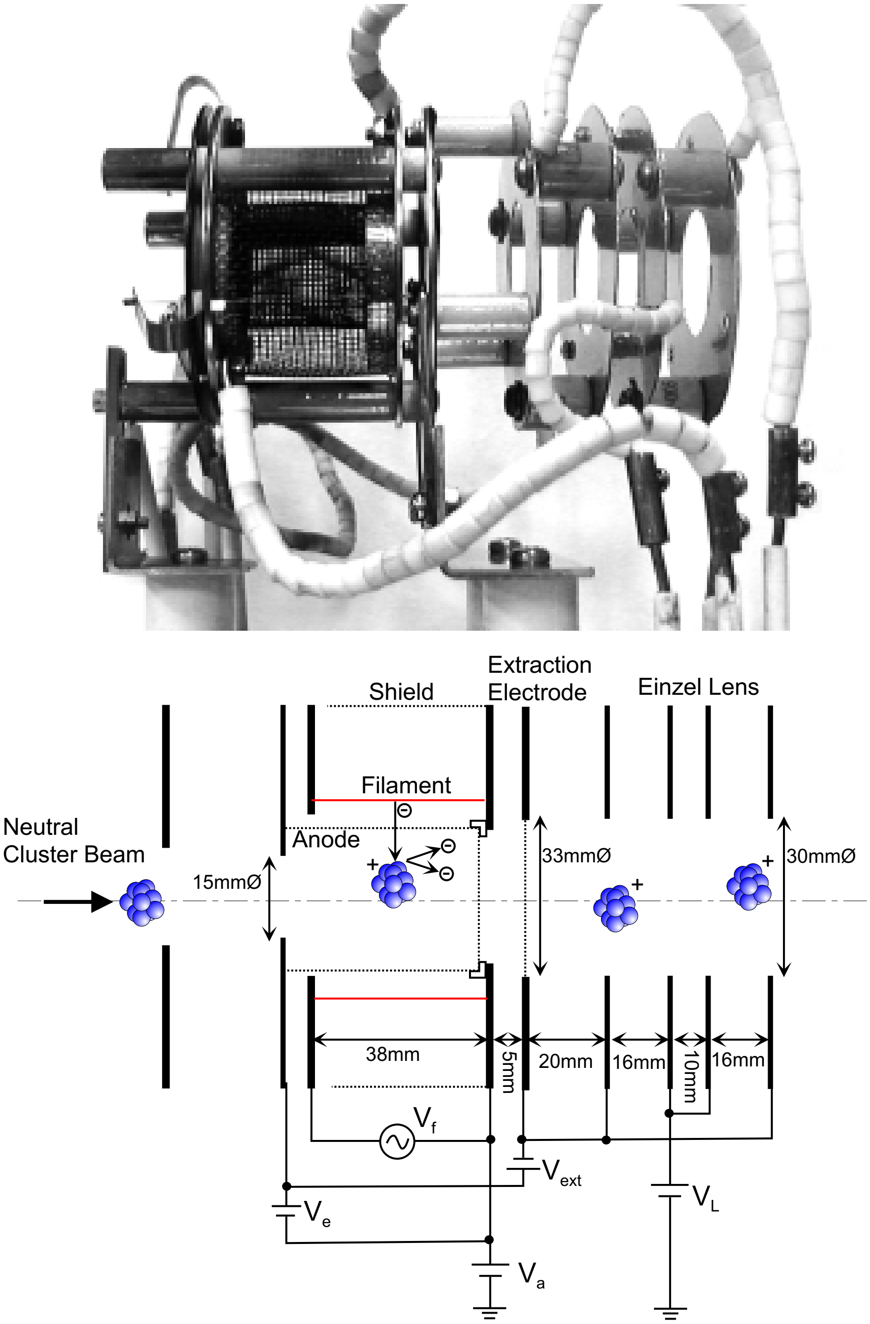

Figure 2.7: Picture and schematic diagram of an ionizer.

550 ℓ/s. The initial pressure in this chamber is less than 2×10^{-9} Torr. When Ar gas was supplied at 5 atm, the target chamber pressure became 4×10^{-7} Torr. A sample holder can hold 25×25 mm^2 samples and be introduced into the target chamber from a load lock chamber through an exchange chamber. The samples can be annealed to 1000°C with a Pyrolytic Boron Nitride (PBN) heater of the sample manipulator in the target chamber.

2.3.4 Cluster Size Distribution

The cluster size distribution is the most important property of cluster beams, because the cluster size, which is a unique parameter of the cluster ion beam, causes unique interactions that occur between cluster atoms and surface atoms. Fig. 2.8 shows mass distributions of Ar cluster for different supplied gas pressures. The mass distributions were measured with a Time-of-Flight (TOF) attached to the ion source. When the supplied gas pressure was more than 2 atm, clusters were measured. This shows that the threshold of supplied gas pressure for Ar cluster generation was about 2 atm. The mean size of clusters increased with the supplied gas pressure and became about 1000 at 5 atm.

2.4 Carbon Cluster Ion Beam System

2.4.1 Carbon Cluster Generation

Fig. 2.9 shows a schematic diagram of the carbon cluster ion beam system. Neutral carbon clusters were generated by heating fullerene powder to 400-600°C by an oven in the hot-hollow cathode ion source. The source chamber is evacuated with TMP and the initial pressure in this chamber is less than 8×10^{-7} Torr. After ionization of the neutral clusters by electron bombardment, the cluster ion beam is focused by an eintzel lens. Some of the fullerene molecules were dissociated by electron bombardment. Cluster ions were mass-separated by a 90° magnet, and accelerated up to 400 kV.

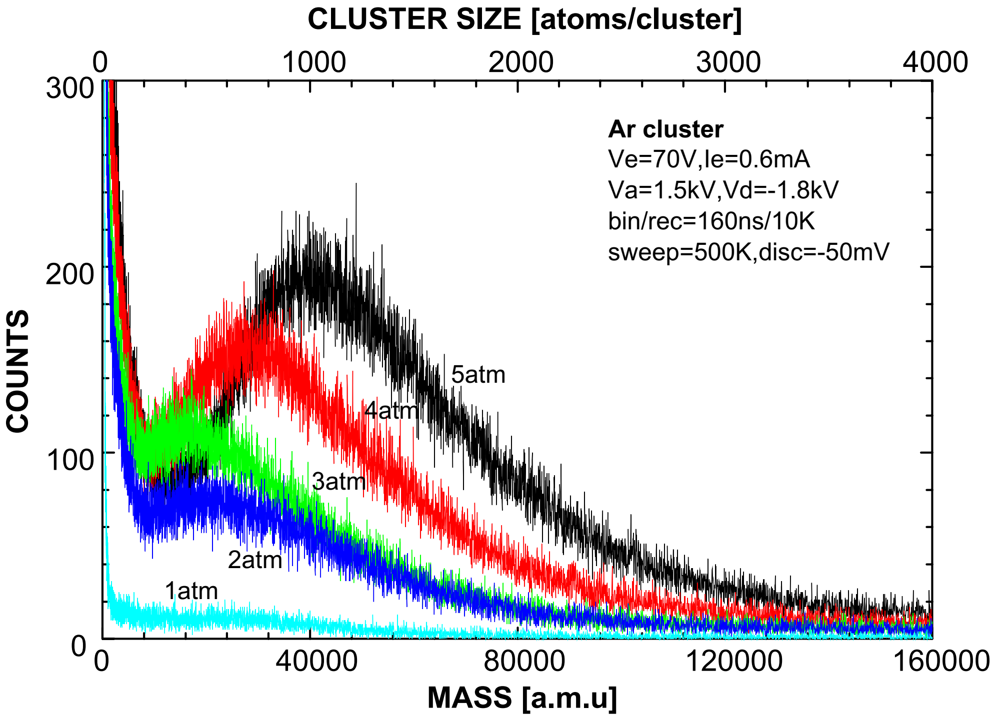

Figure 2.8: Mass distributions of Ar cluster for different supplied gas pressures.

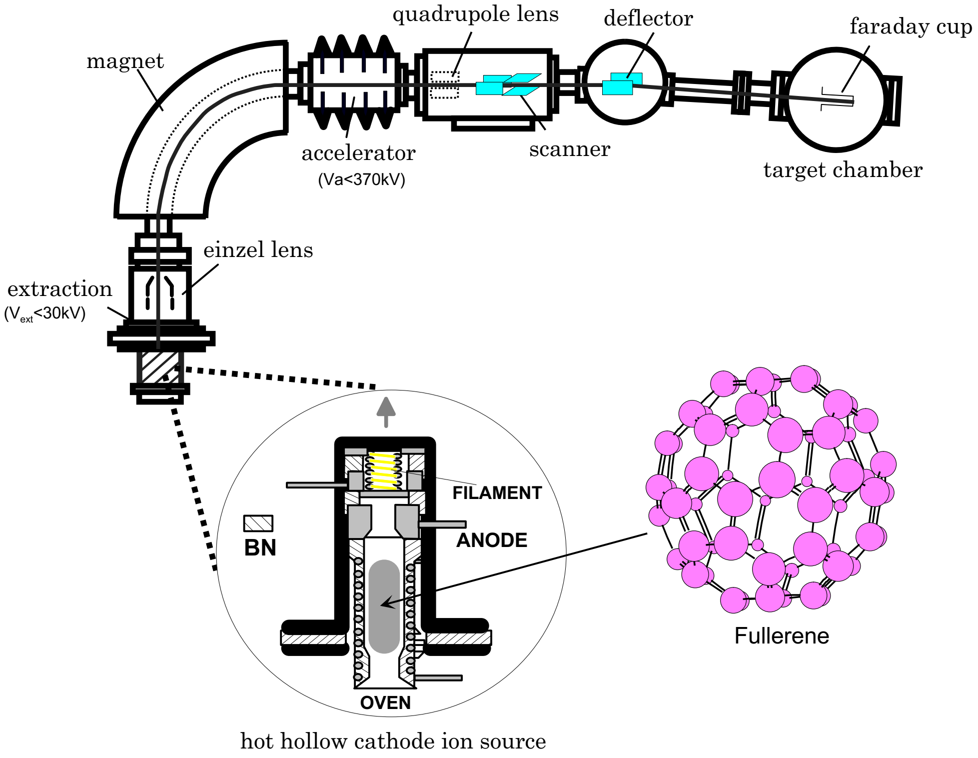

Figure 2.9: Schematic diagram of carbon cluster ion beam system.

2.4.2 Cluster Size Distribution

The target chamber is evacuated with diffusion pump and the initial pressure in this chamber is less than 5×10^{-7} Torr. When a surface is bombarded by a cluster ion, many secondary electrons and ions are emitted because of the multiple collisions between the incident atoms and the substrate atoms [25]. In order to count a high energy cluster ion dose accurately, both the secondary electrons and ions should be counted. Therefore, a sample was set in a Faraday cup as shown in Fig. 2.10. Because neither secondary electrons nor ions can escape from the Faraday cup, the cluster ion dose is measured with an ammeter between the Faraday cup and ground. When the edge of electrode I is bombarded by a cluster ion, several secondary electrons and ions may be emitted toward the sample. However, they cannot reach the Faraday cup because the potential of electrode II is -300V.

Fig. 2.11 shows the mass spectrum of carbon cluster beam generated from mixed C_{60}, C_{70} powder. Various sizes of clusters - up to 70 - and some doubly charged ions were generated as a consequence of cracking fullerene. C_n^{2+} beams are generated and doubly charged ions are able to be accelerated to 800 keV. Subsequently, the carbon cluster beams were scanned in order to produce a uniform irradiation and deflected at 3° in order to remove neutral beams.

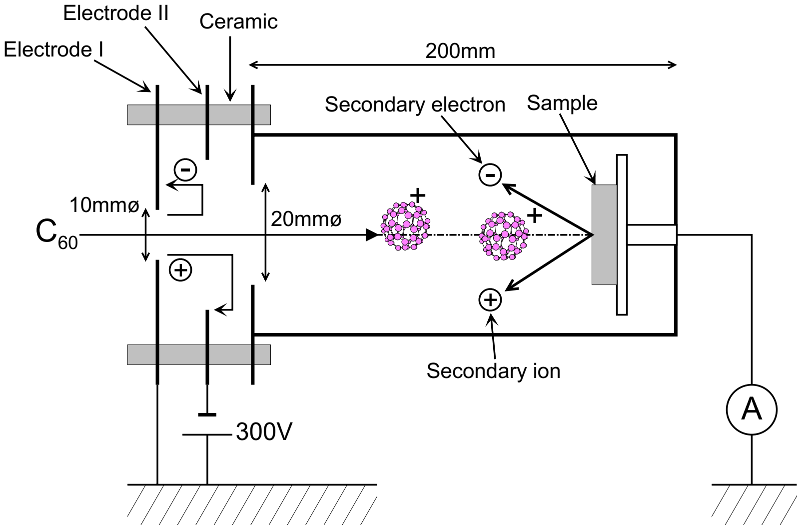

Figure 2.10: Schematic diagram of the Faraday cup in the target chamber.

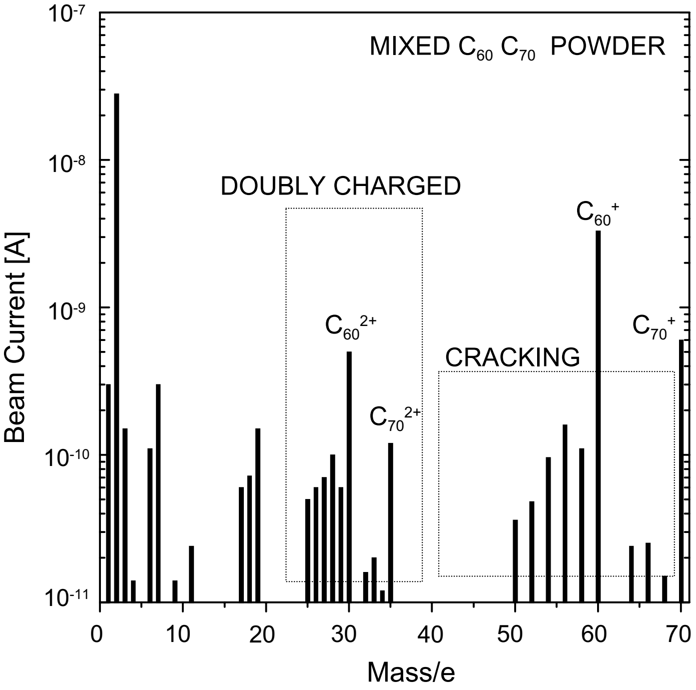

Figure 2.11: Mass spectrum of carbon cluster beam generated from C_{70}, C_{60} mixpowder.

Chapter 3

Surface Effects by Xe Ion Impact

3.1 Introduction

Surface defects have been investigated with the technique of STM at room temperature, but the annealing process of defects caused by ion impacts has remained unclear. STM observation at high temperature may give us better understanding of the annealing process on an atomic scale. An apparatus, which combines a VT-STM and an ion source in UHV has been constructed. The atomic structure of surface defects created by ion impact and the annealing process were studied with this apparatus in situ at various temperatures, from room temperature to 800°C. Xe ions were used in this study because low energy Xe ion has a large collision cross-section with surface atoms. In this chapter, we discuss the thermal annealing process of defects caused by low energy Xe ion impacts.

3.2 Si(111) Clean Surface

Fig. 3.1(a) shows the STM image of a clean Si(111) surface prepared as follows: Samples of Si(111) were cleaned chemically with an HF solvent after initially cleaning with an aceton solvent, and then an oxide layer was formed on the surfaces with a sulfuric acid solvent. After transference to the UHV chamber, the samples were flashed to 1250°C for a minute to eliminate the oxide layer in this chamber. We used a chemically polished W tip for the probe. These observations were carried out at the following conditions: tunneling current was 0.5 nA, bias voltage was +2.0 V and chamber pressure was lower than 5×10^{-10} Torr. The 7×7 reconstructed surface was observed clearly at room temperature. This atomic resolution image shows that the Si(111) surface was atomically flat, so that we can discuss a single trace of an ion impact at an atomic level.

Fig. 3.1(b) shows the STM image of a Si(111) surface exposed to an atmosphere of Xe for 5 minutes in the STM chamber. The Xe pressure was 1×10^{-7} Torr, which is higher than that during Xe ion irradiation. After exposure, the 7×7 reconstructed surface could be observed clearly at room temperature. A few vacancies were generated by the exposure to Xe. However, because the vacancy islands were smaller than those caused by Xe ion impacts, the influence of the exposure to Xe can be ignored in the following experiments.

Fig. 3.2 shows the STM images of a Si(111) surface observed at 600°C. These images were obtained after 30 minutes annealing at 600°C. Flat terraces were observed in a long range image Fig. 3.2 (a). The Si(111) surface was atomically flat after annealing at 600°C. The number of vacancies in the image Fig. 3.2 (b) was low as compared with that in the clean surface, Fig. 3.1 (a). This observation shows that the number of surface vacancies does not increase by only annealing at 600°C.

3.3 Surface Observation after Xe Ion Irradiation and Annealing

A Si(111) surface was irradiated with Xe ions using the ion gun in the STM chamber at room temperature. The irradiation was carried out at the following conditions: acceleration voltage (Va) was 1 kV, ion dose was 6.4×10^{12} ions/cm^2, the incident angle (θ) was 59° and chamber pressure

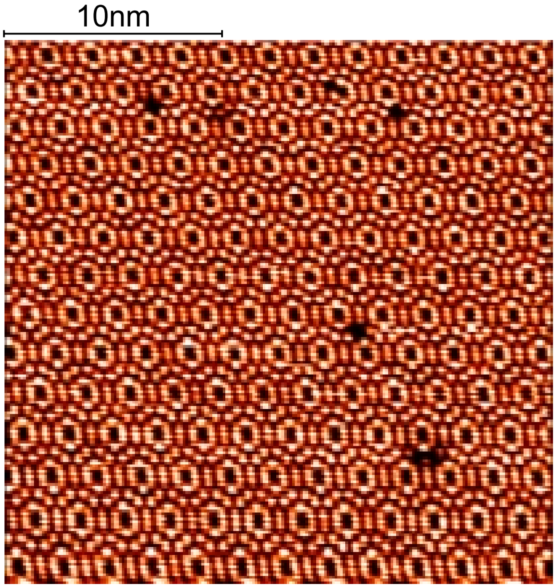

(a) Before exposure

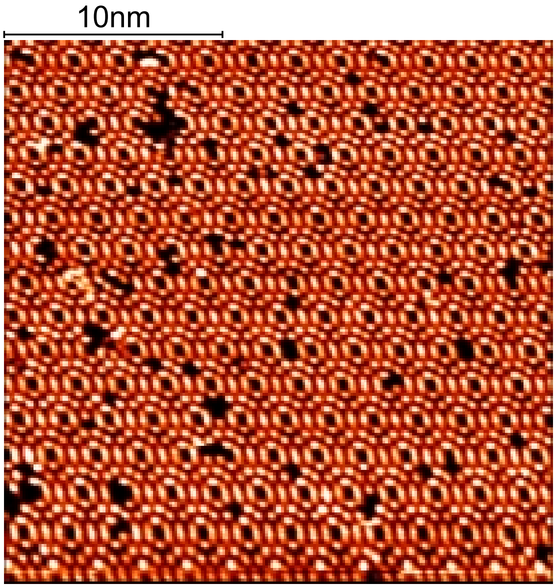

(b) After exposure

Figure 3.1: STM images of Si(111) clean surface before and after exposure to Xe.

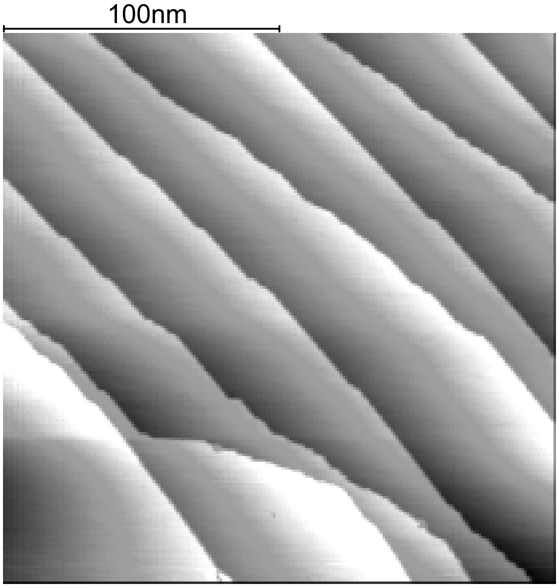

(a) Long range image

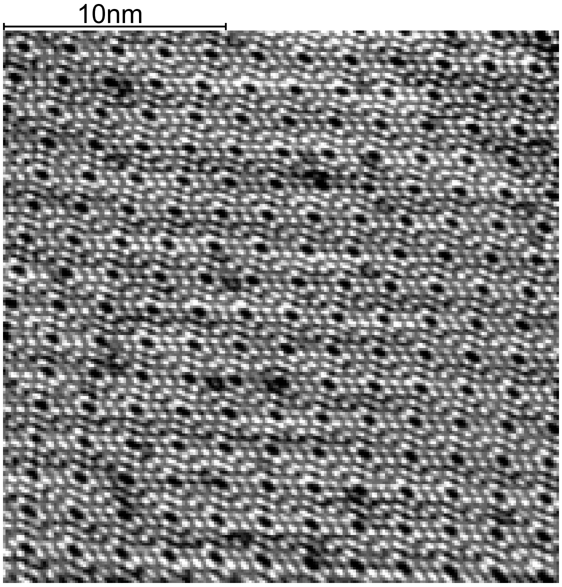

(b) High resolution image

Figure 3.2: STM images of Si(111) surface observed at 600°C.

(P_{Xe}) was 1×10^{-7} Torr. The irradiated surface was observed with STM at room temperature and was thermally annealed at 600°C and 700°C. During annealing, the surface was observed with STM.

According to the calculation with TRIM [38], the number of vacancies generated by a Xe ion is about 7. At a dose of 6.4×10^{12} ions/cm^2 the number of incident Xe ions in a 7×7 unit cell is 0.4. If all the vacancies were generated on the surface, the number of vacancies calculated in a 7×7 unit cell would be about 3. Therefore, the surface should not be completely amorphized at this ion dose. Fig. 3.3(a) shows the STM image of the surface obtained at room temperature after irradiation with 1 keV Xe ions to a dose of 6.4×10^{12} ions/cm^2. The surface image is disordered for the most part, because many ad-atoms are displaced from the 7×7 structure and are located on the surface. Nevertheless, several islands of vacancies and some corner holes can be clearly observed in this image.

This disordered surface was observed by VT-STM at annealing temperatures of 600°C and 700°C, respectively. Fig. 3.3(b) shows the STM image of the surface obtained at 600°C. Most of the displaced ad-atoms were recombined with the vacancies at this temperature and the reconstructed surface could be observed. Large vacancy islands were found in the 7×7 reconstructed surface. When a vacancy is generated by Xe ion impact, the dislodged surface atom becomes either a displaced ad-atom or an interstitial atom. The number of vacancies was larger than that of displaced ad-atoms. This indicates that many interstitial Si atoms are present in the bulk.

The amount of vacancies before irradiation is about 9% of the area. The amount of vacancies in this image, after irradiation and annealing at 600°C, is about 39%. Therefore, the amount of vacancies caused by Xe ion impacts is about 30%, i.e. the number of vacancies is about 518 in an area of 30×30 nm^2 shown in Fig. 3.3(b) which contains 1726 atoms. Because the number of incident Xe ions in the area of 30×30 nm^2 is about 58 at the dose of 6.4×10^{12} ions/cm^2, the number of vacancies caused by one Xe ion impact is about 9. The number of created vacancies is close to that calculated by TRIM. Fig. 3.3(c) shows the STM image of the

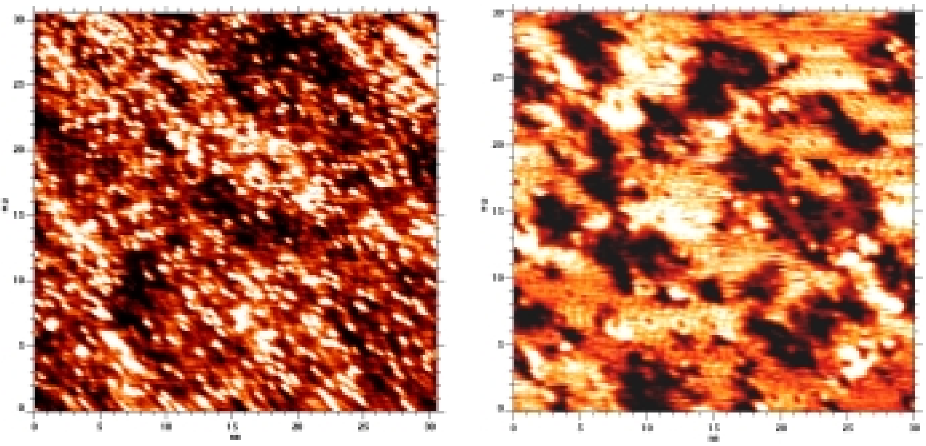

(a) At room temperature (b) At 600°C

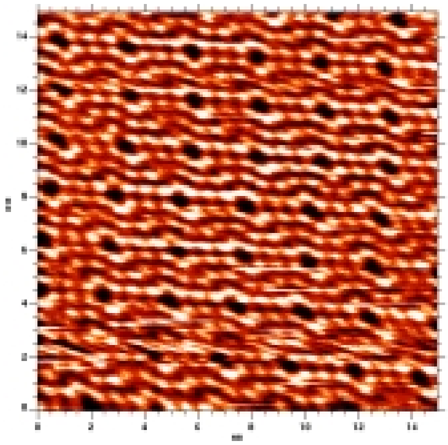

(c) At 700°C

Figure 3.3: STM images of Si(111) surface observed at various temperature. (Va=1 kV, Dose=6.4×10^{12} ions/cm^2)

surface obtained at 700°C. The surface had recovered completely and the 7×7 reconstructed surface was observed clearly. This indicates that the defects caused by the Xe ion impact are recovered completely by annealing at 700°C.

3.4 Atomic Process by a Single Xe Ion Impact

In order to understand ion-surface interactions, it is important to investigate a single trace formed by one ion impact on a solid surface. Single ion traces were created by Xe irradiation with ion dose lower than 1.5 $\times 10^{12}$ ions/cm^2. At these low doses, each ion impact trace can be individually distinguished in STM images. The irradiation was carried out at the following conditions: acceleration voltage (Va) was varied in the range 1-5 kV, the incident angle (θ) was 59° and chamber pressure (P_{Xe}) was lower than 5×10^{-8} Torr. The irradiated surface was observed with STM at room temperature and during thermal annealing at 400°C and 600°C.

3.4.1 STM Observation of Traces

Figs. 3.4(a-c) show STM images of Si(111) 7×7 surfaces irradiated with Xe ions at acceleration voltage of 1, 3 and 5 kV respectively. Xe ions bombarded the surface from the upper left side of the images at room temperature. The ion dose was about 1.2×10^{12} ions/cm^2 and the number of incident Xe ions in the area of 25×25 nm^2 was about 7. A few traces with diameters of about 20 Å can be observed in these images. The number of the traces is of the same order with that calculated from the ion dose, indicating that these are single ion traces formed by a Xe ion impact. At all impact energies, the size of these traces was almost the same and their shapes were elliptic, with the longer diameters in the incident ion direction. However, the number of displaced surface ad-atoms increased with impact energy. The displaced ad-atoms were found under the right side of the traces. The displaced surface atoms were created in

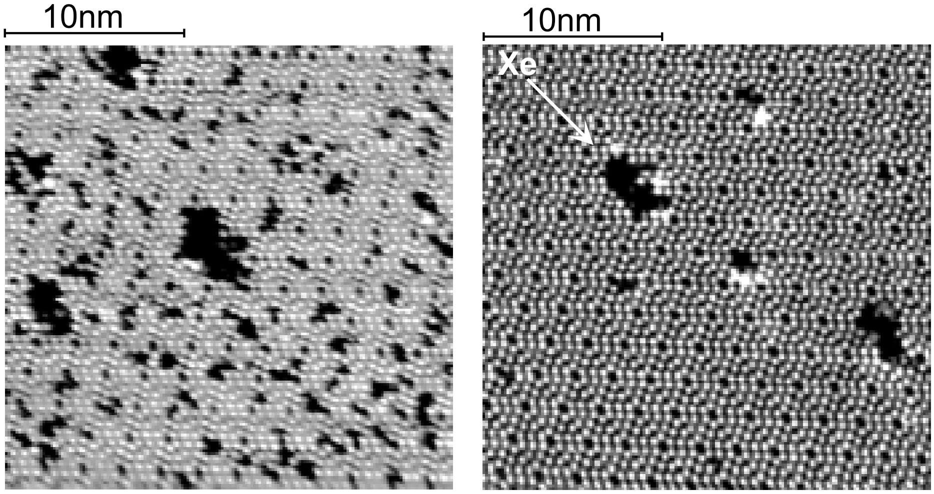

(a) Va=1 kV (b) Va=3 kV

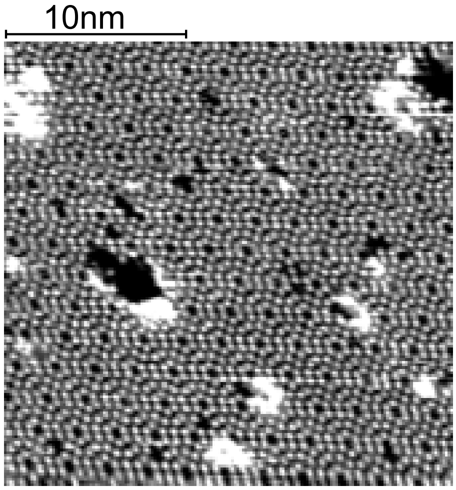

(c) Va=5 kV

Figure 3.4: STM images of a Si(111) 7×7 surfaces irradiated with Xe ions at room temperature. (Dose=1.2×10^{12} ions/cm^2)

the forward direction of the ion impacts.

3.4.2 MD Simulation of Xe Ion Impact

Fig. 3.5 shows the damage formation calculated by Molecular Dynamics (MD) simulation for Xe ions with various impact energies. For this simulation, the Stillinger-Weber (SW) model potential [39] was applied to interactions between Si atoms and the Ziegler-Biersack-Littmark (ZBL) model potential [40] was applied to interactions between Si and Xe atoms. The substrate was Si(100), and the incident angle was 60°. Dark circles in the images show the displaced Si atoms.

The damage in the bulk increases with impact energy. However, the extent of surface damage was almost the same - about 20 Å for all conditions. These results agree well with STM observations (Fig. 3.4). It should be noted that only surface defects can be observed with STM. This study shows that the sizes of surface defects were almost the same even when more defects were created in the bulk at higher impact energy.

3.5 Vacancy Cluster Formation

3.5.1 Diffusion of Vacancies during Annealing

Fig. 3.6 shows the Si(111) 7×7 surface after Xe irradiation at room temperature and after annealing. The impact energy was 3 keV, ion dose was 1.2×10^{12} ions/cm^2 and annealing time was about 30 minutes. After annealing at 400°C, many new vacancies have appeared on the surface. This indicates that a noticeable amount of vacancies that were formed in the bulk by ion impacts were able to diffuse from the bulk toward the surface, because the surface is a natural sink for vacancies. The enthalpy of migration of a vacancy in Si is relatively low, 0.33 eV, and vacancies diffuse rapidly in the bulk [41]. The activation energy of migration of an interstitial Si atom in Si is -3.1 eV and the diffusivity is

$$d_i = 100 \exp\left(\frac{-3.1}{\mathrm{k}T}\right) \quad \mathrm{cm}^2/\mathrm{sec}, \tag{3.1}$$

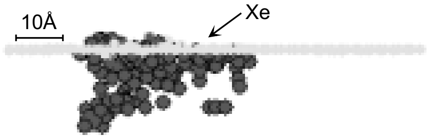

(a) Va=1 kV

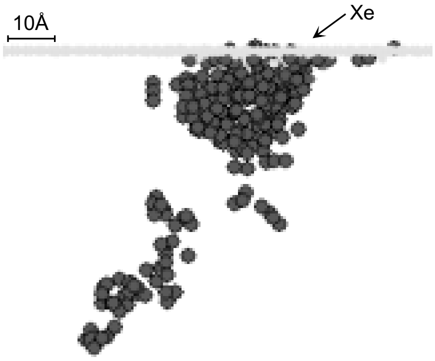

(b) Va=3 kV

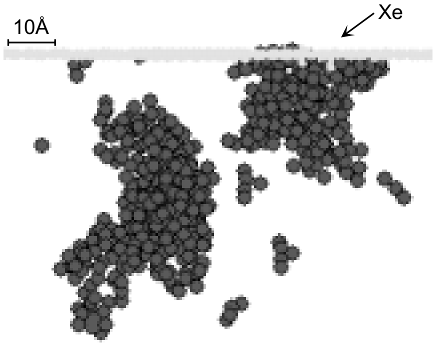

(c) Va=5 kV

Figure 3.5: The damage formation (displaced Si atoms) calculated by Molecular-Dynamics (MD) simulation for Xe ions with various impact energies.

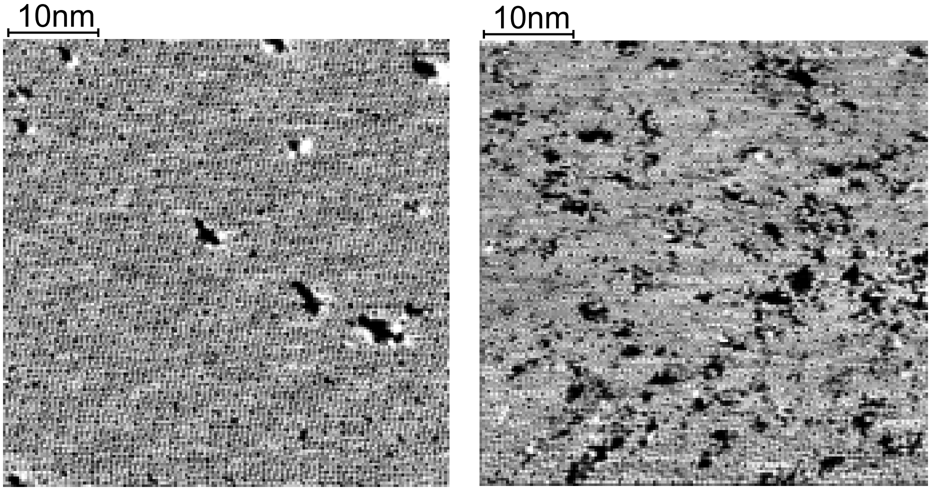

(a) At room temperature

(b) At 400°C

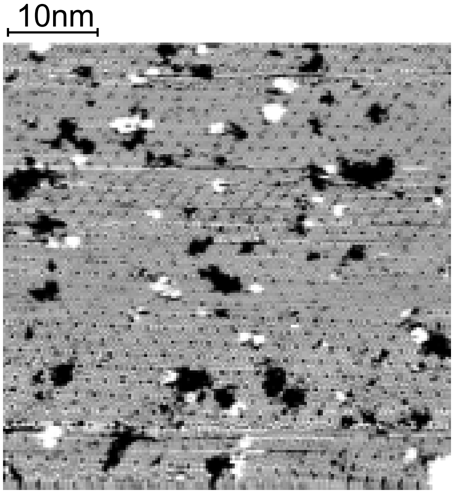

(c) At 600°C

Figure 3.6: Annealed Si(111) surface after Xe ion irradiation. (Va=3 kV, Dose=1.2×10^{12} ions/cm^2, annealed for 30 minutes)

where k is Boltzmann's constant (eV/K) and T is temperature (K) [42]. The diffusion length of an interstitial Si atom is

$$L = \sqrt{d_i \times t} \quad \text{cm}, \tag{3.2}$$

where t is annealing time in seconds. At 400°C, the diffusion length is 0.1 Å for 30 minutes annealing. The interstitial atoms generated together with the vacancies remain in the bulk because the depth of penetration is of the order of 10 Å.

The activation energy of a surface vacancy, such as a missing ad-atom on Si(111) 7×7 surface, is about 2eV [43]. This energy is higher than the migration energy of a vacancy in the bulk (0.33eV). Therefore, the surface vacancies could not migrate at this temperature and are distributed randomly on the surface. At 600°C, however, the vacancies at the surface migrate, aggregate and form large vacancy clusters.

3.5.2 Impact Energy Dependence

Fig. 3.7 shows Xe-irradiated Si(111) 7×7 surface after annealing at 600°C. The impact energy was 1 keV, 3 keV, and 5 keV, ion dose was 1.5×10^{12} ions/cm^2, 1.2×10^{12} ions/cm^2, and 1.2×10^{12} ions/cm^2, respectively. Annealing time was about 30 minutes. After annealing at 600°C, vacancy clusters were observed for these impact energies. The sizes of the vacancy clusters seemed to be same for all impact energies, despite the fact that the maximum impact energy was 5 times higher than the lowest one.

Fig. 3.8 shows a comparison between the number of vacancies as a function of impact energy, as calculated with TRIM, and as measured by STM. The lower line represents the number of missing ad-atoms as observed by STM at 600°C. At 1 kV, the number of the missing ad-atoms is comparable to the number of vacancies calculated with TRIM. This suggests that all vacancies formed by ion impacts in both the surface and the bulk have diffused toward the surface. Because the damage was formed very near the surface at 1 kV, all the vacancies could diffuse toward the surface without recombination with interstitial atoms. At

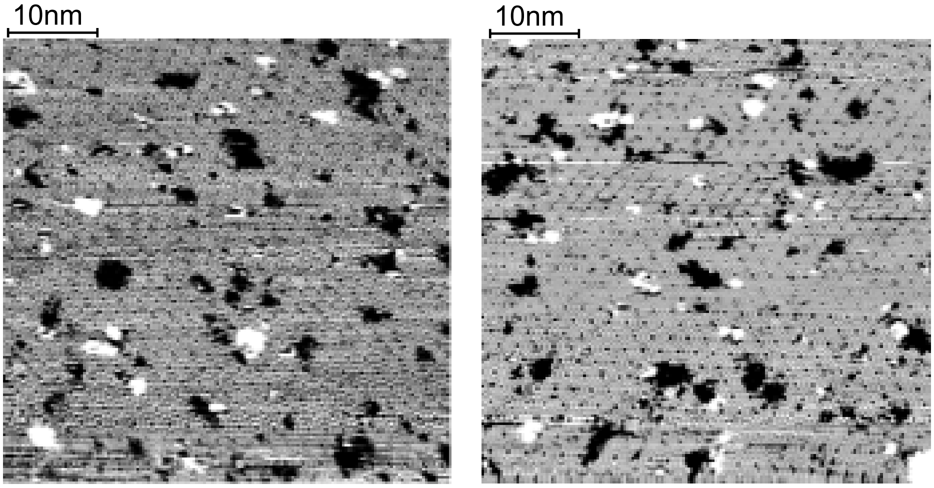

(a) Va=1 kV
(Dose=1.5×10^{12} ions/cm^2)

(b) Va=3 kV
(Dose=1.2×10^{12} ions/cm^2)

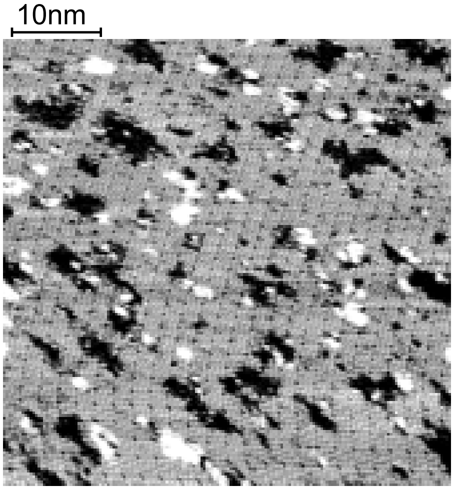

(c) Va=5 kV
(Dose=1.2×10^{12} ions/cm^2)

Figure 3.7: Xe-irradiated Si(111) 7×7 surface after annealing at 600°C. (Annealed for 30 minutes)

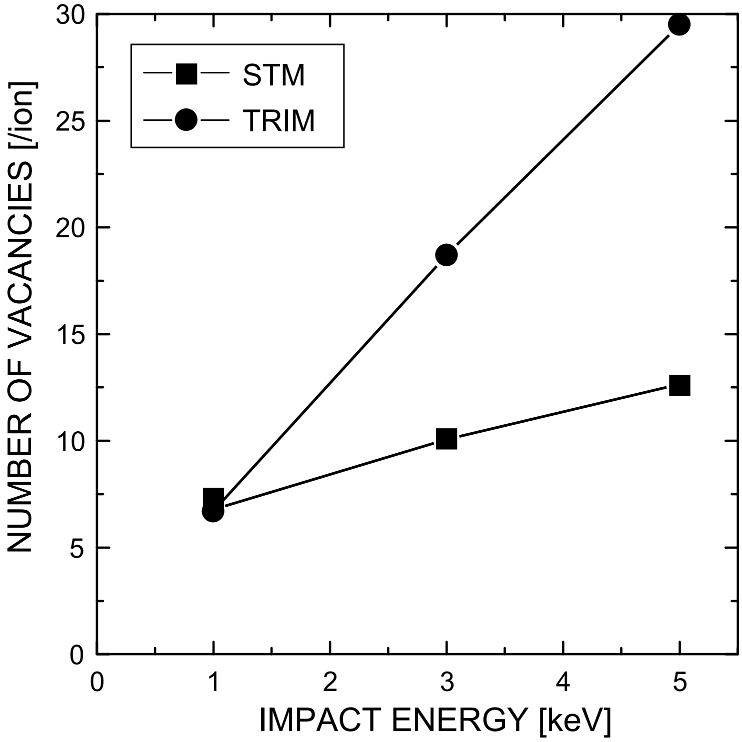

Figure 3.8: Impact energy dependence of the number of vacancies. Circle points show the number of vacancies calculated with TRIM. Square points show the number of missing ad-atoms in the STM images at 600°C.

higher energies, however, the number of the missing ad-atoms observed by STM was less than the numbers of vacancies calculated with TRIM. This suggests that not all vacancies in the bulk have diffused toward the surface. The vacancies in the near surface layer could diffuse toward the surface, but the vacancies in the deeper layers could not reach the surface and recombined with the interstitial atoms. The penetration depth was about 10 Å at 1 kV. Therefore, the depth of the layer from where vacancies can reach the surface is up to 10 Å. This layer will be referred to as "shallow".

3.5.3 Size Distribution of Vacancy Clusters

Fig. 3.9 shows the size histogram of vacancy clusters formed at 600°C in an area of 100×100 nm^2 on a surface irradiated with Xe ions at 1 kV. The size of the vacancy cluster shows the number of missing ad-atoms in this cluster. The number of missing ad-atoms was calculated from the size of individual dark areas in the STM image. Vacancy clusters of size smaller than 5 were ignored from the analysis, because such small dark areas might be considered as vacancies caused by neutral Xe exposure or errors during STM observation. The ion dose was about 1.5×10^{12} ions/cm^2 and the number of incident Xe ions in the area of 100×100 nm^2 was about 150. The sum of counts in the histogram was 91 (ignoring sizes of 4 and smaller) and the mean size of the vacancy clusters was about 10. The number of the vacancy clusters was close to the number of ion impacts calculated from the ion doses and the sizes of the vacancy clusters were also almost similar to the number of vacancies calculated with TRIM. Therefore, it can be assumed that each vacancy cluster was constituted from vacancies formed by a single Xe ion impact. A few very large vacancy clusters were observed, which we believe to have been formed from several nearby Xe ion impacts.

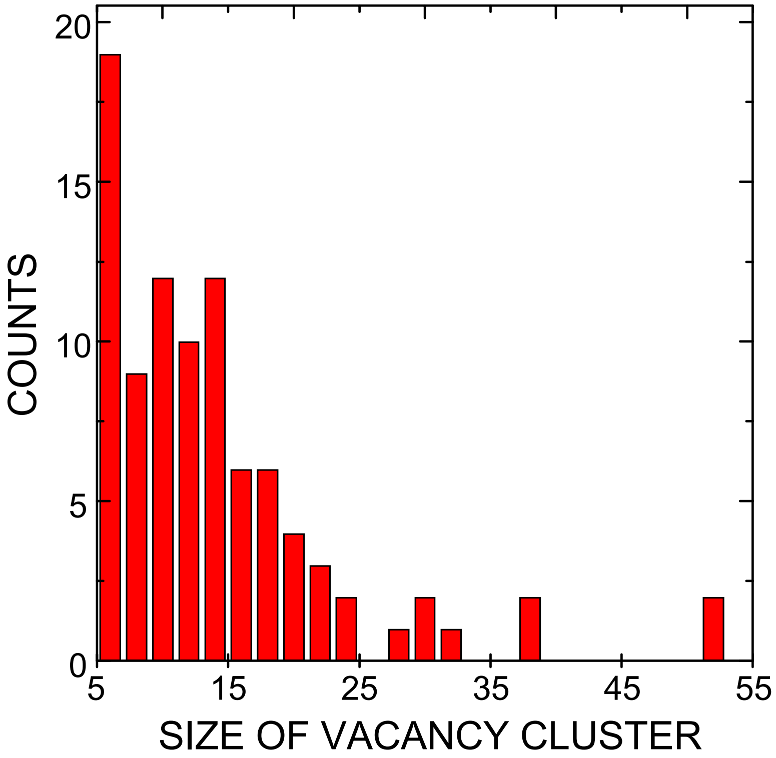

Figure 3.9: The size histogram of vacancy clusters at 600°C. Vacancy clusters of size smaller than 5 were ignored from the analysis.

3.6 Vacancy Cluster Migration

3.6.1 Migration of Surface Atoms

Figs. 3.10(a) and (b) are a series of images of same area obtained at 600°C after irradiation with 1 keV Xe ions to a dose of 1.5×10^{12} ions/cm^2. Fig. 3.10(b) was observed 60 sec after (a). Many vacancy clusters were observed in these images and their movement could be seen. These two images show that large vacancy clusters did not move, but the small vacancy clusters enclosed by white circles moved or changed shape at 600°C.

In order to understand the mechanism of the behavior of vacancy clusters, each atom was observed individually. Figs. 3.10(c) and (d) are the high-resolution images of (a) and (b), respectively. Si atoms can be observed clearly in these images and the atoms in the 7×7 structure are enclosed by black or white circles. The white-circled atom in (c) was not found in (d) and the white-circled atoms in (d) were not found in (c). One of the white-circled atoms in (d) came from the white-circled atom in (c) and the other atoms came from the interstitial Si atoms near the boundary between the vacancy cluster and the 7×7 structure. These results confirm that the atoms on the boundary between vacancy clusters and the 7×7 structure can migrate at 600°C. When these boundary atoms between vacancy clusters and the 7×7 structure migrate, vacancy clusters can move.

3.6.2 Migration Model of Vacancy Cluster

The mobility of the vacancy clusters changes with size. Fig. 3.11 shows the movement of vacancy clusters caused by the behavior of the boundary atoms. The number of vacancies in a small vacancy cluster is less than that of the boundary atoms. When a few boundary atoms migrate, the vacancies before the movement are filled by migrated atoms and vacancies caused by the escape of boundary atoms form a new vacancy cluster. The small vacancy cluster can move when a few boundary atoms migrate.

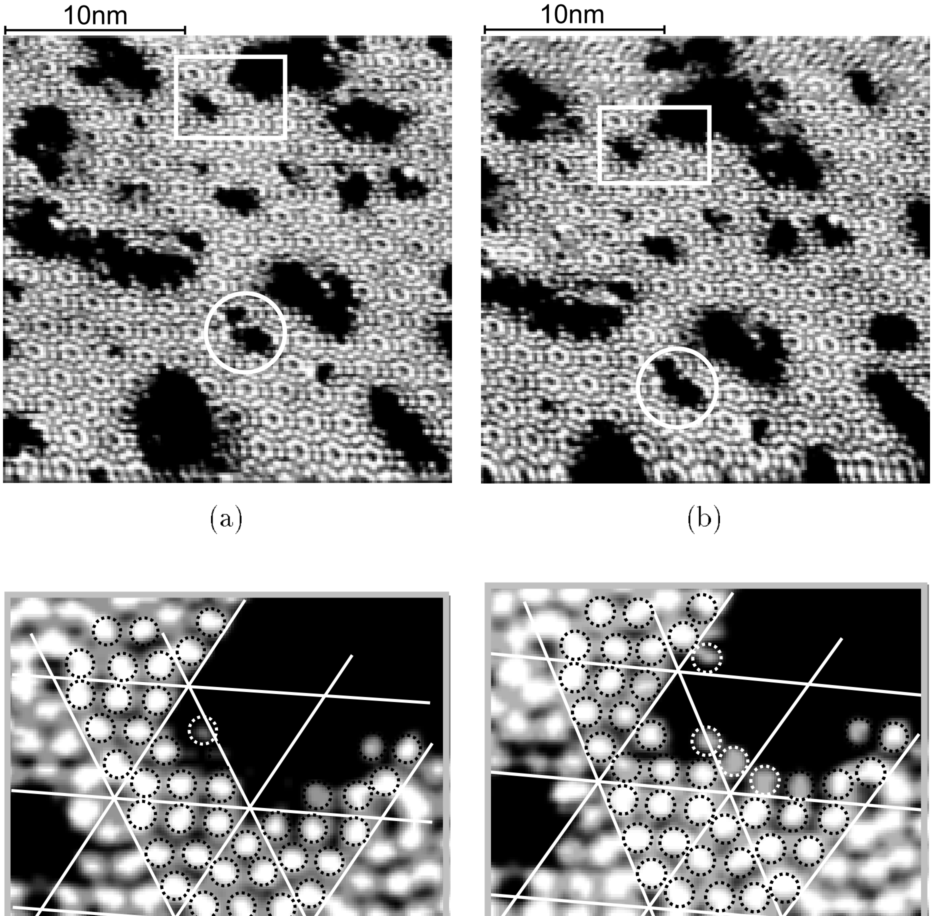

(a) (b)

(c) (d)

Figure 3.10: A series of images of same area obtained at 600°C. (b) was observed at following late 60 sec after (a). (c) and (d) were high-resolution images of (a) and (b), respectively.

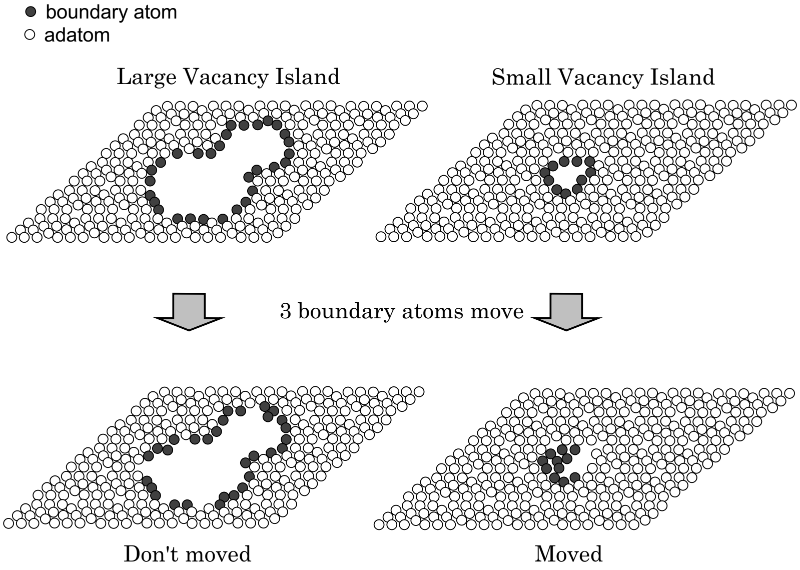

Figure 3.11: Movement of vacancy islands caused by the behavior of boundary atoms.

However, because the number of vacancies in a large vacancy cluster is larger than that of the boundary atoms, the vacancies cannot be filled with migrated boundary atoms. The large vacancy cluster cannot move when a few boundary atoms migrate. Therefore, small vacancy clusters could move rapidly but large vacancy clusters moved slowly at 600°C. These considerations point to the following mechanism: The small vacancy clusters caused by Xe ion impacts moved rapidly. They reached large vacancy clusters, where they were absorbed, and which became stable at 600°C.

3.6.3 Migration by Long Time Annealing

In order to confirm that the small vacancy clusters caused by Xe ion impacts were absorbed by large vacancy clusters, the sample was annealed at 600°C for a long time and the surface was observed with STM intermittently. Fig. 3.12 shows a series of STM images of the same area observed after annealing at different times at 600°C. Fig. 3.12(a) was the image of the surface irradiated with Xe ions at 1 kV and annealed for 60 minutes at 600°C. Figs. 3.12(b), (c) and (d) were obtained 20 minutes, 44 minutes and 98 minutes after (a). The small vacancy cluster enclosed with a white-triangle in (a) was absorbed by a neighboring large vacancy cluster in (b). Moreover, the white-circled small vacancy clusters in (a) disappeared before (c), though all the large vacancy clusters remained in (d). This indicates that small vacancy clusters were recombined with interstitial atoms, rapidly.

As a result of long annealing, the large vacancy clusters enclosed with white-squares in (a) changed the shape in (d). One was separated into two vacancy clusters and the other combined with a neighboring vacancy cluster. This shows that the large vacancy clusters can move and change shape by boundary atom migration with prolonged annealing.

Because the steps are formed on the line connecting corner holes in a 7×7 reconstructed surface, it is expected that the boundary lines between 7×7 structure and vacancy cluster are formed on the lines connecting corner holes which are in a direction from the $<\bar{1}10>$ family. Fig. 3.13

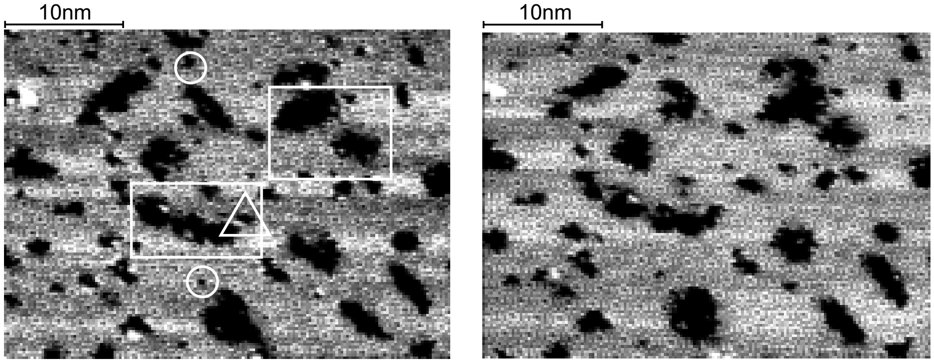

(a) (b) After 20 minutes

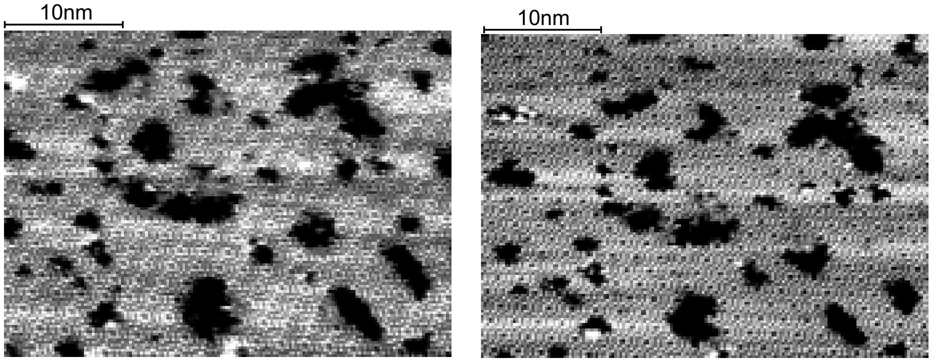

(c) After 44 minutes (d) After 98 minutes

Figure 3.12: A series of STM images of the same area observed after annealing at different times at 600°C. (Va=1 kV, Dose=1.5×10^{12} ions/cm^2)

shows a series of STM images of a part of a large vacancy cluster observed after annealing at different times at 600°C. The boundary lines were formed on $[\bar{1}01]$ and $[01\bar{1}]$ directions and the angle at the corner of the vacancy cluster is about 120° in Fig. 3.13(a). As can be observed, however, the corner collapsed on one side in (b) and the angle of the corner became 60° exactly in (c). This is the angle between $[\bar{1}01]$ and $[\bar{1}10]$ in the Si structure. Moreover, a boundary line extended toward $[\bar{1}01]$ direction in (d). This transformation indicates that the corner of the vacancy cluster was more stable at 60° than at 120° and large vacancy clusters also change to some stable shapes by prolonged annealing at 600°C.

3.7 Vacancy Recombination

Fig. 3.14 shows a series of STM images of the same area observed after annealing at different times at 650°C. Fig. 3.14(a) is the image of the surface irradiated with Xe ions at 650°C at impact energy - 1 keV after 11 minutes annealing. Two vacancy clusters are observed. Figs. 3.14(b) and (c) were obtained 2 minutes and 16 minutes after (a). The size of vacancy clusters in (b) decreased as compared to (a) and they disappeared in (c). The disappearance of these clusters indicates that at 650°C interstitial atoms diffuse toward the surface and recombine with the surface vacancies. The diffusion length of an interstitial Si atom for 30 minutes annealing at this temperature is about 150 Å according to equation 3.1. This distance is longer than the penetration depth of Xe ion at 5 kV (27 Å). Therefore, at this temperature all the interstitial atoms have diffused toward the surface.

In order to understand the time dependence of the number of surface vacancies during annealing at 650°C, the status of the sites in a series of STM images of same area was analyzed. One site corresponds to an area occupied by an ad-atom originally. The number of the analyzed sites was 810 and the sites were divided into two kinds of status that were ad-atom and vacancy. If a status of a site flipped from ad-atom to vacancy or from vacancy to ad-atom in comparison with a previous image,

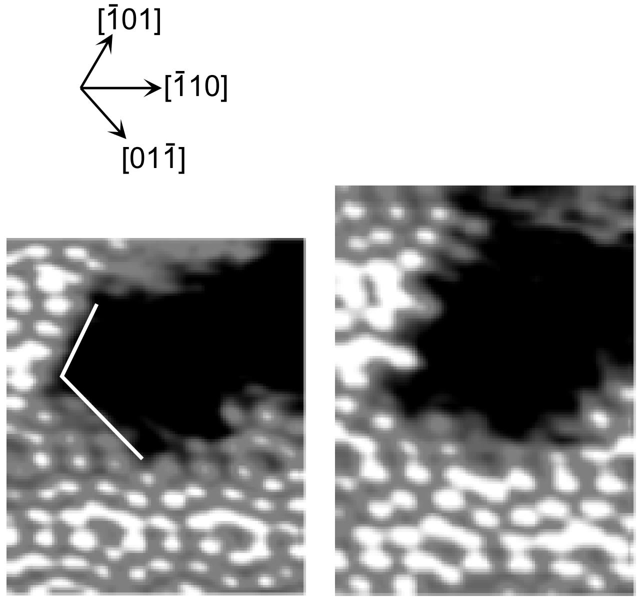

(a) (b) After 34 minutes

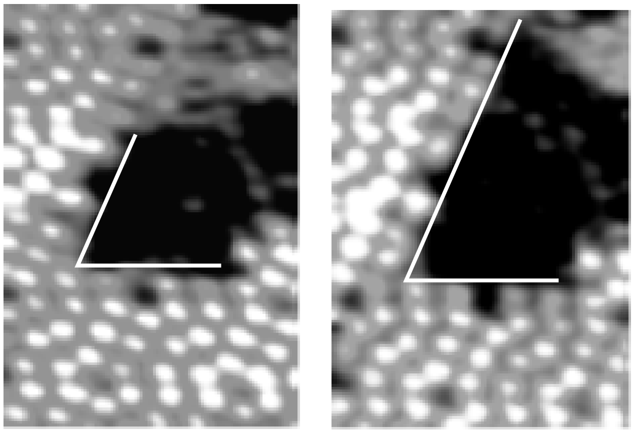

(c) After 78 minutes (d) After 90 minutes

Figure 3.13: A series of STM images of a part of a large vacancy cluster observed after annealing at different times at 600°C.

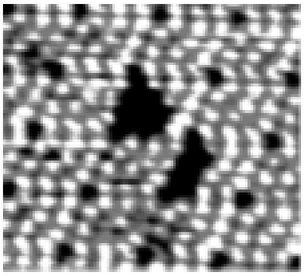

(a)

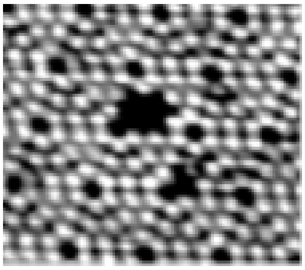

(b) After 2 minutes

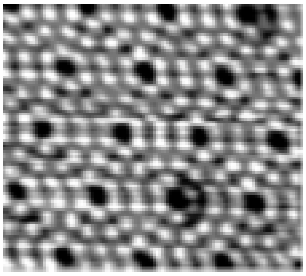

(c) After 16 minutes

Figure 3.14: A series of STM images of the same area observed after annealing at different times at 650°C.

the flipped site was called "flip". Fig. 3.15 shows the annealing time dependence of the number of surface vacancies and "flips" at 650°C. The number of vacancies decreased exponentially with annealing time. This can be explained with following model. The time derivative of the number of vacancies is inversely proportional to the probability of recombination with interstitial atoms. When the interstitial atoms which appeared on the surface recombine with surface vacancies rapidly, the probability of recombination is proportional to the number of interstitial atoms in the bulk. Because the number of vacancies created by an ion impact is equal to that of interstitial atoms and all the vacancies appeared on the surface at 650°C in case of the surface bombarded at 1 kV, the number of interstitial atoms in the bulk is equal to that of the surface vacancies. Therefore, the time derivative of the number of vacancies is inversely proportional to the number of the surface vacancies. The time derivative of the number of vacancies is

$$\frac{\mathrm{d}v(t)}{\mathrm{d}t} = -\mathrm{k}v(t), \tag{3.3}$$

where $v(t)$ is the number of vacancies and k is a constant. The solution for $v(t)$ is, therefore,

$$v(t) = \mathrm{A}\mathrm{e}^{-\mathrm{k}t}. \tag{3.4}$$

Equation 3.4 shows that the number of vacancies decreases exponentially with annealing time. When equation 3.4 is applied as a fit function of the graph in Fig. 3.15, the constant (1/k) is about 12 minutes.

The number of "flips" decreased slightly with annealing time. During a sudden decrease in vacancies, many sites flipped as a result of recombination of vacancies with interstitial atoms. After the number of vacancies became small, many sites were also flipped and the number of "flips" was similar to that of vacancies. At this time, only small vacancy clusters whose size was smaller than 5 remained, and all the vacancies in such small vacancy clusters occupied positions at the boundary. This result shows that the vacancies which occupied positions at the boundary exchanged neighboring atoms quickly.

Fig. 3.16 shows the annealing time dependence of the size of three

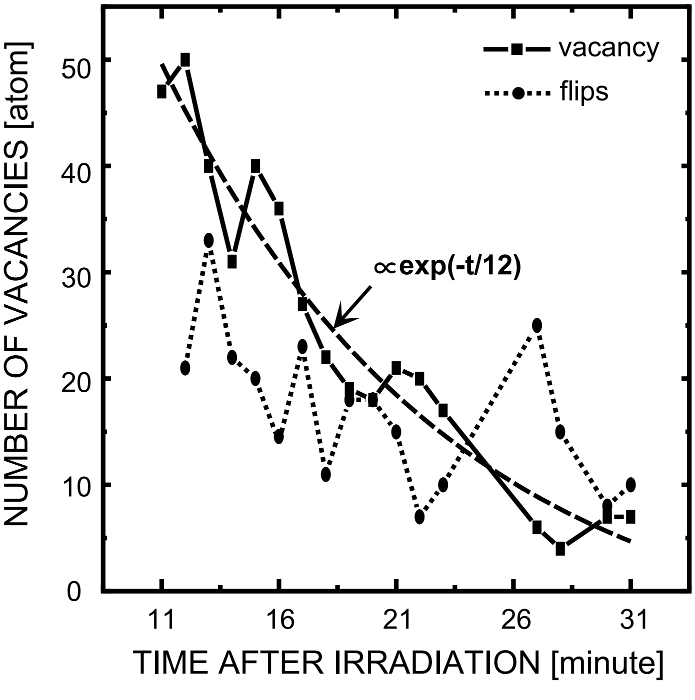

Figure 3.15: Annealing time dependence of the number of vacancies and "flips" at 650°C.

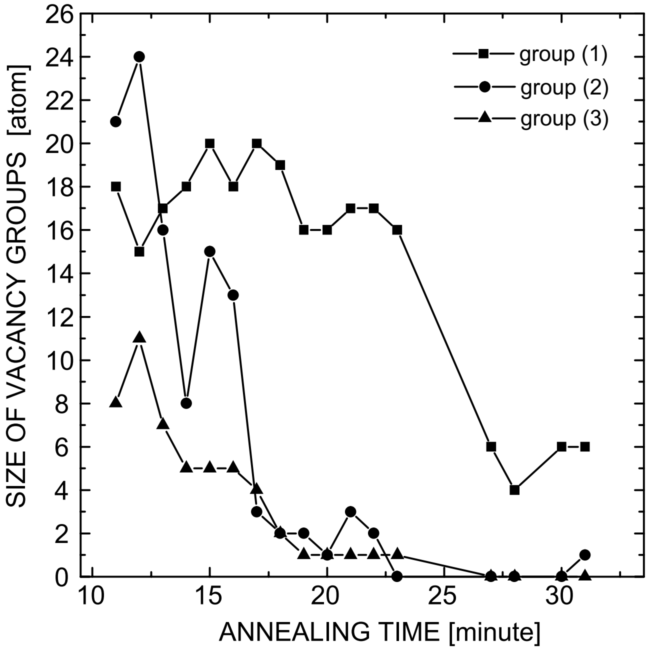

Figure 3.16: Annealing time dependence of the number of vacancies included in vacancy clusters at 650°C.

vacancy groups at 650°C. The size of a vacancy group is the number of vacancies created by an ion impact at 1 kV. Because these vacancy groups were at some distance from each other, they were removed individually. The size of vacancy groups decreased with annealing time, intermittently. When the size was more than 12, it decreased slightly. When the size was between 6 and 12, it decreased suddenly. After the size reached 6, it also decreased slightly.

Fig. 3.17 shows the size distribution of vacancy clusters included in a vacancy group after annealing at 650°C. This vacancy group is called "group (1)" in Fig. 3.16. This group included two vacancy clusters whose sizes were 2 and 16. One vacancy cluster combined with another after 17 minutes annealing. The new vacancy cluster, however, was separated into two vacancy clusters and a few vacancies were removed after 19 minutes. Thus, the vacancy clusters repeated combination and separation, but the size of vacancy clusters was more than 12 or less than 6. This result suggests that the vacancy clusters, whose size was between 6 and 12, were unstable. Therefore, when the group size was between 6 and 12, it decreased suddenly. Finally, the sizes of vacancy clusters became less than 2 and the vacancies were removed.

Fig. 3.18 shows an annealing model of defects formed by single ion impact. At 1 kV, vacancies and interstitial atoms are created in the "shallow" layer. At 400°C, vacancies can diffuse toward the surface, but interstitial atoms remain in bulk. At 600°C, surface vacancies can migrate and create a vacancy cluster on the surface. At 650°C, interstitial atoms can diffuse and recombine with the surface vacancies. In the case of 3 kV, vacancies and interstitial atoms are created in the shallow layer and also in a deeper layer. At 400°C, vacancies can diffuse toward surface, but deeper vacancies recombine with interstitial atoms in bulk. At 600°C, surface vacancies can migrate and create a vacancy cluster on a surface. The size of the vacancy cluster corresponds to the number of vacancies created in the "shallow" layer. At 650°C, interstitial atoms can diffuse and recombine with the surface vacancies.

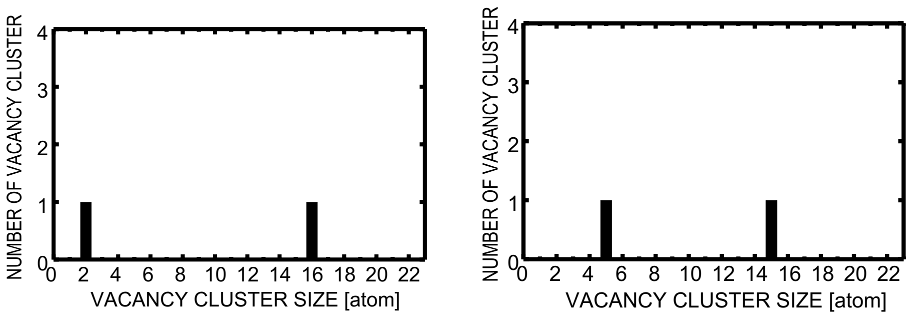

(a) After 11 minutes

(b) After 15 minutes

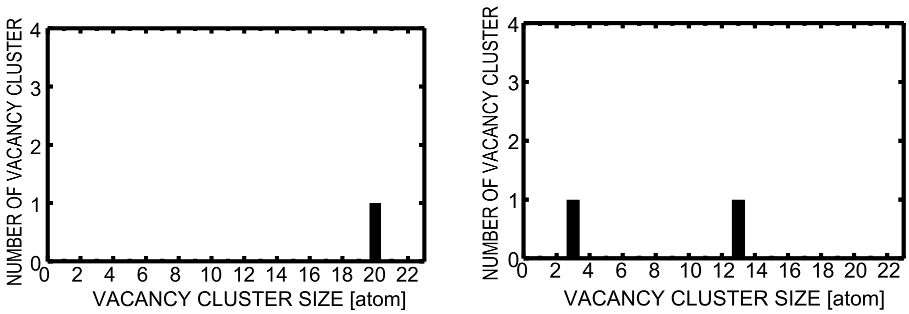

(c) After 17 minutes

(d) After 19 minutes

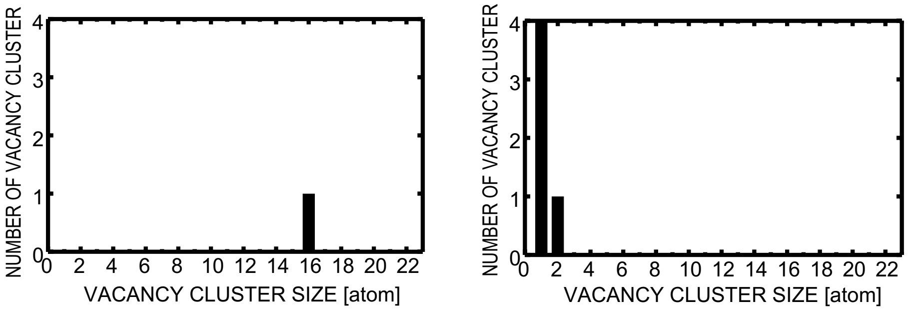

(e) After 23 minutes

(f) After 27 minutes

Figure 3.17: Size distribution of vacancy clusters included in the vacancy group (1) after annealing at 650°C.

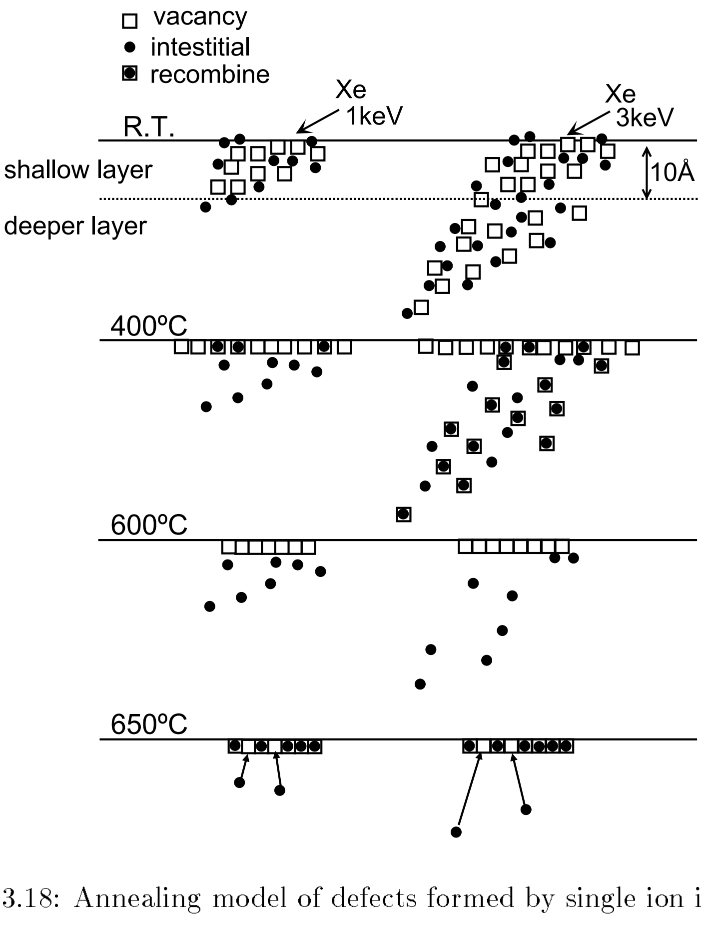

Figure 3.18: Annealing model of defects formed by single ion impact.

3.8 Summary

In this chapter, the atomic structure of surface defects created by a Xe ion impact and the thermal annealing process were described.

1. The STM image of a clean Si(111) 7×7 surface was obtained clearly. The Si(111) surface was atomically flat, so that we could discuss a single trace of an ion impact at an atomic level.
2. Traces with diameters of about 20 Å can be observed on Si(111) surfaces after Xe irradiation. At all impact energies (1 kV, 3 kV, and 5 kV), the size of these traces was almost the same and their shapes were elliptic, with the longer diameters in the incident ion direction. The displaced surface atoms were created in the forward direction of the ion impacts.
3. After 400°C annealing, vacancies can diffuse toward the surface, but interstitial atoms remain in bulk. Upon annealing to 600°C, vacancy clusters are formed whose size corresponds to the number of vacancies created in the "shallow" sub-surface layer.
4. The small vacancy clusters caused by Xe ion impacts moved rapidly by behavior of atoms on a boundary between a vacancy cluster and the 7×7 structure during 600°C annealing. They reached large vacancy clusters, where they were absorbed by large vacancy clusters. The large vacancy clusters also change to some stable shapes by long time annealing at 600°C.
5. At 650°C, interstitial atoms recombine with the surface vacancies and the size of vacancy cluster decreased. The defects caused by the Xe ion impact were recovered completely by annealing at 700°C.

Chapter 4

Surface Effects by Cluster Ion Impact

4.1 Introduction

Cluster ion beams offer new surface modification processes because of their unique interaction between cluster atoms and solid surfaces. For example, surface smoothing [19, 20] and shallow implantation [21] by cluster ion beam have been demonstrated. In order to reveal such cluster-surface interaction, a single trace formed by a cluster ion impact on a solid surface was investigated using STM.

The traces created by Ar cluster ion impact on Si were observed and the annealing process of the traces was investigated. Because the mean size of Ar cluster is about 1000, it is expected that the typical effect caused by large cluster impact would occur. As well, Highly Oriented Pyrolitic Graphite (HOPG) surfaces irradiated with high energy carbon cluster ions were observed and the mechanism of the interaction between high energy small clusters and the surface was investigated. Because the traces created by various size carbon cluster ions can be observed, the threshold size of clusters to find a difference between monomer impacts and cluster impacts can be investigated. We believe that the threshold size gives us information to reveal the mechanism of the cluster-surface interaction.

4.2 Large Cluster Ion Impact

4.2.1 Ar Cluster Ion Irradiation on Si(111)

In order to understand the irradiation effect of cluster ions, it is necessary to compare them with those of monomer ions. Single traces of a cluster ion impact were compared with those of a monomer ion impact. Fig. 4.1(a) shows an STM image of Si(111) surfaces irradiated with Ar cluster ions at acceleration voltage of 8 kV. The supplied gas pressure was 5 atm, the ion dose was about 6.3×10^{10} ions/cm^2, and the number of incident Ar cluster ions in the area of 200×200 nm^2 was about 25. About 12 doughnut shape traces can be observed in this image. The number of traces is of the same order with that calculated from the ion dose, indicating that these are single ion traces formed by an Ar cluster ion impact. The traces of cluster ion impact had a quite different shape from those of the monomer, as shown in chapter 3. Small hole shape traces were observed in the case of monomer ion irradiation, while large doughnut shape traces were observed in the case of cluster ion irradiation.

Fig. 4.1(b) shows a high resolution image and a cross section diagram of a large doughnut-like trace with an outer diameter of about 60 Å and an inner diameter of about 25 Å. The cross-sectional image of the doughnut-like trace shows that the traces created by the cluster ion impacts were a crater shape with a big hole in center. The outer rim of the crater is 2.4 Å above the substrate surface level. This indicates again that cluster impact processes are quite different from a summation of separate monomer impacts.

Fig. 4.2 shows a distribution of the diameter of craters created by Ar cluster impacts at 8 kV. The diameter of craters has a wide distribution from 50 Å to 200 Å and the mean diameter is about 80 Å. This wide distribution can be caused by the size distribution of cluster ion and extremely large traces may be created by double charged cluster ions. If

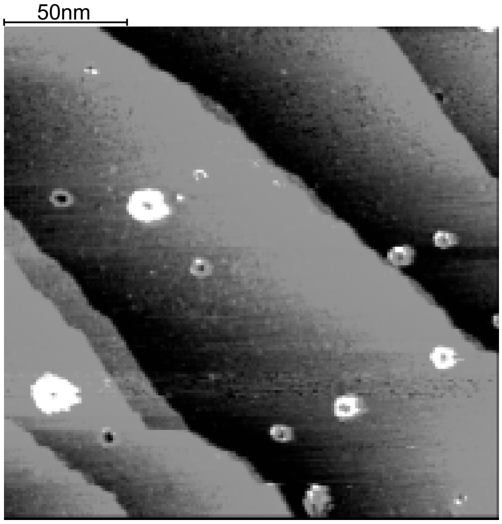

(a) Long range image

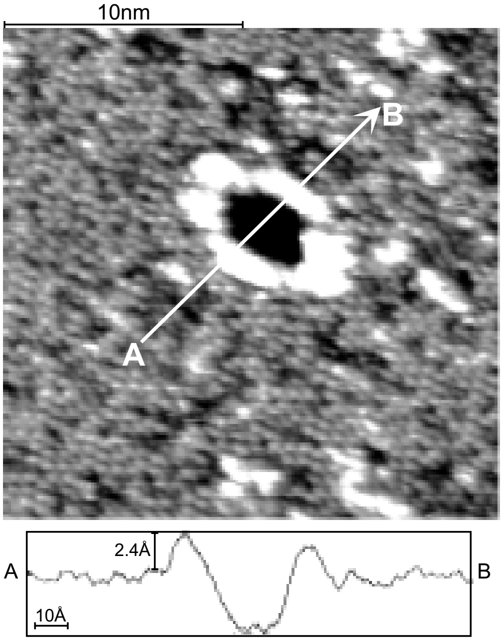

(b) High resolution image and cross section diagram

Figure 4.1: STM images of Si(111) surface irradiated with Ar cluster ions at room temperature. (Va=8 kV, Dose=6.3×10^{10} ions/cm^2)

the size of clusters is 1000, the energy per an Ar atom is 8 eV. Though the energy per atoms is very low, large traces are created by Ar cluster impacts. This result may be caused by the multiple-collision effect.

4.2.2 Crater Formation Mechanism

Fig. 4.3 shows snapshots of an Ar_{688} cluster impacting with the Si(100) surface calculated by MD simulation. The impact energy is 6.88 keV. For this simulation, the Stillinger-Weber (SW) model potential [39] was applied to interactions between Si atoms and the Buckingham model potential [44] was applied to interactions both between Si and Ar atoms and between Ar and Ar atoms. Fig. 4.3(a) is the initial state, the initial temperature of the Ar cluster is 0 K, and the initial kinetic energy of an Ar atom constituted the cluster is 10 eV/atom. Figs. 4.3(b) and (c) correspond to 1.54 ps and 4.62 ps after the impact. The Ar cluster penetrated and created hemispherical damage in the target at 1.54 ps. After the Ar atoms escape as vapor from the target, a hole remains at the center of the damage region and a crater is created. This crater formation agrees with the result of STM observation as shown in Fig. 4.1.

These results allow us to discuss the process of cluster ion impact and crater formation. Fig. 4.4 shows a model of the mechanism of crater formation. In the case of monomer ion impact, the damage region is created by a cascade collision [45]. When a cluster ion hits the target surface, the energy of the cluster ion spreads out symmetrically from the impact point to the target. The distributed energy causes hemispherical damage in the target, and target atoms around that surface region move. This results in the shape of the outer rim of the crater.

Fig. 4.5 shows the time dependence of the penetration depth of the cluster and of the crater size, which is calculated by a molecular-dynamics simulation. Ar cluster ion, with a size of 688 atoms, was accelerated to 6.88 kV. The depth and radius of the crater alongside increase with the penetration depth of the cluster, and this indicates the symmetrical crater formation. At the maximum penetration depth of the cluster, when the

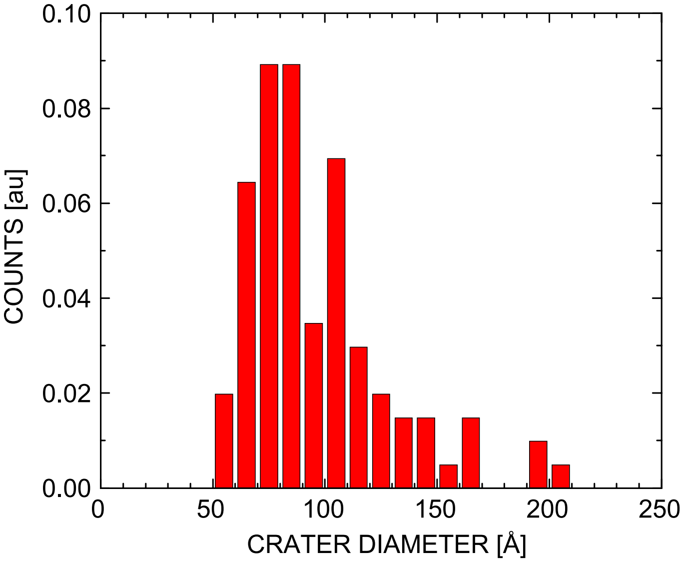

Figure 4.2: Distribution of crater diameter. (Va=8 kV)

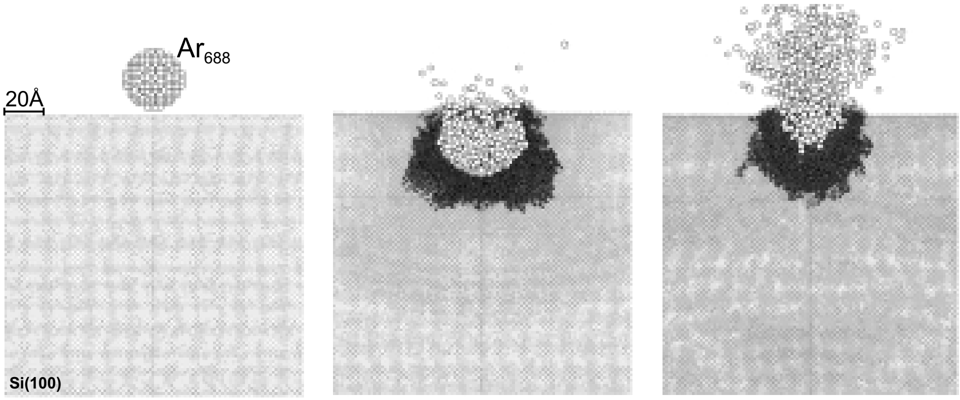

(a) t=0 ps (b) t=1.54 ps (c) t=4.62 ps

Figure 4.3: Snapshots of an Ar_{688} cluster impacting with the Si(100) surface calculated by MD simulation. (Va=6.88 kV)

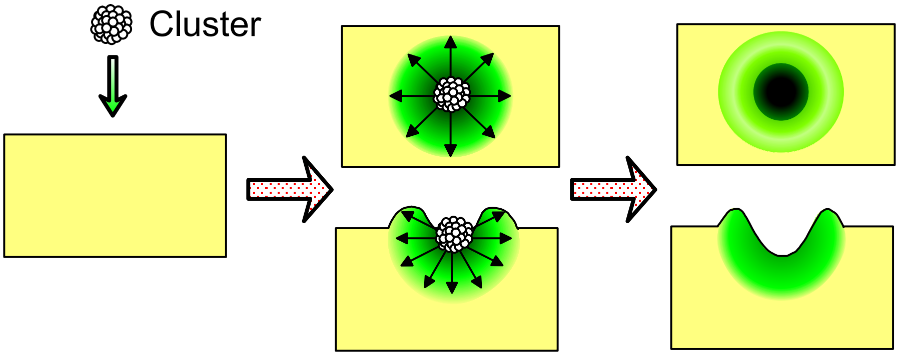

Figure 4.4: Model of the mechanism of crater formation.

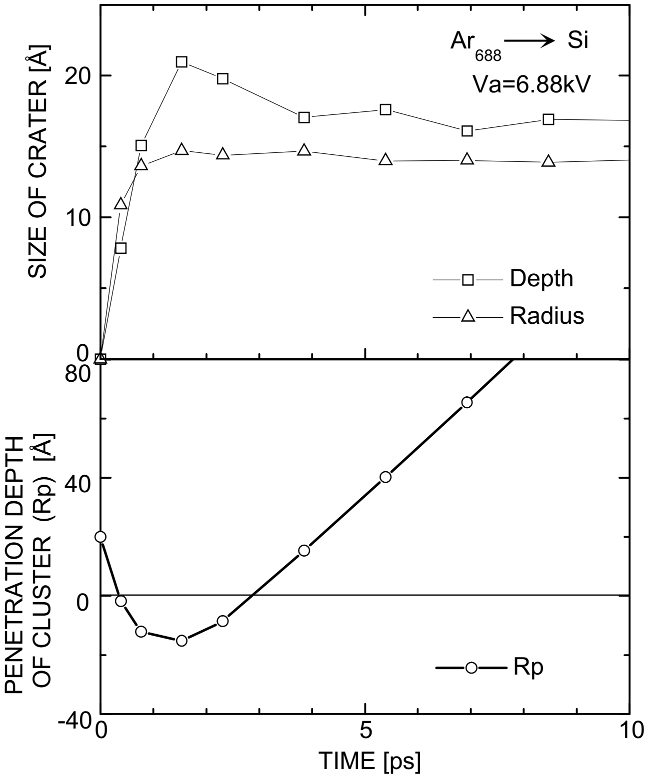

Figure 4.5: Time dependence of the penetration depth of the cluster and of the crater size.

time is 1.5 ps, the depth of the crater reaches a maximum. Because the radius of the crater is constant and the depth of the crater is reduced slightly after this time, the crater formation is completed after 1.5 ps. The time of crater formation is longer than that of cascade collision. After Ar cluster atoms escape as vapor from the target, a hole remains at the center of damage region and a crater is created.

4.2.3 Annealing of Craters

The Si(111) surface was annealed after irradiation with Ar cluster ions at 8 kV. Figs. 4.6(a-d) shows STM images of the surface observed at various temperatures. The ion dose was 6.3×10^{10} ions/cm^2 and the annealing time was about 30 minutes. At 300°C, the shape of the craters was still that of the initial craters. At higher temperature, part of the outer rim of craters appears chipped. Then, at 600°C, the outer rim of the craters disappeared, but the holes remained. Fig. 4.7 shows larger magnification STM images and cross section diagrams of individual craters observed in Fig. 4.6. The chipped area of the rim increased and the height of the rim decreased with annealing temperature. At 600°C, the outer rim of the crater disappeared and the 7×7 reconstructed structure was observed at the site of the rim. This result shows that the hemispherical damage created by the cluster impact was removed at this temperature.

Fig. 4.8 shows a schematic model of crater formation and annealing after cluster impact. It summarizes the results presented in Figs. 4.6 and 4.7. A crater is formed by an Ar cluster impact and the shape is maintained after annealing at 300°C. Because the atoms constituting the rim of crater can migrate above 400°C, the outer rim of crater is gradually chipped away above 400°C. The outer rim of crater disappears and the hemispherical damage in the target is removed at 600°C, but the hole remains.

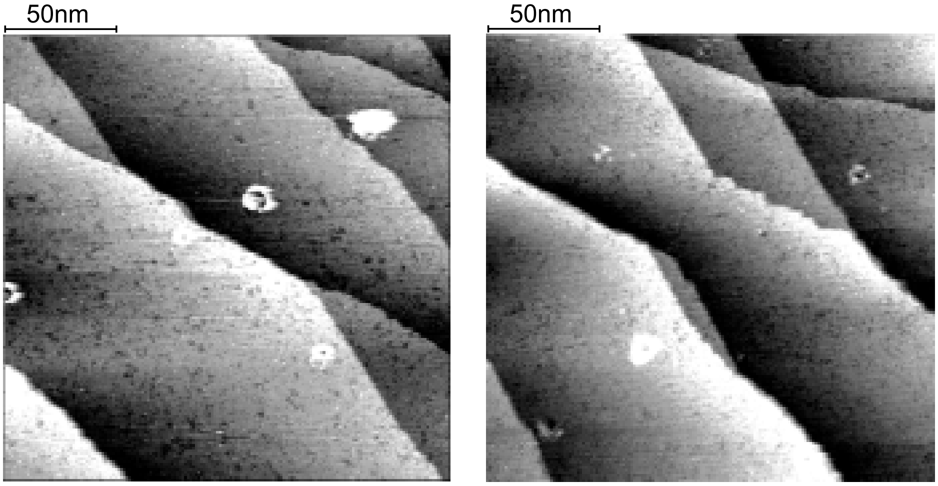

(a) At 300°C (b) At 400°C

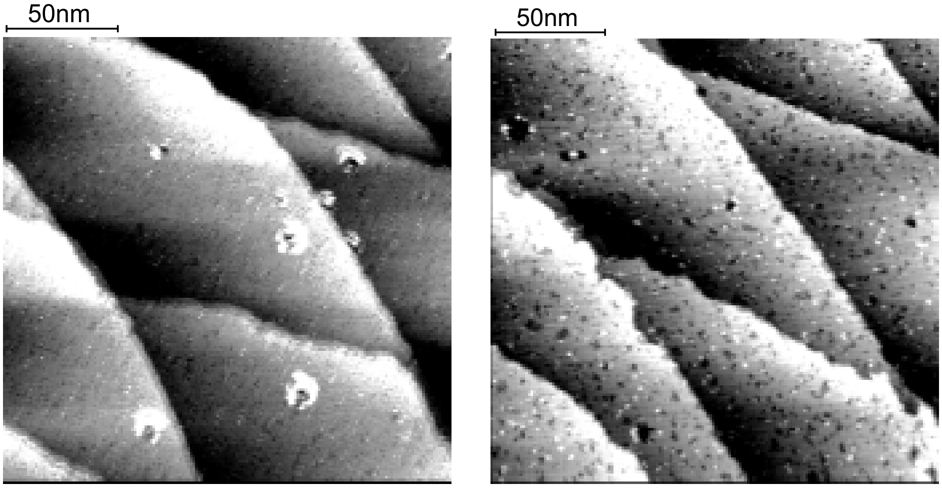

(c) At 500°C (d) At 600°C

Figure 4.6: STM images of Si(111) surface observed at the indicated temperatures after irradiation with Ar cluster ions. (Va=8 kV, Dose=6.3×10^{10} ions/cm^2)

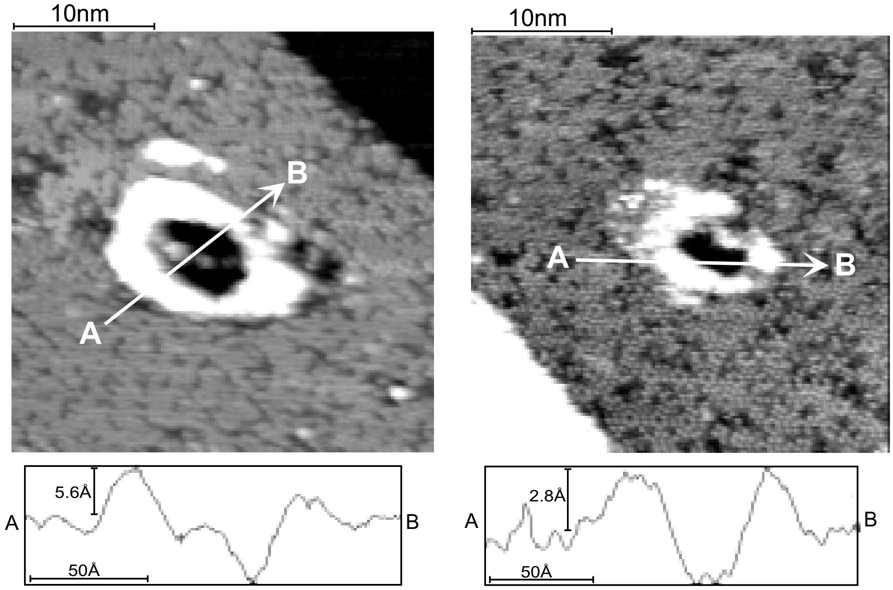

(a) At 300°C (b) At 400°C

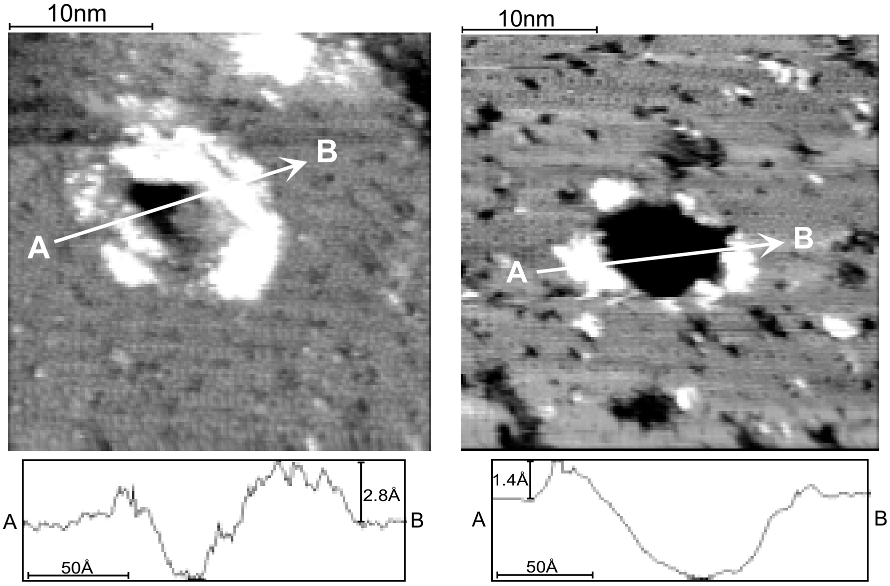

(c) At 500°C (d) At 600°C

Figure 4.7: Larger magnification STM images and cross section diagrams of craters observed at the indicated temperatures after irradiation with Ar cluster ions. (Va=8 kV, Dose=6.3×10^{10} ions/cm^2)

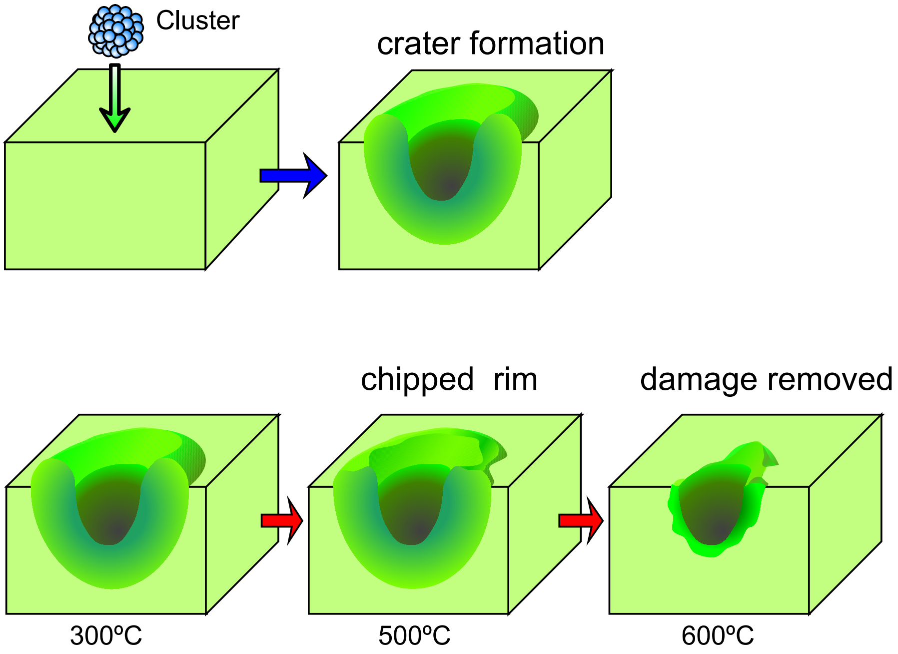

Figure 4.8: Schematic model of crater formation and annealing after cluster impact.

4.3 Small Cluster Ion Impact

4.3.1 C_{60} Ion Irradiation on HOPG

HOPG has the characteristics of high conductivity, chemical stability and an atomically flat surface. Because of these properties, this material can be examined by STM in air and was therefore selected as a target for these series of experiments. Fig. 4.9(a) shows an STM image of an HOPG surface before irradiation. Mechanically polished Pt-Ir tips were used for the probe. The conditions for these observations were: tunneling current was constant at 0.7 nA and bias voltage was +1.0V. This image indicates that the HOPG surface was very flat. Fig. 4.9(b) shows a high resolution image of the HOPG surface. Bright spots were observed on a pattern of a triangle lattice. It is known that such a pattern is observed on an HOPG surface, resulting from the electronic state of surface atoms [46]. This atomic resolution image shows that the HOPG surface was atomically flat, and we can then discuss traces of ion impact on an atomic level. This surface can be obtained quite easily by means of cleavage and is suitable for STM observation in air.

Fig. 4.10(a) is an STM image of an HOPG surface irradiated with C_{60} ions. The impact energy was 300 keV and the dose was 5×10^{10} ions/cm^2. Craters and large hills, with diameter of about 150 Å, were observed on this surface. The observed area was a 5000×5000 Å square and the number of incident C_{60} ions in this area is 125 at a dose of 5×10^{10} ions/cm^2. The number of traces observed by STM was almost the same as the calculated number. Thus, the craters and the large hills observed by STM are the traces formed by the C_{60} ion impact with the surface. Fig. 4.10(b) is a high resolution image and a cross section diagram of a crater shown in Fig. 4.10(a). This profile image shows that the rim height of the crater was about 5 Å and the diameter was about 230 Å. The large crater shape traces are one of the typical consequences of high-density energy deposition and multiple-collision between cluster atoms and surface atoms at cluster ion impact. Formation of a crater by C_{60} impact indicates that

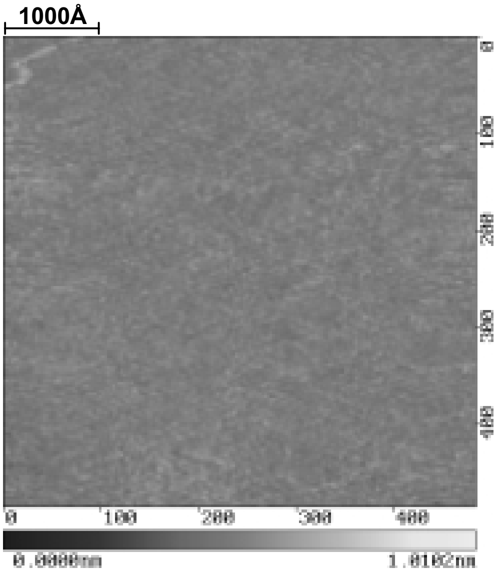

(a) Long range image

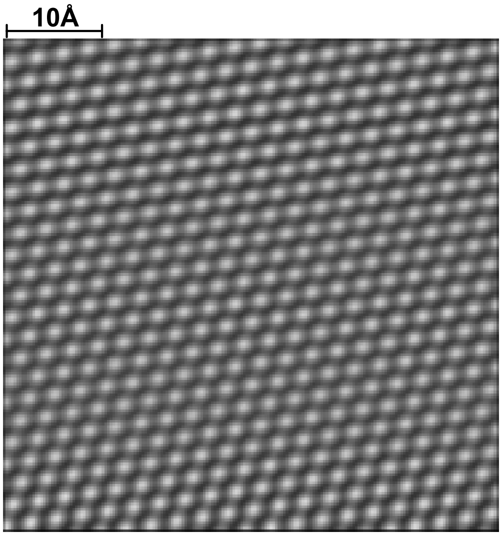

(b) High resolution image

Figure 4.9: STM images of an HOPG surface before irradiation.

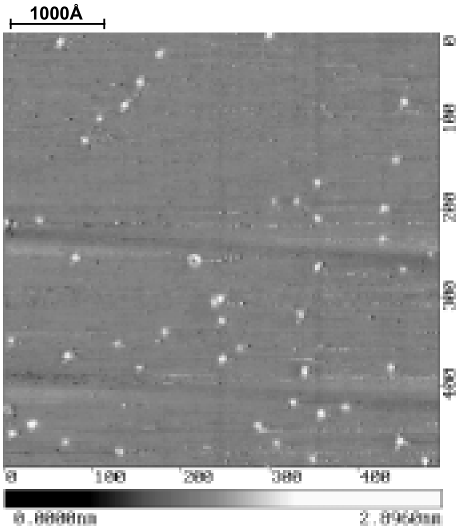

(a) Long range image

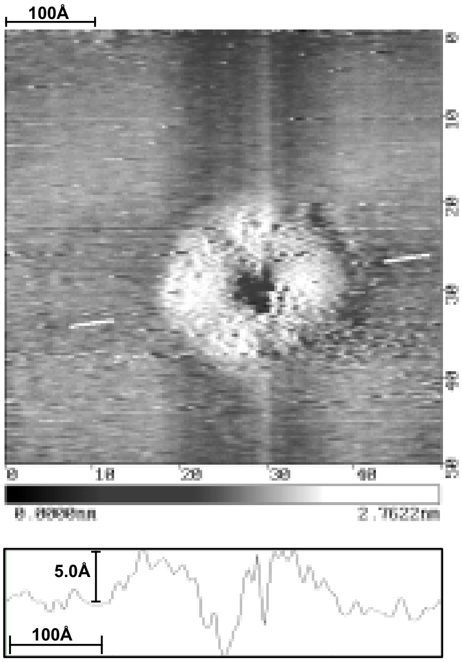

(b) High resolution image and cross section diagram

Figure 4.10: STM images of an HOPG surface irradiated by C_{60}. (Va=300 kV, Dose=5×10^{10} ions/cm^2)

the C_{60} impact process has the same effects.

4.3.2 Energy Dependence of the Trace Diameter

HOPG surfaces irradiated with C_{60} ions accelerated up to 600 kV were observed by STM. Double charged ions were accelerated to more than 400 kV. The ion doses were varied from 1×10^{10} to 1×10^{11} ions/cm^2. At these low doses, each ion impact trace can be distinguished from another in STM images. Fig. 4.11 shows the dependence of the trace area on acceleration energy on HOPG surfaces. The solid line is the nuclear stopping power of a carbon atom in graphite calculated using ZBL potential. In case of low velocity Ar cluster impact, the trace diameters were proportional to the cubic root of the acceleration energy [28], because the energy of Ar cluster ion is distributed symmetrically from the impact point to the target. However, the trace diameters of C_{60} impacts decrease with increasing acceleration energy above 3 keV/atom. This indicates that the amount of deposited energy near the surface decreases when the acceleration energy is above 3 keV/atom. High energy C_{60} ion penetrates the substrate deeply and forms deeper damage.

The square of the trace diameter is maximum at acceleration energy between 2 keV/atom and 3 keV/atom. This dependence is similar to that of nuclear stopping power on acceleration energy. The square of the trace diameter is equivalent of an area of damage on a surface. The stopping power of C_{60} is sixty times larger than the energy loss of a monomer ion near the surface. As the energy loss of C_{60} ions near the surface causes a large trace on surfaces, the trace size and the energy loss have same energy dependence.

Fig. 4.12 shows the damage formation calculated by molecular-dynamics (MD) simulation for C_{60} ions with various impact energies. Dark points are damaged atoms that are defined to have excess potential energy of more than 0.3 eV after 0.1 ps. A graphite target was irradiated with C_{60} ions. The impact energies were from 100 eV/atom to 5 keV/atom. Many-body potential proposed by Tersoff [47] was used for both substrate

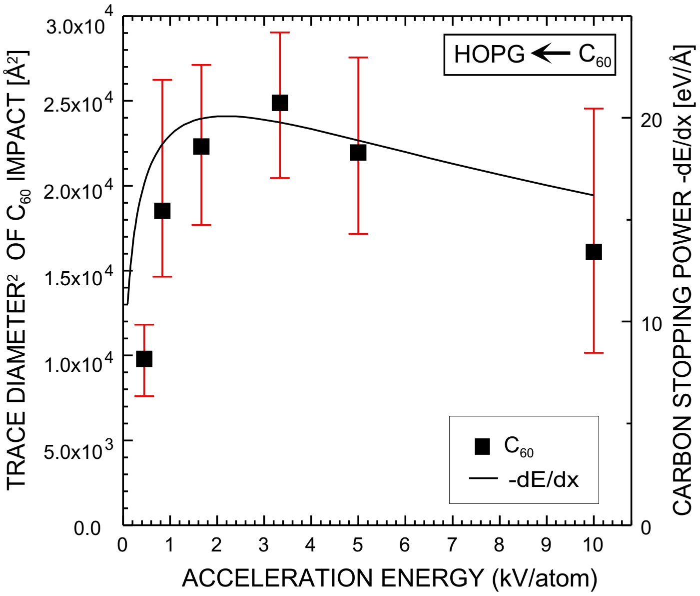

Figure 4.11: Dependence of trace area of C_{60} impact on an HOPG surface on acceleration voltage. The solid line is nuclear stopping power of a carbon atom in graphite calculated by using ZBL potential.

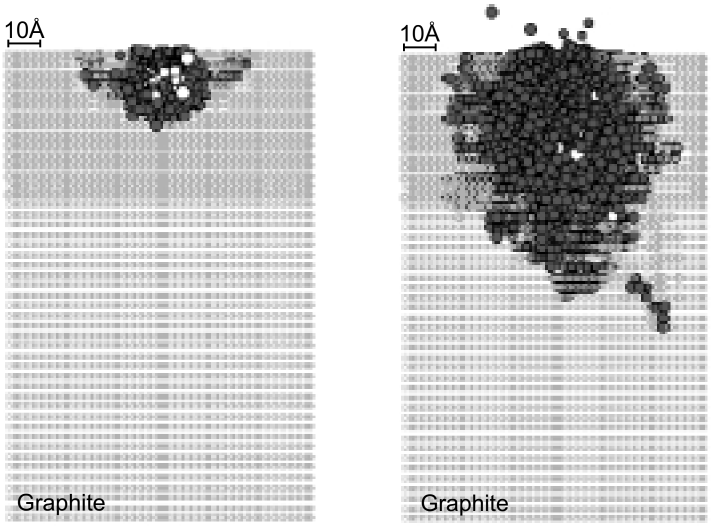

(a) Va=100 V/atom (b) Va=1 kV/atom

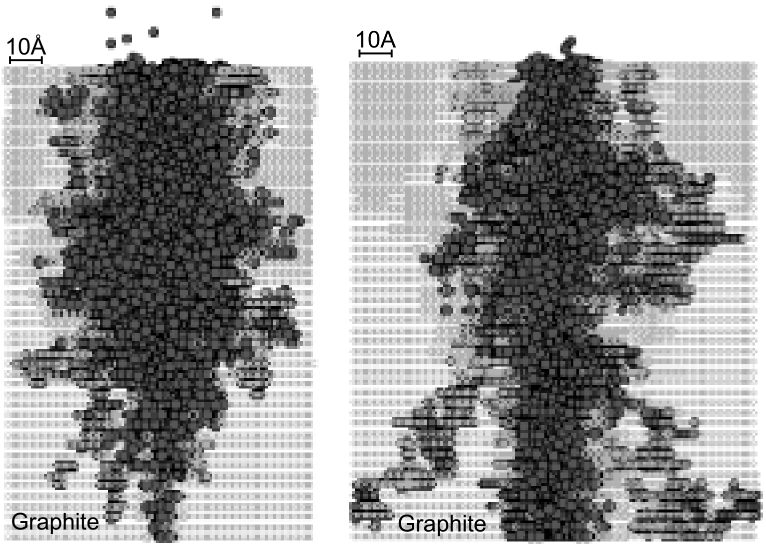

(c) Va=2 kV/atom (d) Va=5 kV/atom

Figure 4.12: The damage formation (displaced C atoms) calculated by Molecular-Dynamics (MD) simulation for C_{60} ions with various impact energies. Dark points are damaged atoms.

and C_{60} atoms. Two different damage formation mechanisms are found in these calculations. In the case of low energy impact, below 1 keV/atom, the C_{60} ion forms almost hemispherical damage. In the case of high energy impact, above 2 keV/atom, C_{60} ion forms cylindrical damage near the surface and scattered damage is created as a result of collision cascades at the end of projection range.

4.3.3 RBS Investigation of Defects

In order to investigate defects created by C_{60} ion irradiation, the number of disordered atoms was estimated from Rutherford Back Scattering (RBS) channeling spectra. Fig. 4.13 shows random and channeling RBS spectra from Si(100) substrates irradiated with C_{60} ions. The impact energy was 5 keV/atom and the ion dose was 1×10^{13} ions/cm^2. By using TRIM, the damage depth was calculated at about 150 Å for C_1 ions at an energy of 5 keV. The depth resolution of the RBS measurement is not sufficient to study the damage at a 150 Å. However, the number of disordered Si atoms can be estimated from the area of the surface peak, because the latter corresponds to the total number of defects [48]. Fig. 4.14 shows dependence of disordered Si atoms on atomic dose. The disordered atoms calculated by TRIM at impact energy of 5 keV is depicted as the monomer carbon ion irradiation.

In both monomer and C_{60} ion bombardment, the number of disordered atoms saturated for high atomic doses. When the whole surface area is completely bombarded at the high doses, the number of disordered atoms corresponds to the thickness of the damaged layer. The number of disordered atoms after C_{60} ion irradiation at the high doses was similar to that calculated by TRIM, and therefore there is no remarkable difference in the thickness of the damaged layer between C_{60} and monomer carbon ion irradiation. This means that the penetration depth of C_{60} ion is the same as that of monomer ion at the same velocity. The number of disordered atoms after C_{60} ion irradiation saturated at an atomic dose several times lower than that calculated by TRIM. Such fast saturation

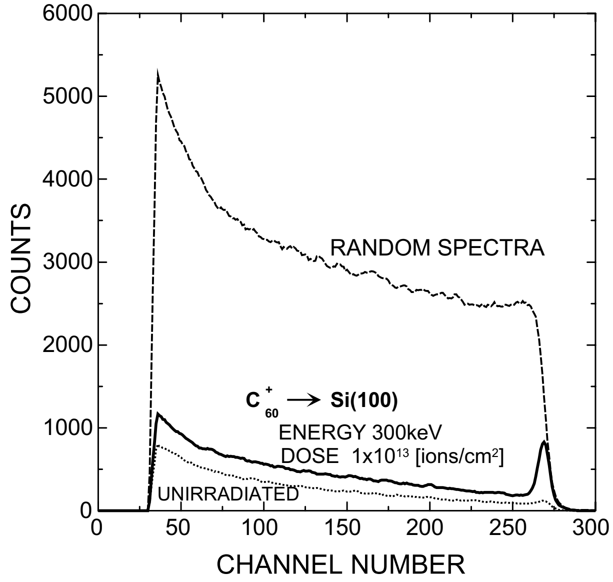

(a)

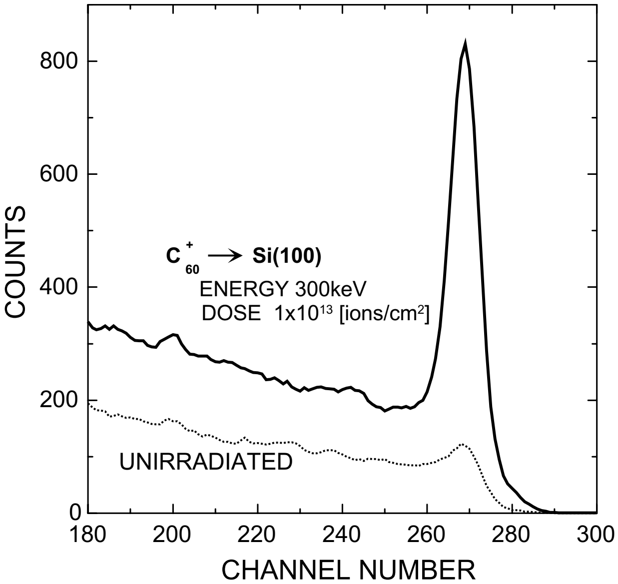

(b)

Figure 4.13: Random and channeling RBS spectra from Si(100) substrates irradiated with C_{60} ions. (Va=300 kV, Dose=1×10^{13} ions/cm^2)

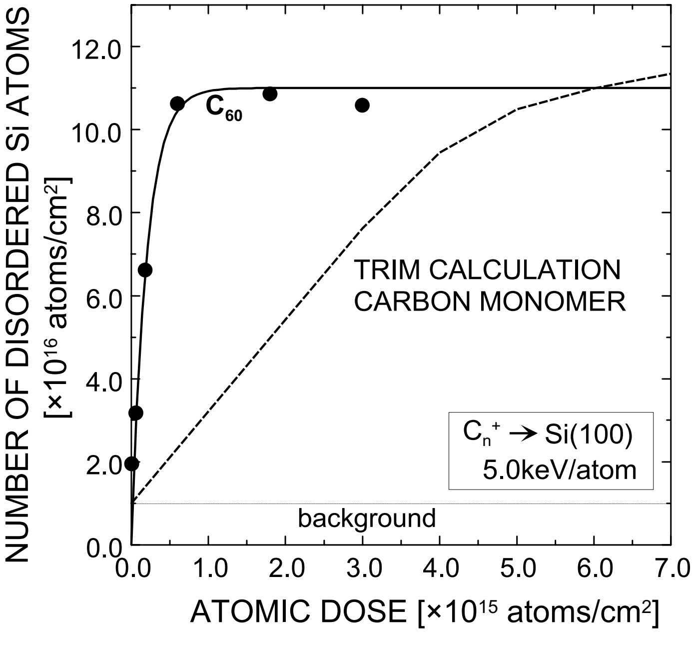

Figure 4.14: Dependence of disordered Si atoms on atomic dose.

shows that the number of defects produced by C_{60} is several times larger than that by carbon monomers at the same velocity [49].

4.3.4 Damage Formation Mechanism

Fig. 4.15 shows a schematic model of damage formation by C_{60} ion impacts. Damage formation by C_{60} ion impacts differs according to ion energy. In case of low energy, C_{60} is broken up near the surface. At the same time, multiple-collision occurred between the incident atoms and the substrate atoms, because the cross section is large enough to produce many collisions between the atoms. Because of the multiple-collision, all the energy of the C_{60} ion is dissipated in the near surface region and forms an almost hemispherical damage. This phenomenon is quite similar to crater formation by low energy Ar cluster impact, as shown in Fig. 4.4. We believe that the formation of hemispherical damage is typical to low energy cluster impact. In the case of high energy C_{60} impact, the energy of C_{60} ion cannot spread out to near the surface, because the cross section is not large enough to produce numerous collisions. C_{60} ion penetrates deep into the substrate as a group of 60 carbon atoms. As a result of energy loss of C_{60} ion, deep cylindrical damage is formed. After the group is broken up, scattered damage pockets are created as a result of collision cascades near the end of the projection range.

As shown in Fig. 4.15, the damaged area has two different zones: the cluster zone, where a group of 60 carbon atoms has penetrated, and the monomer zone, where individual damage is formed. Although the penetration depth of C_{60} ion is the same as that of monomer ion, the number of defects produced by C_{60} is several times larger than that by carbon monomers at the same velocity as shown in section 4.3.3. Therefore, nonlinear multiple collisions, which are not proportional to size, occur when HOPG surface is bombarded by C_{60} and the number of defects in the cluster zone is more than that produced by individual impacts of 60 carbon atoms.

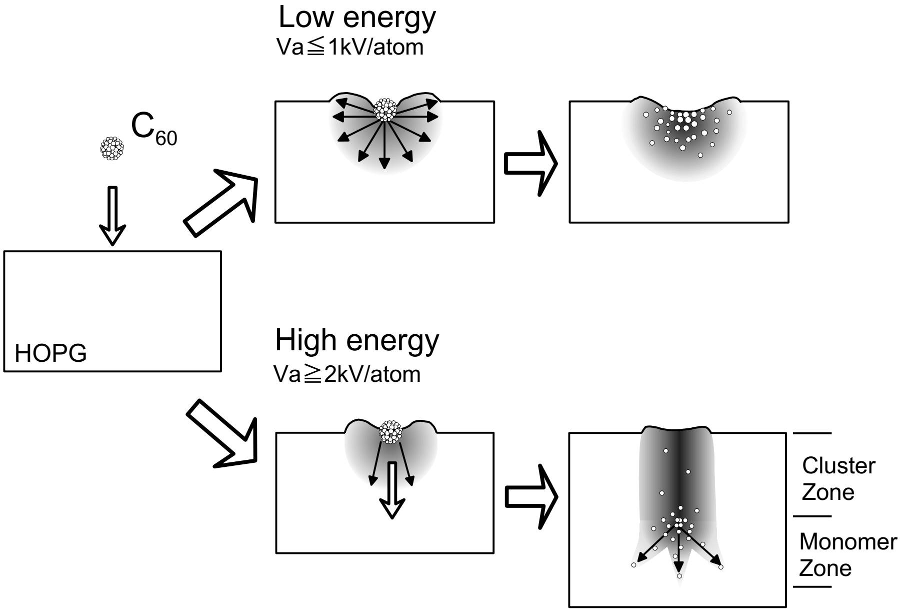

Figure 4.15: Schematic model of damage formations by C_{60} ion impacts. The mode of damage formation by C_{60} ion impacts differs according to ion energy.

4.4 Size Effect of Carbon Cluster Ion Impact

4.4.1 Smaller Size Carbon Cluster Ion Impacts

Fig. 4.16 shows STM images of HOPG surfaces irradiated with C_2, C_7, C_{19} and C_{60} accelerated to 5 kV/atom. Small hills with diameter of about 50 Å were observed on the surface irradiated with C_2 or C_7. Large hills with diameter of 100 Å to 150 Å were observed on surfaces irradiated with C_{19} or C_{60}. A large difference between cluster sizes 7 and 19 was observed. This indicates that in case of size above 19 the mechanism of trace formation is different from that by small carbon cluster, with a size less than 7.

Fig. 4.17 shows the dependence of the trace area on the cluster size. The carbon cluster was accelerated to 5 keV/atom or 10 keV/atom. The trace areas are proportional to cluster size up to 10 for both energies, and increase suddenly for cluster sizes above 10 atoms. For clusters below 10 atoms, the trace diameter for 5 keV/atom is higher than for 10 keV/atom. This is due to the fact that nuclear stopping power for 5 keV is higher than for 10 keV as shown in Fig. 4.11

4.4.2 RBS Investigation of Defects

In order to investigate the size dependence of amount of defects created by a carbon cluster ion impact, the number of disordered atoms was estimated from RBS channeling spectra. Si(100) substrates were irradiated with carbon cluster ions. The impact energy was 5 keV/atom and the size of cluster was 19, 52, 60, and 70. Fig. 4.18 shows the size dependence of the number of disordered Si atoms per carbon atom. The disordered atoms calculated by TRIM at impact energy of 5 keV is depicted as the monomer carbon ion irradiation.

The number of disordered Si atoms per carbon atom for carbon cluster impact was several times larger than that for monomer carbon impact. When the size was larger than 19, the number of disordered Si atoms increased slightly with the cluster size.

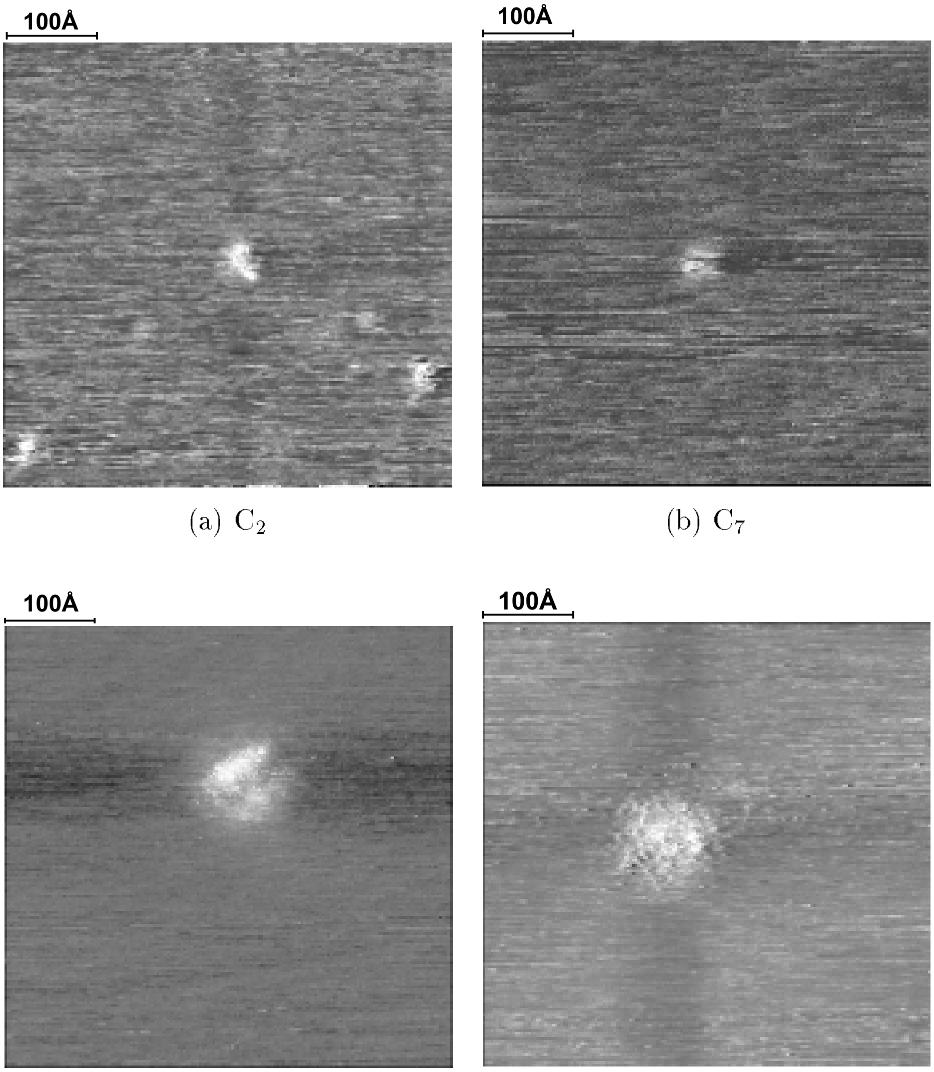

(a) C_2 (b) C_7

(c) C_{19} (d) C_{60}

Figure 4.16: STM images of HOPG surfaces irradiated with C_2, C_7, C_{19} and C_{60} accelerated to 5 kV/atom.

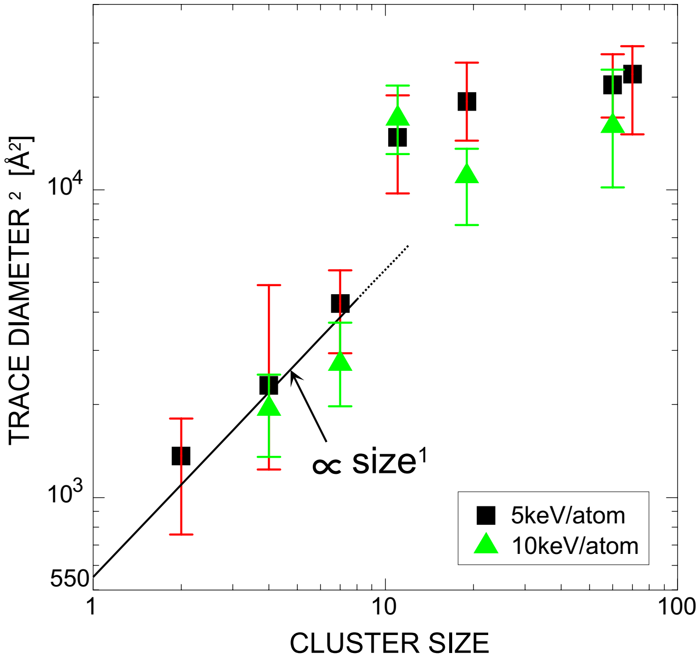

Figure 4.17: Dependence of trace area of carbon cluster impact on cluster size. Carbon cluster was accelerated to 5 keV/atom or 10 keV/atom.

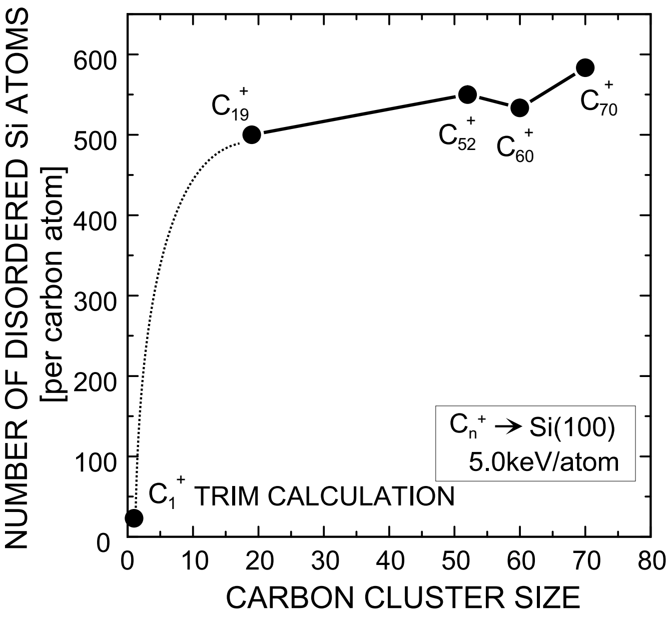

Figure 4.18: Size dependence of the number of disordered Si atoms created by a carbon cluster impact.

4.4.3 Damage Formation Mechanism

We propose a model to explain the drastic increase of the trace diameter. Fig. 4.19 shows the proposed model of damage formation by carbon cluster ion impacts, which is described as follows.

When a monomer ion collides with the surface, the incident atom excites the atoms on an area (S_a). After the incident atom goes through the first layer, excited atoms in S_a lose their energy and the rim of S_a doesn't become damage. Finally, the only damage remaining in each S_a is represented by S_d. When a cluster ion collides with the surface, the cluster is broken and the atoms constituting the cluster are scattered on an area (S_s). The scattered atoms impinge on the surface with the energy divided among the atoms constituting the cluster. If the cluster size (N) is small ($S_a \times N < S_s$), affected areas are isolated and appear as the small hills observed in Fig. 4.16(a) and Fig. 4.16(b). Therefore the damaged area of the first layer (S_1) is,

$$S_1 = S_d \times N, \tag{4.1}$$

which is proportional to the cluster size. Because the same effects occur in another layer, if STM scan is influenced by the damage area from the first to the n-th layer, the damage area (S) measured by STM is given by

$$\begin{aligned} S &= \sum_{i=1}^{n} a_i S_d N && (4.2) \\ &= A \times S_d \times n \times N \quad (A = \sum_{i=1}^{n} a_i) && (4.3) \end{aligned}$$

where i is the layer number and a_i is degree by which the STM scan is influenced by the damage area of the i-th layer. According to this model the trace area is proportional to the cluster size, when the cluster size is small ($S_a \times N < S_s$). We can say that such damage formation resembles monomer damage formation. The affected areas start to overlap with increasing cluster size. When the cluster size is large ($S_a \times N > S_s$), each area damaged by the atoms of one cluster cannot remain isolated like in

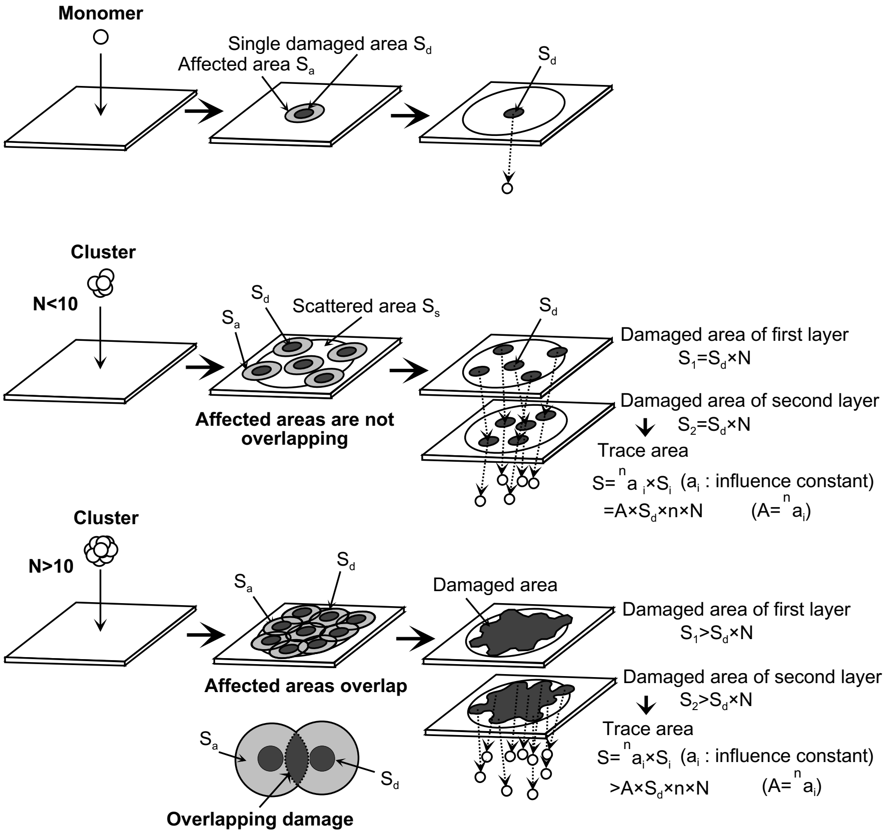

Figure 4.19: The model of damage formation by carbon cluster ion impacts. When cluster ion collides with the surface, atoms constituting cluster are scattered on an area (S_s) and excites the atoms on an area (S_a). If the cluster size (N) is small, affected areas are isolated. If cluster size is large, affected areas overlap and overlapping damage occurs. The magnitude of the damage area is enhanced.

the case of small clusters because of its geometrical size, and thus overlapping damage occurs. As multiple collisions in the area are affected by overlap, atoms are excited strongly. Thus, because such strongly excited atoms are disordered, the magnitude of the damage area of the 1-st layer (S_1) is enhanced. S_1 is,

$$S_1 > S_d \times N, \tag{4.4}$$

and the damage area (S) measured by STM is given by

$$\begin{aligned} S &> \sum_{i=1}^{n} a_i S_d N & (4.5)\\ &> A \times S_d \times n \times N \quad (A = \sum_{i=1}^{n} a_i) & (4.6)\end{aligned}$$

which is larger than the monomer like damage of the smaller cluster. As a result of this, the trace area increases suddenly, when the affected areas start to overlap. However, the trace area is limited to the scattered area (S_s) and S_s increases slightly with the cluster size. Therefore, when the cluster size is larger, the trace area increases slightly. Applying this model to the dependence of trace area on cluster size, our results, shown in Fig. 4.17, show that monomer like damage formation occurs when cluster size is less than 10 and cluster damage formation occurs when cluster size is 10 or more. According to this model, non-linear multiple collision effects occur only when a local area is instantaneously bombarded by more than 10 atoms, which appears to be the threshold value.

4.4.4 Secondary Electrons and Ions Yield

Fig. 4.20(a) shows secondary electron yields from Au surfaces bombarded by carbon cluster ions. The size of carbon clusters was 1, 7, 9, 11, and 60. The secondary electron yield was proportional to the velocity of carbon cluster ions for all sizes and did not depend on the size of clusters. The secondary electron yield should be proportional to the electronic stopping power. According to the model of Firsov [50], the electronic stopping power is proportional to the velocity of an incident particle. These results

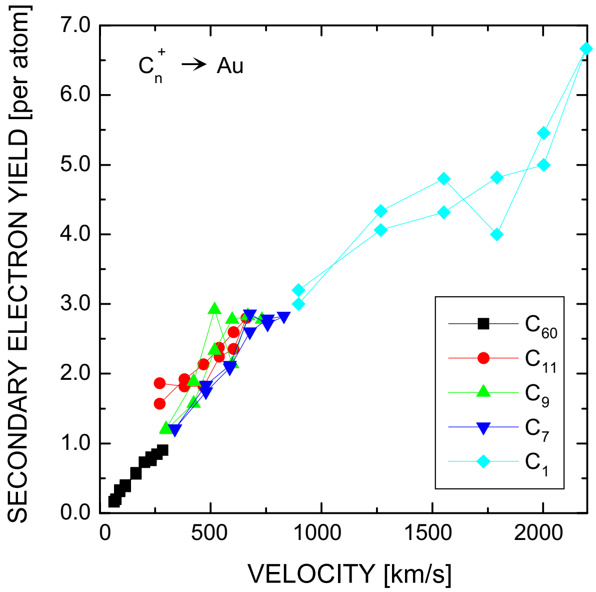

(a) Secondary electron yield

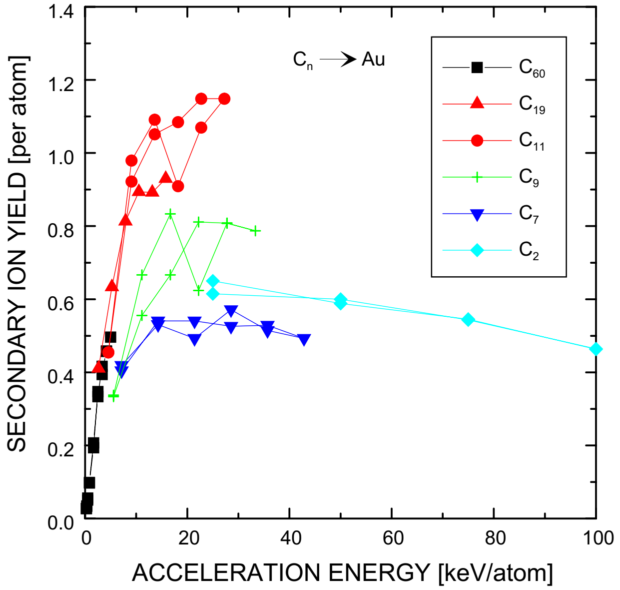

(b) Secondary ion yield

Figure 4.20: Secondary electron and ion yields from Au surfaces bombarded by carbon cluster ions.

show that the energy per atom deposited in the target does not depend on the size of clusters when the size is less than 60.

Fig. 4.20(b) shows secondary ion yields from Au surfaces bombarded by carbon cluster ions. The size of carbon clusters was 2, 7, 9, 11, 19, and 60. When the size of clusters was more than 11, the secondary ion yield was higher than that caused by smaller clusters whose size was less than 7. The secondary ion yield caused by C_{19} was about twice as high as that caused by C_7. The secondary ion yield should depend on the amount of displacement of near surface atoms. Therefore, the amount of displacement of near surface atoms increased discontinuously for cluster size above 10. These results indicate that non-linear multiple collision effects occur only when a local area is instantaneously bombarded by more than 10 atoms. This fact agrees with the model of damage formation by carbon cluster ion impacts as described in section 4.4.3.

Because the trace area is proportional to cluster size up to 10 as shown in Fig. 4.17, it is expected that the area of a trace created by a carbon monomer ion impact is about 550 Å^2. This trace area corresponds to S_d for the model of damage formation by carbon cluster. Because the secondary ion yield caused by C_{19} was about twice as high as that caused by C_7, affected area (S_a) can be estimated to be

$$S_a \sim 2 \times S_d. \tag{4.7}$$

When the cluster size is more than 10, the affected areas start to overlap. Therefore, the scattered area is

$$\begin{aligned} S_s &= 11 \times S_a & (4.8)\\ &\sim 22 \times S_d. & (4.9) \end{aligned}$$

Because S_d is about 550 Å^2, S_s is about 1.2×10^4 Å^2. The diameter of the scattered area is about 110 Å. This diameter corresponds with the diameter of a trace created by C_{11} (120 Å).

4.5 Summary

In this chapter, traces created by Ar cluster ion impact were observed and the annealing process of the traces was investigated. HOPG surfaces irradiated with high energy carbon cluster ions were observed and the mechanism of the interaction between high energy small cluster and surface was investigated.

1. The trace of a cluster ion impact showed a crater shape, with a diameter of about 80 Å. After Ar cluster atoms escaped as vapor from the target, a hole remained at the center of damage region and a crater was created. This indicates that cluster impact process is different from a summation of separate monomer impacts.

2. The crater shape was maintained after annealing at 300°C. Because atoms constituting the rim of the crater can migrate above 400°C, a part of the outer rim of the crater is chipped above 400°C. The outer rim of the crater disappears and the hemispherical damage in the target is removed at 600°C, but the hole remains.

3. The square of trace diameters is at maximum at acceleration energy between 2 keV/atom and 3 keV/atom. This dependence on acceleration energy is similar to that of nuclear stopping power. The similarity of dependence indicates that the energy loss of C_{60} ions near the surface causes a large trace on the surface.

4. C_{60} impacts have two different damage formation mechanisms according to impact energy. When the energy of C_{60} ion is low, all the energy of C_{60} ion is dissipated in the near surface region and forms hemispherical damage. When the energy of C_{60} ion is high, cylindrical damage is formed by collectively losing energy as a group of 60 atoms and the penetrating atoms separate and each atom creates its' individual damage.

5. Large hills were observed on HOPG surfaces irradiated with carbon cluster with size of up to 70. The impact site areas were found to

be proportional to cluster size for clusters of up to 10 atoms and increase discontinuously for cluster sizes above 10 atoms. This can be explained by considering that small affected areas overlap. This indicates that non-linear multiple collision effects occur only when a local area is instantaneously bombarded by more than 10 atoms.

Chapter 5

Ion Irradiation Effects on Initial Stage of Film Formation

5.1 Introduction

In order to reveal the role of ion bombardment during film formation, it is important to investigate ion bombardment effects on each stage of film formation such as adsorption of incoming depositing atoms on a surface, their surface diffusion, nucleation and island growth.

The film formation of Ge is well known and Ge islands on Si(111) are fabricated easily [51–53]. The formation of Ge film on a Si(111) 7×7 surface follows the Stranski-Krastanov (SK) growth mode [54]. A pseudomorphic 2D Ge layer forms on a Si(111) 7×7 surface at coverages of up to two bilayers (BL) and has a 5×5 reconstruction. The transition from 2D to 3D growth proceeds when Ge coverage exceeds 2 BL. In this chapter, the Ge islands are investigated with an STM and the ion bombardment effect on the kinetics of nucleus growth is studied.

5.2 Formation of Ge Islands

5.2.1 Deposition

The experiments were carried out in the UHV chamber containing the VT-STM, the ion gun and a Ge source. Ge atoms were deposited on the Si(111) surface at room temperature. Ge was evaporated from bulk Ge heated by a W wire, which was wound up around the Ge mass. The purity of Ge mass was 99.9999999 %. Fig. 5.1 shows the Si surface after Ge deposition. The thickness of the Ge film was 2-3 Å and the deposition rate was less than 0.1 BL per minute. In the long range, Ge was deposited uniformly on the Si(111) surface. In the short range, however, the corner holes of the 7×7 structure can be found. This image shows that the 7×7 lattice has a partial ordering effect at this low deposition dose.

5.2.2 Annealing

Fig. 5.2 shows the STM images of the Ge covered surface after annealing at various temperatures of 300°C, 400°C, 500°C, and 600°C for 30 minutes. Many Ge islands were formed by annealing above 300°C and the islands increased in size with annealing temperature. These results show that Ge atoms can migrate on a Si(111) surface above 300°C. The smaller Ge islands observed at 300°C migrated, combined with each other, and formed the large islands at higher temperatures. At 600°C, the diameter of one of the largest islands was more than 100 nm. The heights of the islands were 1 BL and the surfaces on the islands were flat at atomic level. The step edges were straight before annealing, but not straight after annealing. This suggests that some Ge atoms coalesced into the step edges.

Fig. 5.3 shows STM images of the Ge deposited surface after annealing at 400°C. Four islands were observed on a Si(111) 7×7 surface in Fig. 5.3(a). The surface structure on two islands, that were found at the left under side and at the right upper side, was of the 5×5 symmetry and the surface structure on other islands was of the 7×7 symmetry. This result

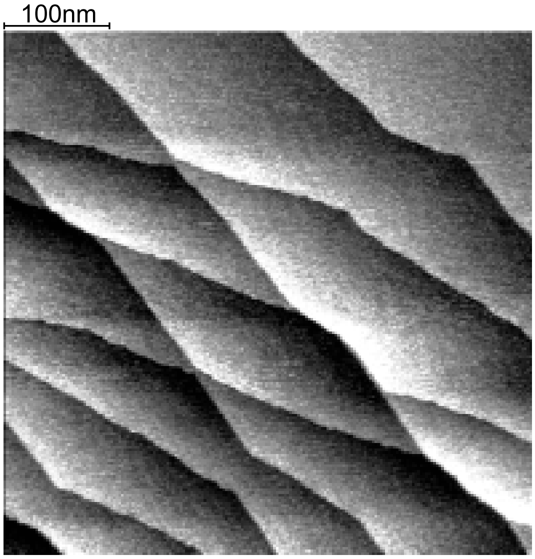

(a) Long range

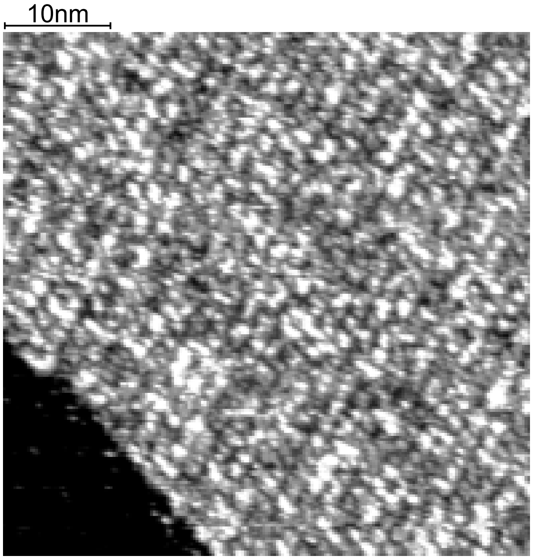

(b) Short range

Figure 5.1: STM images of the Si(111) surface after Ge deposition at room temperature.

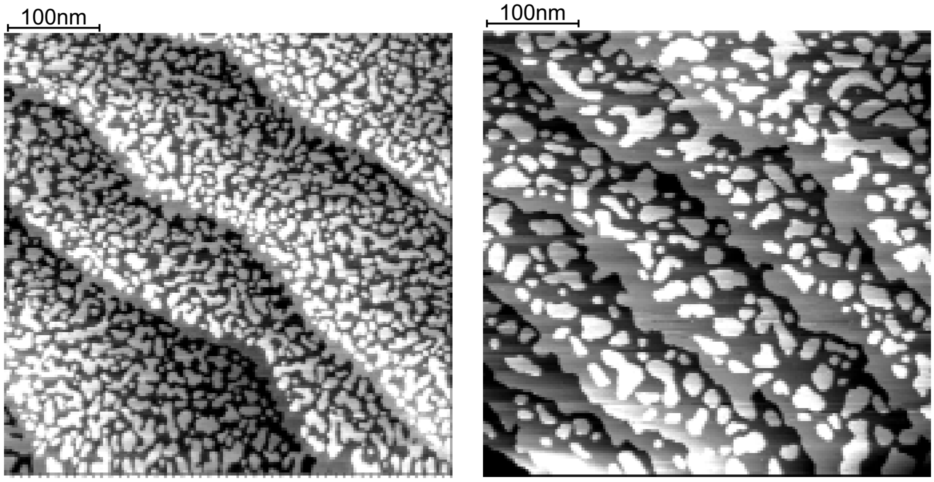

(a) At 300°C (b) At 400°C

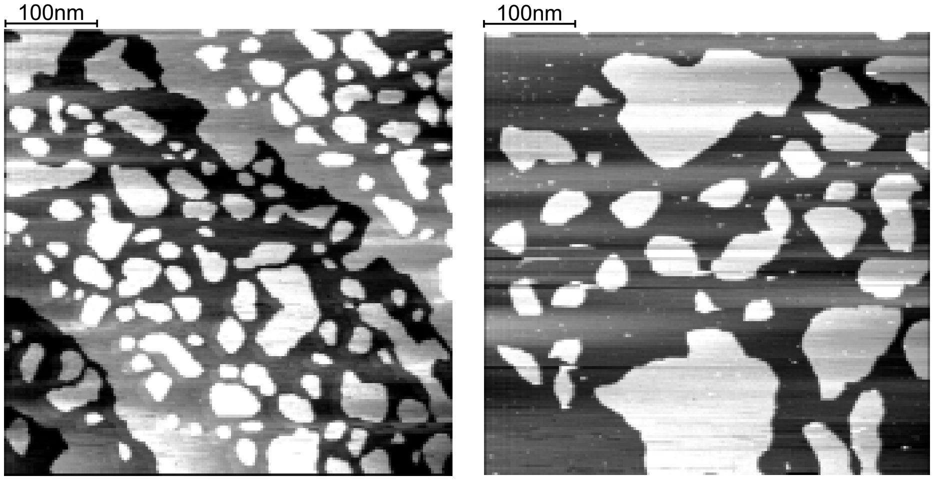

(c) At 500°C (d) At 600°C

Figure 5.2: STM images of Si(111) surface observed at various temperature after Ge deposition.

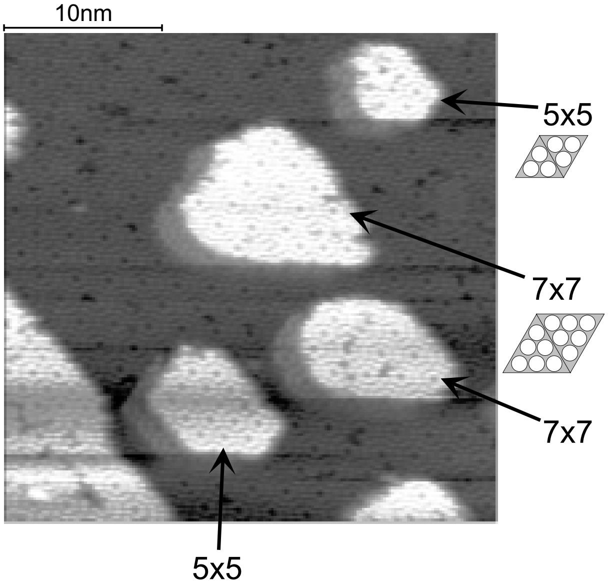

(a) Islands

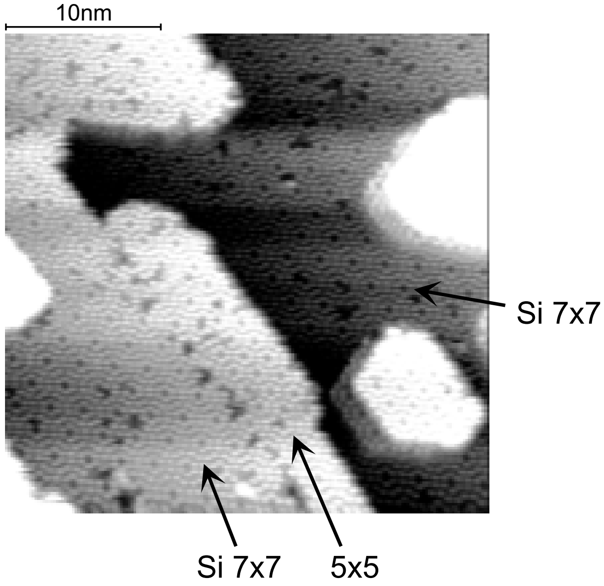

(b) Step

Figure 5.3: STM images of the Ge deposited surface after annealing at 400°C.

is similar to that obtained in the case of Ge Molecular Beam Epitaxy (MBE) at 370°C [55]. A line of step edge was observed in Fig. 5.3(b). A structure with the 5×5 symmetry was found on the step down of the terrace, where the step edge was not straight. These results show that some Ge atoms coalesced into the step edges.

5.2.3 Size Distribution of Islands

The size of Ge islands on the Si(111) surface was investigated after 30 minutes annealing at various temperatures. Fig. 5.4 shows the size histograms of Ge islands on wide terraces whose width is wider than 150 nm. The Y-axis in this figure shows the number of the Ge islands in an area of 1×1 μm^2. Many islands whose size was smaller than 1500 nm^2 were created at 300°C. The number of small islands whose size was smaller than 500 nm^2 decreased and the number of large islands whose size was larger than 1000 nm^2 increased at 400°C. Then, the number of small islands decreased also and the huge islands whose size was larger than 2500 nm^2 were created at 500°C. These results shows that the small islands whose size was smaller than 500 nm^2 become unstable in proportion as the annealing temperature increased and coalesced into the larger islands.

Fig. 5.5 shows the size histograms of Ge islands on narrow terraces whose width is smaller than 80 nm. The Y-axis in this figure shows the number of the Ge islands in an area of 1×1 μm^2. Many islands whose size was smaller than 1000 nm^2 were created at 300°C. The number of islands whose size was smaller than 500 nm^2 decreased, but almost no large islands whose size was larger than 1000 nm^2 were created at 400°C. Then, the number of small islands decreased also, but almost no large islands were created at 500°C. The huge island created at 500°C was a rare case. These results shows that the small islands whose size was smaller than 500 nm^2 become unstable in proportion as the annealing temperature, but did not coalesce into the large islands on the narrow terraces. The small islands could coalesce into the step edges.

Fig. 5.6 shows the coverage of the Ge islands on the Si(111) surface.

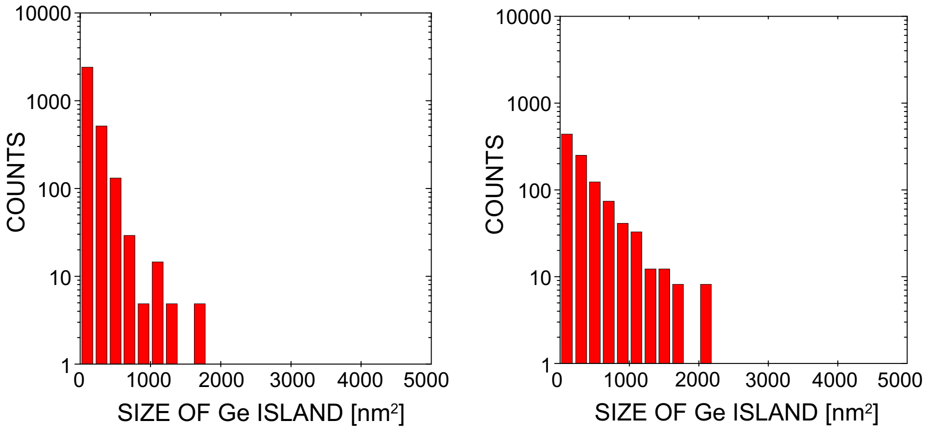

(a) At 300°C (b) At 400°C

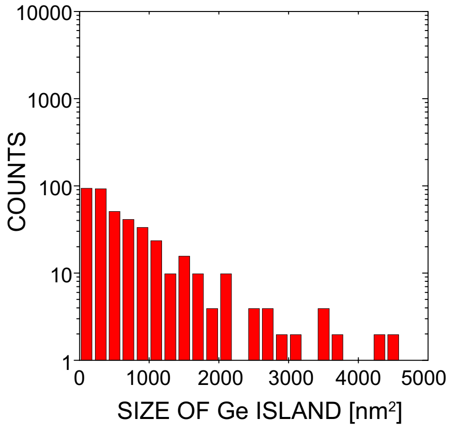

(c) At 500°C

Figure 5.4: Size histogram of Ge islands on wide terraces.

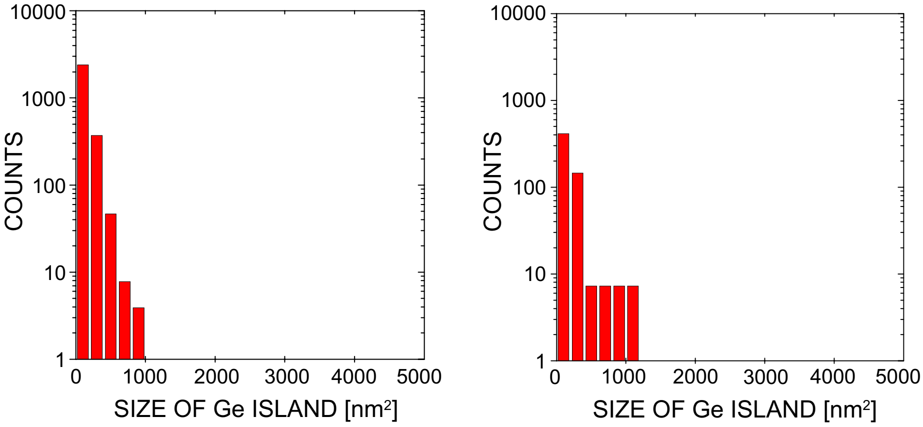

(a) At 300°C (b) At 400°C

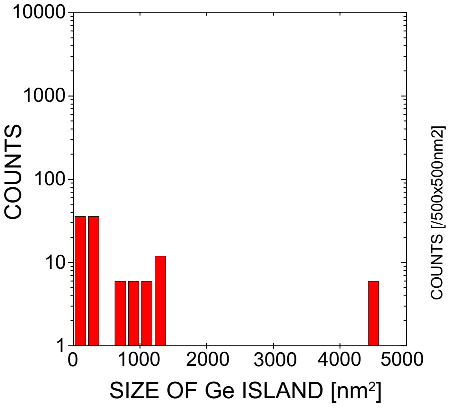

(c) At 500°C

Figure 5.5: Size histogram of Ge islands on narrow terraces.

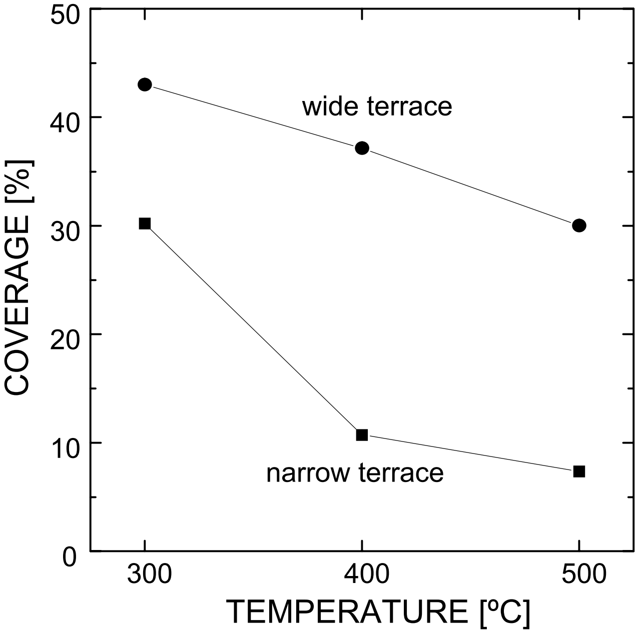

Figure 5.6: Coverage of Ge islands.

The coverage shows the ratio of the area occupied by islands to the analyzed area. The coverage of islands decreased with the annealing temperature on both wide and narrow terraces. This means that the islands coalesced into the step edges on both wide and narrow terraces. In narrow terraces, however, the coverage of islands was quite lower than that on wide terraces. This shows that on narrow terraces the number of islands which coalesced into the step edges was larger than that on wide terraces. At 500°C, almost all islands coalesced into the step edges on narrow terraces.

The activation energy of a Ge atom migration on Si(111) surface is about 2.48 eV [56]. The diffusivity of a Ge atom on Si(111) surface is

$$d_{Ge} = 600 \exp\left(\frac{-2.48}{\mathrm{k}T}\right) \quad \mathrm{cm}^2/\mathrm{sec}, \tag{5.1}$$

where k is Boltzmann's constant (eV/K) and T is temperature (K). The diffusion length of a Ge atom is

$$L = \sqrt{d_{Ge} \times t} \quad \mathrm{cm}, \tag{5.2}$$

where t is annealing time in seconds. At 300°C, the diffusion length is about 0.1 nm for 30 minutes annealing. The Ge atoms almost cannot reach the step edges because the width of narrow terraces is wider than the diffusion length. At 500°C, the diffusion length is about 85 nm for 30 minutes annealing. Almost all Ge atoms can reach the step edges because the diffusion length is wider than the width of narrow terraces. Moreover, the huge islands that may be stable at 500°C cannot be created because the narrow terrace is not enough wide to create such huge islands whose size was larger than 2500 nm^2. Therefore, almost all islands coalesced into the step edges on narrow terraces at 500°C.

5.3 Ion Irradiation Effects on Ge Islands

5.3.1 Xe Ion Irradiation and Annealing

In order to investigate ion bombardment effects on Ge islands on a Si(111) surface, the surface was irradiated with Xe ions at room temperature and the result of irradiation was observed with STM. The Xe irradiation was carried out at the following conditions: acceleration voltage - 5 kV, 59° incident angle and chamber pressure - 2×10^{-8} Torr.

Fig. 5.7 shows the STM images of Si(111) surface irradiated with various Xe ion doses after Ge deposition. The Ge islands were formed by 30 minutes annealing at 400°C. At doses lower than 1.3×10^{13} ions/cm^2, both islands and steps kept the sharp edges. At a dose of 1.0×10^{14} ions/cm^2, the image was different from others. The shapes of both the islands and steps were almost the same, but the edges were not sharp.

Fig. 5.8 shows STM images of a single Ge island irradiated with various Xe ion doses. These STM images show a single Ge island in the same area. At ion doses lower than 1.3×10^{13} ions/cm^2, several traces whose diameters were about 20 Å were observed. The number of the traces was of the same order as the number calculated from the ion doses, indicating that these were single ion traces formed by Xe ion impacts. The symmetry on the surface of the island remained almost the same and the sharp edges were maintained at these low doses. At a dose of 1.0×10^{14} ions/cm^2, the shapes of the islands were still almost the same, but the edges were not sharp anymore and the symmetry on the surface of the island was destroyed completely. The thickness of Ge was 2-3 Å and the Ge quantity was about 1×10^{15} atoms/cm^2. This indicates that in order to change the shape of Ge islands by ion impacts physically, it is necessary to irradiate with a ratio of ions to deposited atoms above 1/10. The number of defects formed by a single Xe ion at 5 kV was about 30 as calculated by TRIM simulation. Therefore, the total number of defects was comparable to that of deposited Ge atoms at 1.0×10^{14} ions/cm^2 and the islands were destroyed.

The sample with Xe irradiation of 1.0×10^{14} ions/cm^2 was annealed up to 600°C. Fig. 5.9 shows the result of annealing of Ge islands on the Si(111) surface after Xe ion irradiation. At 400°C, the Ge atoms constituting the islands migrated and also the Si(111) surface was reconstructed. Many small islands, vacancy clusters, and complicated steps were created. At 600°C, the islands are combined with the steps or become larger. Such

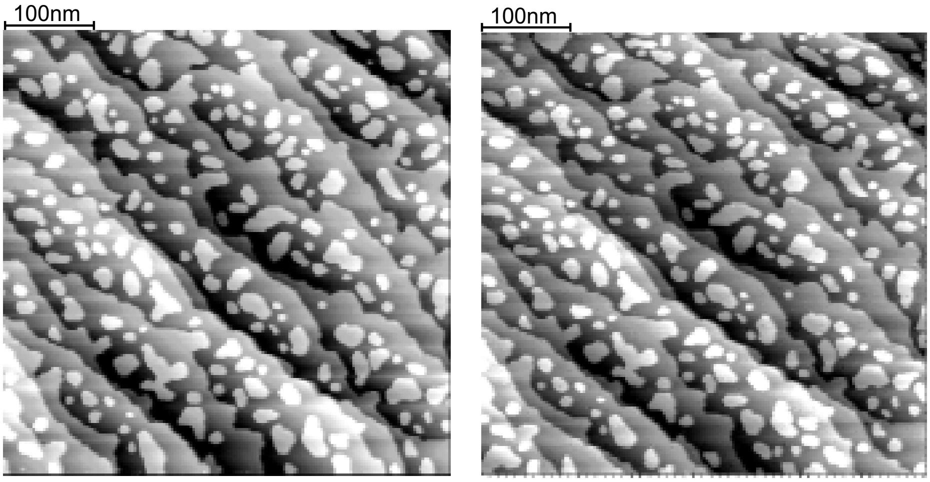

(a) Before irradiation

(b) 1.2×10^{12} ions/cm^2

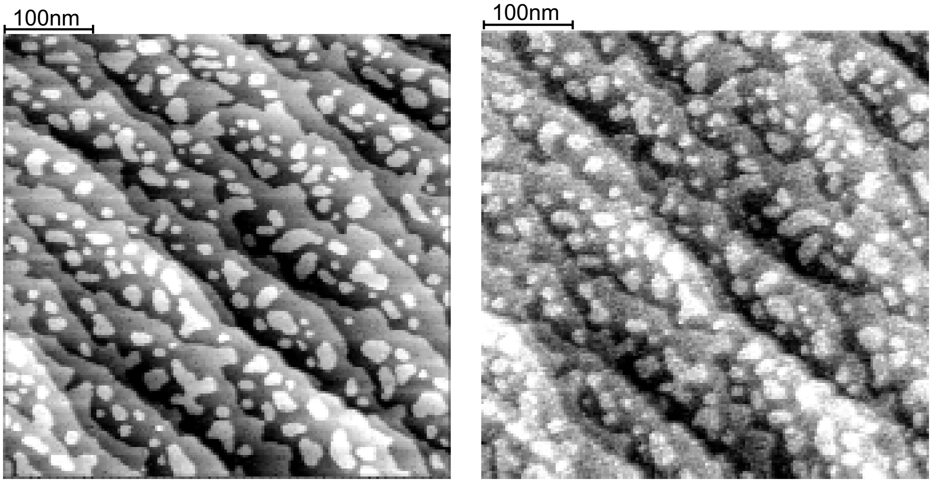

(c) 1.3×10^{13} ions/cm^2

(d) 1.0×10^{14} ions/cm^2

Figure 5.7: STM images of Si(111) surface irradiated with Xe after Ge deposition. (Va=5 kV, at room temperature)

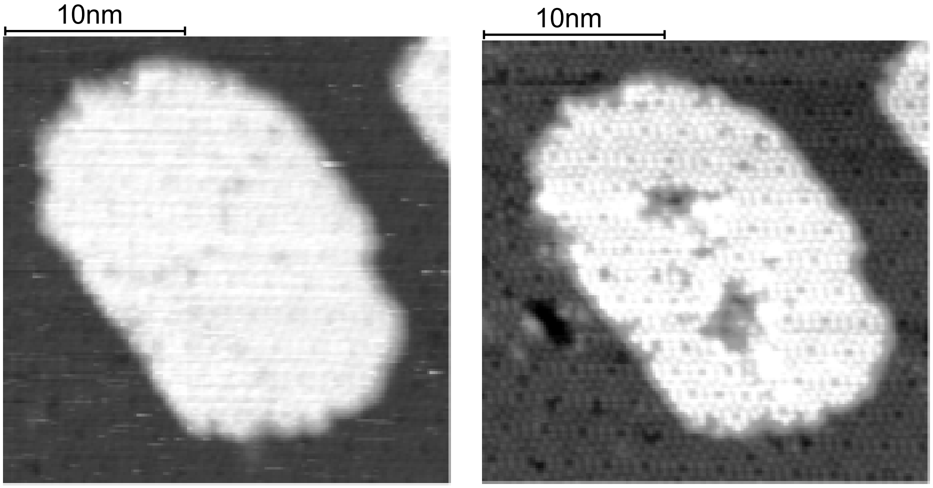

(a) Before irradiation (b) 1.2×10^{12} ions/cm^2

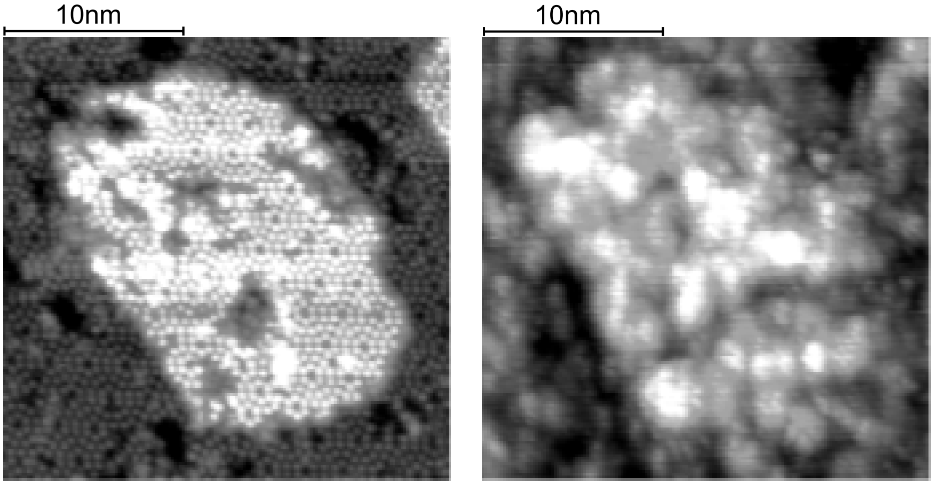

(c) 1.3×10^{13} ions/cm^2 (d) 1.0×10^{14} ions/cm^2

Figure 5.8: STM images of a Ge island irradiated with Xe. (Va=5 kV, at room temperature)

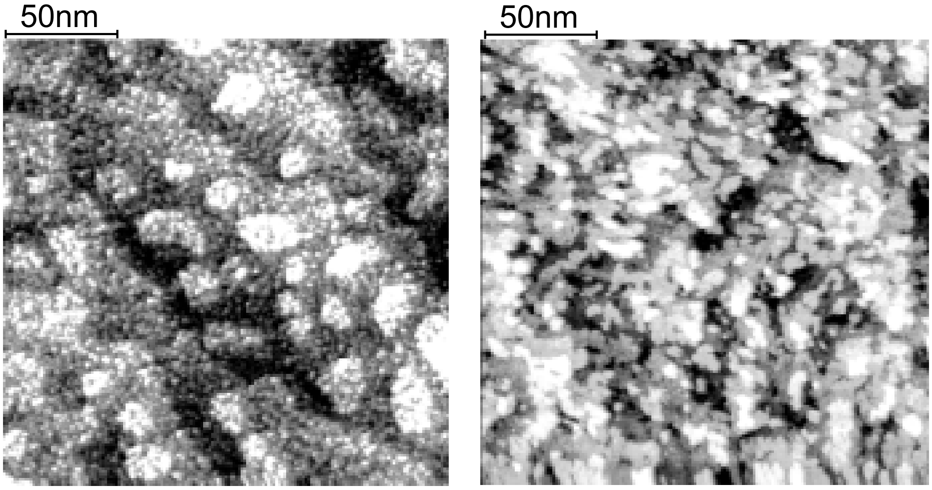

(a) At room temperature

(b) At 400°C

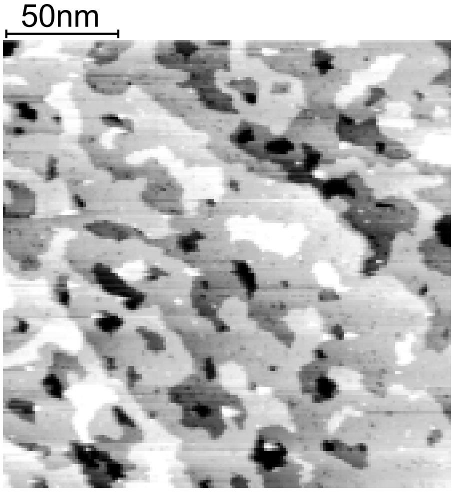

(c) At 600°C

Figure 5.9: Annealing of Ge islands on the Si(111) surface after Xe ion irradiation. (Va=5 kV)

a complex surface cannot be formed only by ion irradiation without annealing. Moreover, the complex surface cannot be formed only by annealing without ion irradiation as described in section 5.2. The surface can be formed only by both ion irradiation and annealing. This shows that the complex surface reconstruction was caused by the diffusion of defects formed by Xe ion irradiation.

Fig. 5.10 shows a model of the complex surface structure formation. When the surface was irradiated with Xe ions after creation of Ge islands, many vacancies were created in the bulk. At 400°C, some of the vacancies appeared on the surface and others recombined with interstitial atoms in the bulk. These vacancies can aggregate with the formation of the observed vacancy clusters and can be a driving force for the complex surface structure. At such temperature, Ge atoms could migrate, but the migrated Ge atoms could have been trapped with the vacancies and can be a building material for the formation of many small islands. At 600°C, both the vacancy clusters and Ge atoms can migrate. Therefore, the trapped Ge atoms are released and the islands are combined with the steps or became larger. The monomer ion impacts can have a large effect on the film formation if samples are annealed. If monomer ions radiate to films at high temperature, the density of nucleus becomes high as can be seen in Fig. 5.9(b) and the quality of films may be improved.

5.3.2 Ar Cluster Ion Irradiation and Annealing

In order to investigate cluster ion bombardment effects on Ge islands on a Si(111) surface, the surface was irradiated with Ar cluster ions at room temperature and the result of irradiation was observed with STM. The Ar cluster irradiation was carried out at the following conditions: acceleration voltage - 5 kV and ion dose - 4×10^{11} ions/cm^2.

Fig. 5.11(a) shows the STM images of Si(111) surface irradiated with Ar cluster ion after Ge islands formation. The Ge islands were formed by 30 minutes annealing at 400°C. The large craters were found in Fig. 5.11(a). The number of the traces was of the same order as the number

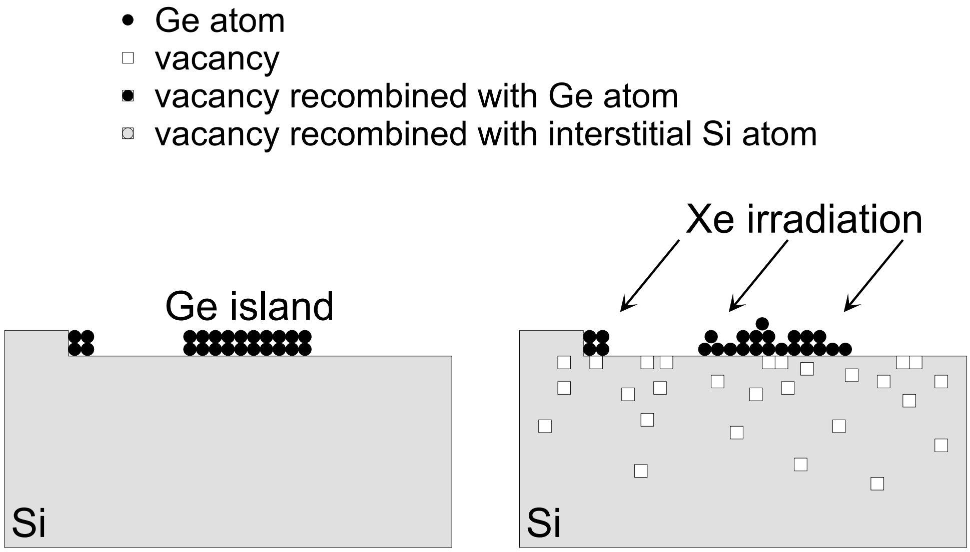

(a) Before irradiation - island created (b) After irradiation - vacancy created

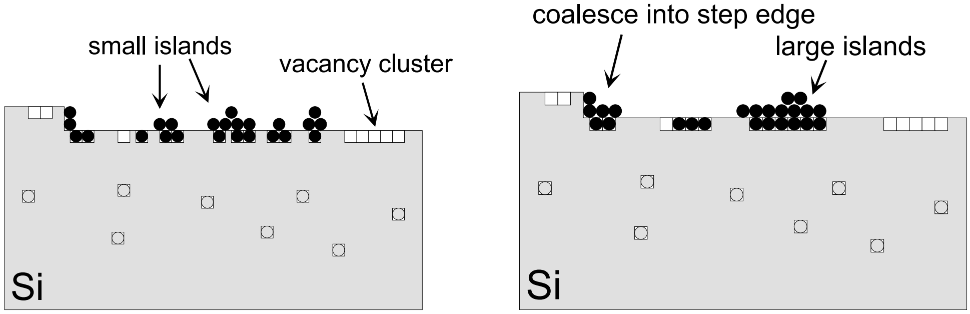

(c) At 400°C - vacancy diffuse toward surface

(d) At 600°C - surface vacancies diffuse with Ge atoms

Figure 5.10: Model of the complex surface structure formation.

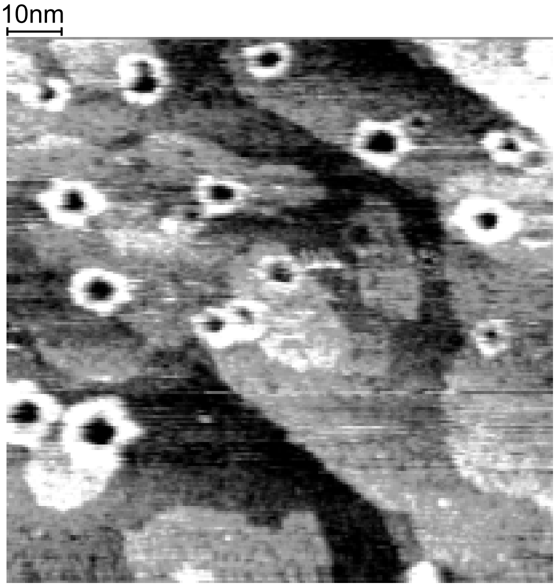

(a) At room temperature

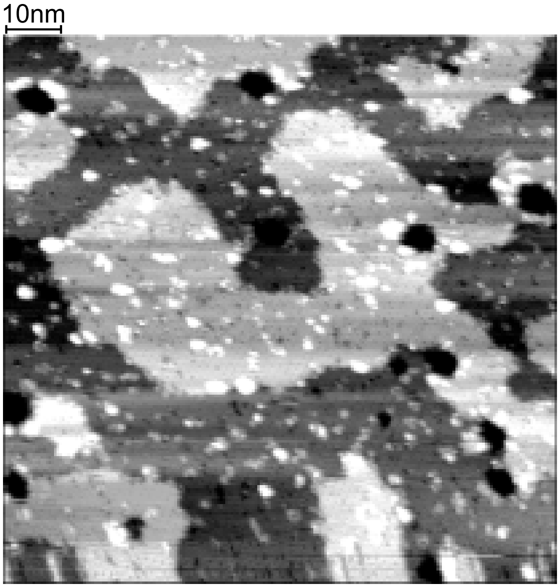

(b) At 600°C

Figure 5.11: STM images of the Ge islands after Ar cluster irradiation.

calculated from the ion doses, indicating that these were single ion traces formed by Ar cluster ion impacts. As can be seen, the number of Ge atoms displaced by one Ar cluster ion impact was much larger than that by one Xe ion impact. This result indicates that Ar cluster ion impacts can physically change the shape of Ge islands with low ion dose. They produce the many number of ad-atoms and this surface diffusion is enhanced with increasing the annealing temperature. These ad-atoms occupy the vacancy clusters and the number of vacancies decreases. Therefore, the film quality will be improved and high quality films can be formed by the cluster ion irradiation at lower temperature than the monomer ion irradiation. This suggestion is agreed that high quality ITO films can be obtained by O_2 cluster ion assisted deposition at room temperature [18].

The sample with Ar cluster irradiation was annealed at 600°C. Fig. 5.11(b) shows the result of annealing of Ge islands on the Si(111) surface after Ar cluster ion irradiation. The hole remained, but the outer rim of the crater disappeared and the hemispherical damage in the target was removed at 600°C. These results indicate that in the case of film formation at 600°C, the cluster ion impacts can have a large effect on the film formation, but the large number of disordered atoms may not remain in the film.

5.4 Summary

In this chapter, ion bombardment effects on Ge islands and the thermal annealing process after ion irradiation were described.

1. Many Ge islands were formed by annealing above 300°C after deposition and the size of the islands increased with annealing temperature. The surface structure on islands was of the 5×5 or 7×7 symmetry and some Ge atoms coalesced into the step edges.

2. It is necessary to irradiate with a ratio of ions to deposited atoms above 1/10, in order to physically change the shape of Ge islands by ion impacts. At the ion dose, the total number of defects is

higher than that of deposited Ge atoms. Therefore, the islands are destroyed.

3. When Ge islands on the Si(111) surface after Xe ion irradiation were annealed at 400°C, the Ge atoms constituting the islands migrated and also the Si(111) surface was reconstructed. Many small islands, vacancy clusters, and complicated steps were created.

4. After annealing at 600°C, the islands are combined with the steps or become larger. The complex surface structure observed after Xe ion irradiation and thermal annealing can be caused by the appearance and surface migration of vacancies that were formed by Xe ion impacts. The Xe ion impacts can have a large effect on the film formation if samples are annealed.

5. When the Si(111) surface was irradiated with Ar cluster ion after Ge islands formation, the large craters were formed. This result indicates that Ar cluster ion impacts can physically change the shape of Ge islands with low ion dose. The cluster ion impacts can have a large effect on the film formation even if samples are not annealed.

Chapter 6

Summary & Conclusions

In this study, we revealed the ion bombardment effects on surfaces and annealing process of the damage caused by ion impacts. For controlling ion beam processes at an atomic level, it is necessary to understand the interaction between energetic ions and solid surfaces. To explore the interaction, the surface defects created by ion impacts were analyzed with VT-STM. The annealing process of the defects that were vacancies or amorphized area was also analyzed. The surface was reconstructed or influenced strongly by the annealing after ion irradiation.

An ion beam system combined with a VT-STM in UHV was used in this work. The STM chamber is combined with an ion gun and a Ge source. Samples can be analyzed by STM with various temperatures after Xe irradiation and Ge deposition. The ion source can generate Ar clusters whose mean size is about 1000 and the large clusters are accelerated up to 10 keV. A carbon cluster ion beam system can generate small carbon clusters from fullerene and the clusters whose size is smaller than 70 are accelerated up to 400 keV.

The traces created by Xe ion impacts on Si(111) surfaces were observed with VT-STM and the annealing process of the damage was investigated. The single ion impact traces of about 20 Å diameter were clearly observed with atomic resolution. In the range from 1 to 5 keV, the average size of the trace does not depend on the impact energy.

When the sample is annealed at 400°C, the vacancies created in the subsurface by the impact start to diffuse toward the surface and appear on the surface, but the interstitial defects generated together with the vacancies remain in the bulk. At 600°C, vacancy clusters are formed, whose size corresponds to the number of vacancies created near the surfaces. At 650°C, the interstitial atoms diffuse and recombine with surface vacancies and the size of the vacancy cluster decreases with annealing time. Thus, the diffusion of both vacancies and interstitial atoms created by ion impacts is an important element for understanding the annealing process of the surface after ion irradiation.

In this work, the clear image of a single trace formed by a cluster ion impact was obtained and the mechanism of the cluster-surface interaction was investigated. When a Si(111) surface is irradiated with Ar cluster ions at 8 keV, the trace created by a cluster ion impact shows a crater shape, with a diameter of about 80 Å. This indicates that cluster impact processes are quite different from a summation of separate monomer impacts. In the case of monomer ion impact, the damage region is created by a cascade collision. When a cluster ion hits the target surface, the energy of the cluster ion spreads out symmetrically from the impact point into the target. The distributed energy causes hemispherical damage in the target, and target atoms around that surface region move, and this results in the shape of the outer rim of the crater. After the Ar atoms escape as vapor from the target, a hole remains at the center of damage region and a crater is created. In contrast, when the surface is annealed at 600°C after cluster irradiation, the outer rim of the crater disappears and the hemispherical damage in the target is removed, but the hole at the center of crater remains.

On HOPG surfaces irradiated with carbon cluster of up to 70 atoms, large hills were observed. The impact site areas were found to be proportional to cluster size for clusters of up to 10 atoms and increased discontinuously for cluster sizes above 10 atoms. This shows that monomer like damage formation occurs when cluster size is less than 10 and cluster damage formation occurs when cluster size is 10 or more. The mechanism of cluster damage formation can be explained by considering that small affected areas overlap. This indicates that non-linear multiple collision effects occur only when a local area is instantaneously bombarded by more than 10 atoms, which appears to be the threshold value.

An investigation with STM of Ge islands formed on Si(111) surface was also presented and the ion bombardment effect on the kinetic of nucleus growth was studied. After annealing of a Si(111) sample at 400°C, with a layer of Ge atoms deposited to a few Å, the formation of many islands of Ge was observed. The surface structure on islands was of the 5×5 or 7×7 symmetry and some Ge atoms coalesced into the step edges.

The Ge islands were irradiated with Xe ions and investigated with STM. In order to physically change the shape of the Ge islands by ion impacts, it is necessary to irradiate the surface so that the ratio of ions to deposited atoms is above 1/10. At this ion dose, the total number of defects is higher than that of deposited Ge atoms. When the Ge islands on the Si(111) surface were annealed at 400°C after Xe ion irradiation, many small islands, vacancy clusters, and complicated steps were observed. After annealing at 600°C, the islands either combined with the steps or became larger. The complex surface structure observed after Xe ion irradiation and thermal annealing can be caused by the appearance and surface migration of vacancies formed by Xe ion impacts. The Xe ion impacts can have much effect on the film formation if the samples are annealed.

When the Si(111) surface was irradiated with Ar cluster ion after Ge islands formation, large craters were found. This result indicates that Ar cluster ion impacts can physically change the shape of Ge islands with low ion dose. The cluster ion impacts can have a large effect on the film formation even if samples are not annealed.

From these results, we can understand that the diffusion of vacancies caused by monomer ion impact and post-annealing is very effective for surface modification. We can also understand that the diffusion of vacancies is effective in the film formation with ion irradiation. In the case of cluster ion impact, the high-density energy deposition caused by the multiple collision between incident atoms and substrate is a very important effect. The large amount of surface atom displacement caused by the high-density energy deposition is effective in the film formation at lower temperatures than the monomer impacts.

Thus, VT-STM was proved to be a very effective method to reveal the ion bombardment effects on surfaces and annealing process of surface defects. We expect that the results derived from STM measurements contribute to the development of ion processes.

References

[1] E.W.Müller and T.T.Tsong : Field Ion Microscopy, Principle and Applications, Elsevier, New York (1969).

[2] G.Binnig, H.Rohrer, Ch.Gerber and E.Weibel, Phys. Rev. Lett., **49** (1982) 57.

[3] G.Binnig, H.Rohrer, Ch.Gerber and E.Weibel, Phys. Rev. Lett., **50** (1983) 120.

[4] K.Takayanagi, Y.Tanishiro and M.Takahashi, J. Vac. Sci. & Technol., **A3** (1985) 1502.

[5] John J. Boland and John H. Weaver, Physics Today, August (1998) 34-40.

[6] G.Meyer, B.Voigtländer and N.M.Amer, Surf. Sci. Lett., **274** (1992) L541-L545.

[7] P.Bedrossian and Efthimios Kaxiras, Phys. Rev. Lett., **70** (1993) 2589.

[8] P.Bedrossian and T.Klitsner, Phys. Rev., **B44** (1991) 13783.

[9] P.Bedrossian and T.Klitsner, Phys. Rev. Lett., **68** (1992) 646. 5 (1994) 263.

[10] H.J.W.Zandvliet, H.B.Elswijk and E.J.van Loenen, Phys. Rev., **B46** (1992) 7581.

[11] M.Akizuki, J.Matsuo, W.Qin, T.Aoki, M.Harada, S.Ogasawara, K.Yodoshi and I.Yamada, Mater. Chem. Phys., vol.54, no.1-3 (1998) 255.

[12] F.Rossi, B.Andre, A.V.Veen, P.E.Mijnarends, H.Schut, F.Labohm, H.Dunlop, M.P.Delplancke and K.Hubbard, J.Mater. Res., vol.9, no.9 (1994) 2440.

[13] K.Kubota and M. Naoe, J. Appl. Phys., vol.70, no.10 (1991) 6430.

[14] I.Yamada, J.Matsuo, Z.Insepov and M.Akizuki, Nucl. Instr. and Meth. **B106** (1995) 165.

[15] I.Yamada, W.L.Brown, J,A,Northby and M.Sosnowski, Nucl. Instr. and Meth., **B79** (1993) 223.

[16] G.H.Takaoka, G.Sugawara, R.E.Hummel, J,A,Northby, M.Sosnowski and I.Yamada, Mat. Res. Soc. Symp. Proc., **316** (1994) 1005.

[17] Z.Insepov, M.Sosnowski and I.Yamada, Advanced Materials '93 IV/Laser and Ion Beam Modification of Materials, ed. I.Yamada et al, Trans. Mat. Res. Soc. Jpn. **17** (1994) 1110.

[18] W.Qin, R.P.Howson, M.Akizuki, J.Matsuo, G.Takaoka and I.Yamada, Mater. Chem. Phys., vol.54, no.1-3 (1998) 258.

[19] N.Toyoda, N.Hagiwara, J.Matsuo and I.Yamada, Nucl. Instr. and Meth. **B148** (1999) 639.

[20] A.Nishiyama, M.Adachi, N.Toyoda, N.Hagiwara, J.Matsuo and I.Yamada, AIP conference proceedings (Fifteenth International Conference on Application of Accelerators in Research and Industry) **475** (1998) 421.

[21] N.Shimada, T.Aoki, J.Matsuo, I.Yamada, K.Goto and T.Sugui, J. Mat. Chem. and Phys. **54** (1998) 80.

[22] M.Akizuki, J.Matsuo, M.Harada, S.Ogasawara, A.Doi, K.Yoneda, T.Yamaguchi, G.H.Takaoka, C.E.Asheron and I.Yamada, Nucl. Instr. and Meth. **B99** (1995) 229.

[23] M.Akizuki, J.Matsuo, S.Ogasawara, M.Harada, A.Doi and I.Yamada, Jpn. J. Appl. Phys., **35** (1996) 1450.

[24] N.Toyoda, H.Kitani, J.Matsuo and I.Yamada, Nucl. Instr. and Meth., **B121** (1997) 484.

[25] D.Takeuchi, J.Matsuo, A.Kitai and I.Yamada, Mater. Sci. and Eng. A. MSA217/218 (1996) 74.

[26] I.Yamada, J.Matsuo, Z.Insepov, D.Takeuchi, M.Akizuki and N.Toyoda, J. Vac. Sci. Technol. A 14(3), (1996) 781.

[27] D.Takeuchi, K.Fukushima, J.Matsuo and I.Yamada, Nucl. Instr. and Meth., **B121** (1997) 493.

[28] T.Seki, T.Kaneko, D.Takeuchi, T.Aoki, J.Matsuo, Z.Insepov and I.Yamada, Nucl. Instr. and Meth., **B121** (1997) 498.

[29] D.Takeuchi, T.Seki, T.Aoki, J.Matsuo and I.Yamada, J. Mat. Chem. and Phys. **54** (1998) 76.

[30] M.Dobeli, F.Ames, R.M.Ender, M.Suter, H.A.Synal and D.Vetterli, Nucl. Instr. and Meth., **B106** (1995) 43.

[31] A.Hallen, P.Hakanson, N.Keskitalo, J.Olsson, A.Brunelle, S.Della-Negra and Y.Le Beyec, Nucl. Instr. and Meth., **B106** (1995) 233.

[32] G.Brauchle, S.Richard-Schneider, D.Illig, R.D.Beck, H.Schreiber and M.M.Kappes, Nucl. Instr. and Meth., **B112** (1996) 105.

[33] Y.Mori, H.Kawada and K.Tsuchikata, Nihon Kikai Gakkaishuu, **31** (1952) 104.

[34] Y.Mori, H.Kawada and K.Tsuchikata, Technical report, The Institute of Physical and Chemical Research (RIKEN),(1952).

[35] H.W.Liepmann and A.Roshko, "Element of Gas Dynamics"(Johnes Wiley and Sons, Inc., New York, 1960).

[36] H.Ashkenas and F.S.Sherman, "Rarefied Gas Dynamics"(ed. J.H.de Leeuw), Academic Press, New York, **2** (1965) 84.

[37] U.Bossel, ph.D.Thesis, Univ. of Calif., Barkley and UCB Report, **AS-68-6** (1968).

[38] J.P.Biersack and L.G.Haggmark, Nucl. Instr. and Meth., **174** (1980) 257.

[39] F.H.Stillinger and T.A.Weber, Phys. Rev. B, **31** (1985) 5262.

[40] J.F.Ziegler, J.P.Biersack and U.Littmark, "The stopping and range of ions in solids", Pergamon Press, New York, 1985, p.321.

[41] P.M.Fahey, P.B.Griffin and J.D.Plummer, Rev. Mod. Phys., vol.61, no.2, (1989) 289.

[42] H.J.Gossmann, C.S.Rafferty, H.S.Luftman, F.C.Unterwald, T.Boone and J.M.Poate, Appl. Phys. Lett. 63(5), (1993) 639.

[43] I.S.Hwang, R.L.Lo and T.T.Tsong, J. Vac. Sci. Technol. A 16(4), (1998) 2632.

[44] Z.Insepov, M.Sosnowski and I.Yamada, Proc. **IU-MRS** Int. Conf. on Adv. Mat. Tokyo, (1993).

[45] R.Coratger, A.Chahboun, V.Sivel, F.Ajustron and J.Beauvillain, Ultramicroscopy, 42-44 (1992) 653.

[46] T.R.Albrecht, H.A.Mizes, J.Nogami, Sang-il Park and C.F.Quate, Appl. Phys. Lett. **52** (1987) 362.

[47] J.Tersoff, Phys. Rev., 39/8 (1988) 5566.

[48] L.C.Feldman, R.L.Kaufman and P.J.Silverman, Phys. Rev. Lett., **39** (1977) 38.

[49] M.Tanomura, D.Takeuchi, J.Matsuo, G.H.Takaoka and I.Yamada, Nucl. Instr. and Meth., **B121** (1997) 480.

[50] O.B.Firsov, J. Exp. Theoret. Phys., **36** (1959) 1076.

[51] N.Motta, A.Sgarlata, R.Calarco, Q.Nguyen, J.Castro Cal, F. Patella, A. Balzarotti and M. De Crescenzi, Surf, Sci., **406** (1998) 254.

[52] N.Motta, A.Sgarlata, M.De Crescenzi and J.Derrien, Appl. Surf. Sci. **102** (1996) 57.

[53] B.Voigtländer and A.Zinner, Appl. Phys. Lett., vol.63, no.22 (1993) 3055.

[54] A.A.Shklyaev, M.Shibata and M.Ichikawa, Phys. Rev. B, vol.58, no.23 (1998) 15647.

[55] J.Wintterlin and Ph.Avouris, J. Chem. Phys., vol.100, no.1 (1994) 687.

[56] R.Ditchfield and G.Seebauer, Phys. Rev. Lett., vol.82, no.6 (1999) 1185.

List of Figures

List of Publications

Full Length Papers

1. T.Seki, T.Kaneko, D.Takeuchi, T.Aoki, J.Matsuo, Z.Insepov and I.Yamada, "STM Observation of HOPG Surfaces Irradiated with Ar Cluster Ions", Nucl. Instr. and Meth., **B121** (1997) 498.
2. T.Seki, T.Aoki, M.Tanomura, J.Matsuo and I.Yamada, "Energy Dependence of a Single Trace Created by C_{60} Ion Impact", J. Mat. Chem. and Phys., **54** (1998) 143.
3. T.Seki, J.Matsuo and I.Yamada, "UHV-STM Study on Ion Assisted Deposition", Nucl. Instr. and Meth., **B**, To be published.
4. T.Seki, T.Aoki, J.Matsuo and I.Yamada, "STM Observation of Surface Vacancies Created by Ion Impact", Nucl. Instr. and Meth., **B**, To be published.
5. D.Takeuchi, T.Seki, T.Aoki, J.Matsuo and I.Yamada, "Cluster Ion Bombardment on Atomically Flat Au(111) Solid Surfaces", J. Mat. Chem. and Phys., **54** (1998) 76.
6. T.Aoki, T.Seki, J.Matsuo, Z.Insepov and I.Yamada, "Molecular Dynamics Simulation of a Carbon Cluster Ion Impacting on a Carbon Surface", J. Mat. Chem. and Phys., **54** (1998) 139.
7. T.Aoki, T.Seki, J.Matsuo, Z.Insepov and I.Yamada, "Cluster Size Dependence of the Impact Process on a Carbon Substrate", Nucl. Instr. and Meth., **B**, To be published.

8. I.Yamada, J.Matsuo, Z.Insepov, T.Aoki, T.Seki and N.Toyoda, "Nano-Processing with Gas Cluster Ion Beams", Nucl. Instr. and Meth., **B**, To be published.

Proceedings

1. T.Seki, M.Tanomura, T.Aoki, J.Matsuo and I.Yamada, "Size Dependence of Bombardment Characteristics Produced by Cluster Ion Beams", Materials Research Society Symposium Proceeding (conf. of 1997 MRS Fall Meeting, Symposium KK, Boston, MA, USA), **504** (1998) 93.

2. T.Seki, J.Matsuo and I.Yamada, "VT-STM Observation of Si Surfaces Damaged by Ion Impact", Technical Report of the Institute of Electronics, Information and Communication Engineers of Japan (Silicon Device Materials, Kyoto, Japan), Vol. 98, No. 445, pp.31 (1998) [in Japanese].

3. T.Seki, J.Matsuo and I.Yamada, "STM Observations of the Annealing Process of the Damage caused by Ion Impact", Proceeding of the XIIth International Conference on Ion Implantation Technology (conf. of IIT '98, Kyoto, Japan), pp.1262 (1999), IEEE.

4. M.Ishida, T.Seki, J.Matsuo, G.H.Takaoka and I.Yamada, "Fabrication of Resonant Tunneling Devices Using Epitaxtial Al/Al_2O_3", The 4th symposium on intelligent materials, Tokyo, March 23-24, 1995, session No.A7.

5. T.Aoki, T.Seki, M.Tanomura, J.Matsuo, Z.Insepov and I.Yamada, "Molecular Dynamics Simulation of Fullerene Cluster Ion Impact", Materials Research Society Symposium Proceeding (conf. of 1997 MRS Fall Meeting, Symposium KK, Boston, MA, USA) **504** (1998) 81.

6. J.Matsuo, N.Toyoda, M.Saito, T.Aoki, T.Seki and I.Yamada, "Novel

Analysis Techniques using Cluster Ion Beams", AIP conference proceedings (Fifteenth International Conference on Application of Accelerators in Research and Industry, Denton, TX, USA) **475** (1998) 429.

7. T.Kusaba, T.Seki, T.Aoki, J.Matsuo, M.Kase, K.Goto, T.Sugii and I.Yamada, "Damage Formation and Enhanced Diffusion by Decaborane Ion Implantation", Technical Report of the Institute of Electronics, Information and Communication Engineers of Japan (Silicon Device Materials, Kyoto, Japan), Vol. 98, No. 445, pp.97 (1998) [in Japanese].

International Conference

1. T.Seki, T.Kaneko, D.Takeuchi, T.Aoki, J.Matsuo, G.H.Takaoka and I.Yamada, "STM Observation of Surfaces Irradiated with Ar Cluster Ions", The Joint International Symposium of the '96 MRS-J Conference (Symp. N:'Materials Synthesis and Modification by Ion and/or Laser Beam') and the 3rd Ion Enginnering Conference, May (1996), Chiba, Japan.

2. T.Seki, T.Aoki, M.Tanomura, J.Matsuo and I.Yamada, "STM Observation of Surfaces Irradiated with Carbon Cluster Ions", The 4th IUMRS International Conference in Asia (Symp. H:'Materials Synthesis and Modification by Ion and/or Laser Beam'), September 16-18 (1997), Chiba, Japan.

3. T.Seki, M.Tanomura, T.Aoki, J.Matsuo and I.Yamada, "Size Dependence of Bombardment Characteristics Produced by Cluster Ion Beams", Conference of 1997 MRS Fall Meeting (Symposium KK), December (1997), Boston, MA, USA.

4. T.Seki, J.Matsuo and I.Yamada, "STM Observation of the Annealing Process of the Damage by Ion Impact", XIIth International Con-

ference on Ion Implantation Technology (IIT'98), June (1998), Kyoto, Japan.

5. T.Seki, J.Matsuo and I.Yamada, "UHV-STM Study on Ion Assisted Deposition", The 14th International Conference on Ion Beam Analysis / 6th European Conference on Accelerators in Applied Research and Technology (IBA-14/ECAART-6), July (1999), Dresden, Germany.
6. T.Seki, T.Aoki, J.Matsuo and I.Yamada, "STM Observation of Surface Vacancies Created by Ion Impact", The 18th International Conference on Atomic Collisions in Solids (ICACS-18), August (1999), Odense, Denmark.

Award

- Best Student Award in 12th International Conference on Ion Implantation Technology, June (1998), Kyoto, Japan.